5-2016

Hydrothermal oxide and nontronite deposits at Seamount 3, Wolf-Darwin lineament, Galapagos Archipelago, Ecuador

Megan J. Lubetkin
Bates College '16, mjlubetkin@gmail.com

Steven Carey
Univeristy of Rhode Island - Graduate School of Oceanography, scarey@uri.edu

Genevieve Robert
Bates College, grobert@bates.edu

Hydrothermal oxide and nontronite deposits at Seamount 3, Wolf-Darwin lineament, Galapagos Archipelago, Ecuador

Bates College Geology Department Thesis

Presented to the Faculty of the Department of Geology, Bates College,
in partial fulfillment of the requirements for the Degree of Bachelor of Science

by

Megan J. Lubetkin

Lewiston, Maine
April 8th, 2016

Dedicated to the yogi of Dunagiri. A friend, who now knowing of the existance of life and complex systems at the great depths of the ocean, will meditate on the connections we all share and the ways we are able to explore the planet and our minds.

Acknowledgments

This thesis would not be possible without the tremendous support, guidance, and mentorship of my advisors, educators, family, and friends. From the moment I boarded the E/V *Nautilus* in the summer of 2015, I knew that it would be a dream to write my senior thesis about something newly discovered in the Galapagos. I cannot thank the science and engineering teams enough for all of their countless hours spent balancing on an uneven deck while preparing for ROV exploration, logging data, working in the wet lab, and fixing up *Herc*. The experience I had while on the ship for 6 weeks was completely life-changing. For that, I thank everyone at the Ocean Exploration Trust for providing such an incredible opportunity to take part in ocean exploration. Major thanks to Nicole Raineault for assembling such tremendous science teams for each leg and for teaching me nearly all I know about science research onboard an exploration vessel. I cannot wait to return to the ship this season. Special thanks to the Ocean Exploration Trust as a whole and Bates College for helping fund the research and project.

Dr. Robert Ballard has been a tremendous inspiration to me, and for that I am truly grateful. Bob, you took me in and fueled my passion for exploration every day at sea and on land. I cannot thank you enough for that and for introducing me to Steve Carey. Steve, I cannot tell you how much this project means to me and how much I appreciate you advising me from afar throughout this year. Your excitement about marine geology and volcanism shows through all that you do. It is an absolute joy working with you and learning from your tremendous wealth of knowledge and experience in these fields.

Genevieve Robert, I truly cannot thank you enough for these last two semesters. You have taught me so much about scientific writing, research, and the joys of learning new things. I especially appreciate your tremendous dedication to scholarship and mineralogy. You and your work have inspired me so much to pursue a career in geology. Thank you for supporting me this year as my thesis advisor and in general. I would not be where I am now without you.

To all who helped with my data collection and results, thank you so much. Katie Kelley, thank you for sitting me down and thoroughly explaining all there is to know about ICP-MS and ICP-AES and for preparing the samples and running them with me. I cannot thank you enough for sharing your expertise and your thrill for the work. Major thanks to Jacob Balcanoff for assisting in the sample prep procedures and for all that you did while on ship last season. Greg Anderson, thank you so much for spending so many hours with me down in the Bates SEM-EDS suite. I really appreciate all that you taught me about imaging and sample preparation.

Thank you so much to Mike Retelle, Bev Johnson, Dyk Eusden, and everyone involved with the Bates Geology Department. You are all an inspiration and tremendously supportive of us. Thesis seminar was a wonderful experience because of you. These past four years were fully shaped by your presence and guidance in and out of the classroom. Thank you to all of the Bates geology seniors and all of my tremendously supportive friends.

Finally, I owe all of my success and motivation to my parents and family. You have shown me what hard work looks like and what determination is. You have shown me what love is and how to balance it with a life of learning. Your support for my work and passions has always been present.

Abstract

An unusual deposit of Fe-rich hydrothermal nontronite was recovered by remotely operated vehicle (ROV) from Seamount 3 of the Wolf-Darwin lineament, Galapagos Marine Reserve. X-ray diffraction, ICP-MS/ICP-AES, and SEM-EDS analyses show that this deposit is chemically and mineralogically similar to other deep-sea hydrothermal nontronites, indicating a formation temperature of about 30º to 50º Celsius. These Fe-Si-oxides and Fe-rich Al-poor nontronite deposits contain about 38-51 weight % SiO_2 and 40-50 weight % Fe_2O_3. Although hydrothermal nontronite has been sampled at a number of sites by coring and dredging, this is the first in situ documentation of its sinuous, tubular structure on the seafloor. Image-analysis of ROV imagery suggests that this unusual pattern might be controlled by fluid pathways in the underlying pillow lavas.

Table of Contents

Table of Figures

Table of Tables

1. Introduction to thesis

1.1 Purpose

Studies of seafloor hydrothermal vents have typically focused on high temperature discharges that produce black smokers and chimneys consisting of sulfide deposits which were first discovered along the Galapagos Spreading Center in 1977 (Green et al., 1981; Figure 1.1). However, more recent studies have suggested that low temperature diffuse flow may actually be as important, or even more important, than high temperature venting in the discovery of sulfide deposits (Murnane and Clague, 1983; Figure 1.2). In particular, studies of Pacific seamounts have documented common low temperature hydrothermal deposits that are rich in iron and the clay mineral nontronite (Alt, 1988). Nontronite is an iron-rich aluminum-poor end-member of the smectite group of clay minerals, and is considered to be the most common clay mineral present in hydrothermal deposits around the world (Bischoff, 1972; Murnane and Clague, 1983; Thompson et al., 1988; Singer and Stoffers, 1987; Alt, 1988; Hékinian et al., 1993; Severmann et al., 2004).

Low temperature diffuse hydrothermal systems lack the megafauna, such as tubeworms and giant clams that are commonly observed at high temperature vents. Nonetheless, low temperature diffuse vents provide conditions that are ideal for bacterial colonization and growth, while also providing substrates for stationary organisms such as corals. Specialized Fe-oxidizing bacteria (FeOB) play a fundamental role in the precipitation of minerals that form the deposits because they are extremely efficient at facilitating the oxidation of reduced iron from the vents (Emerson et al., 2010).

There have been few observations of in situ diffuse flow hydrothermal systems. Most studies have recovered samples by dredging or coring (De Carlo et al., 1983; Murnane and Clague, 1983; Dekov et al., 2007), thus the venting configuration of these systems is poorly documented. In 2015 at Seamount 3 in the Wolf-Darwin lineament of the Galapagos Archipelago, a sinuous winding tubular network of low-temperature diffuse hydrothermal deposits was observed for the first time. Studies by Alt (1988) and McMurtry et al. (1993) are the only reports to date with photo documentation of authigenic diffuse flow in situ; although the appearance and pattern of the deposits described in these papers do not match that of the present study.

Understanding these low-temperature seafloor systems is important for evaluating geochemical exchanges with the ocean and alteration of the ocean crust. In addition, the presence of such systems may provide clues to the location of sub-surface massive sulfide deposits, which are of economic significance (Murnane and Clague, 1983; Çağatay, 1993). Current models suggest that diffuse flow systems with microbially facilitated Fe-rich deposits are rooted with sulfide deposits that are produced by deposition from hot fluids in the subsurface (Murnane and Clague, 1983; Humphris et al., 1995; Blumenberg et al., 2007; Figure 1.3).

The purpose of this thesis is to study the composition, structure, and origins of the unusually patterned network of hydrothermal mineral deposits that were discovered in 2015 at the summit of Seamount 3, near the Wolf-Darwin lineation (Galapagos archipelago). Three primary questions are investigated in this study: (1) what is controlling the distribution of the fluid flow to generate the complex tubular pattern of the nontronite and Fe-Si-oxide deposits, (2) what is the temperature regime of this hydrothermal system, and what are the compositional characteristics of the mineral deposits, and (3) is the hydrothermal mineralization being facilitated by bacterial activity?

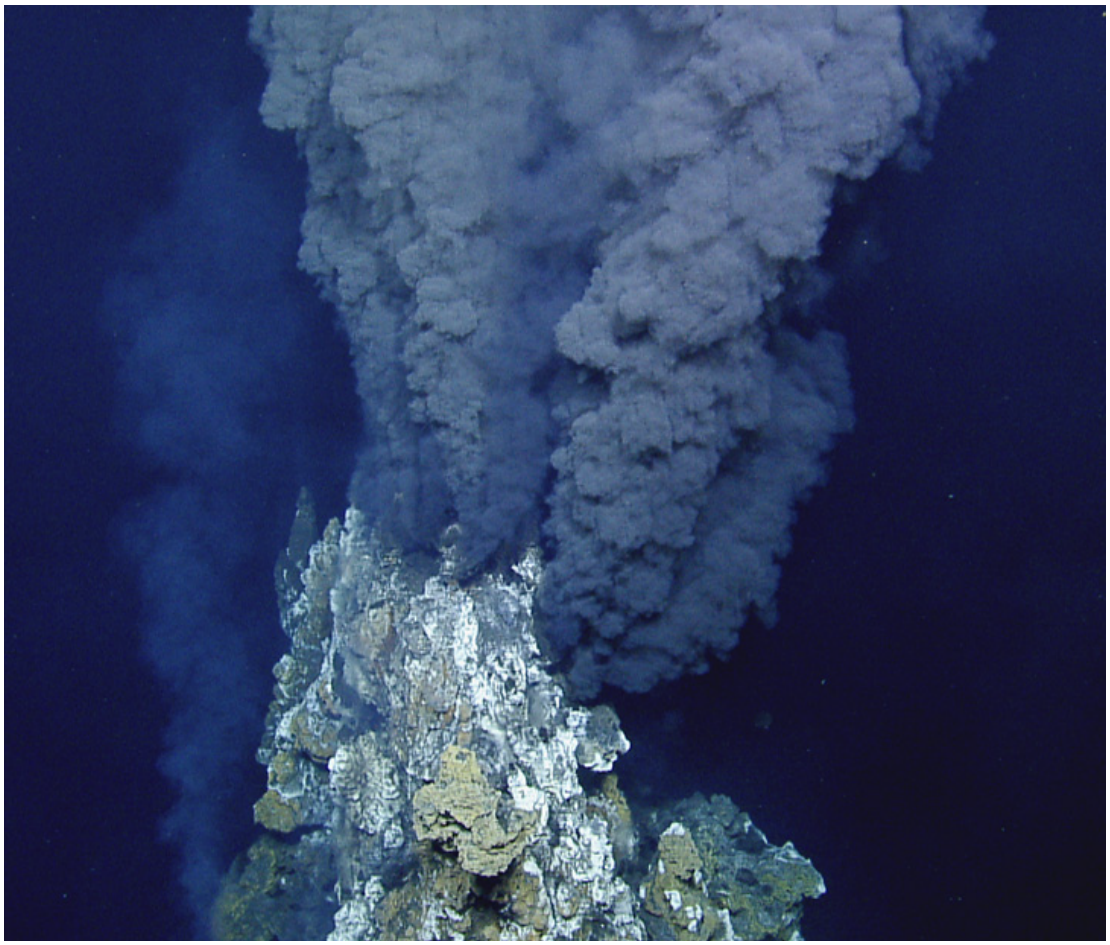

Figure 1.1 High-temperature black smoker vent from Iguanas-Pinguinos hydrothermal area of the Galapagos Spreading Center. The width of the base of this smoker is approximately 2-5 meters. Image collected during cruise NA064 of the E/V *Nautilus* and provided courtesy of the Ocean Exploration Trust.

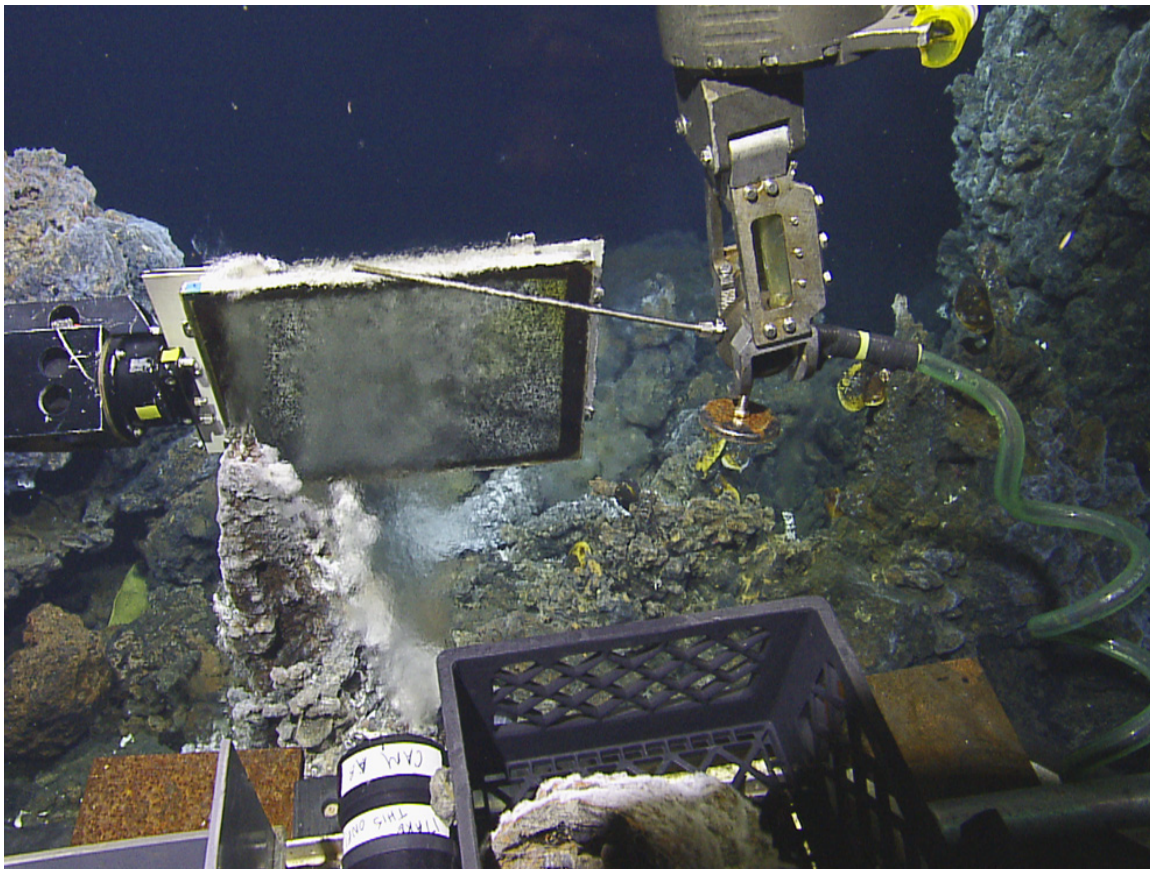

Figure 1.2 Low-temperature diffuse venting producing shimmering water at the Iguanas-Pinguinos hydrothermal area on the Galapagos Spreading Center. The right manipulator arm is clutching the temperature probe while the left arm is holding up a tool used to calculate the velocity of diffuse hydrothermal flow through noninvasive means by tracking moving refractive index anomalies through diffuse flow velocimetry and particle image velocimetry (Mittelstaedt et al., 2010). The width of black plastic crate (rock box) in foreground of image is 0.3 meters (1 foot). Image collected during cruise NA064 of the E/V *Nautilus* and provided courtesy of the Ocean Exploration Trust.

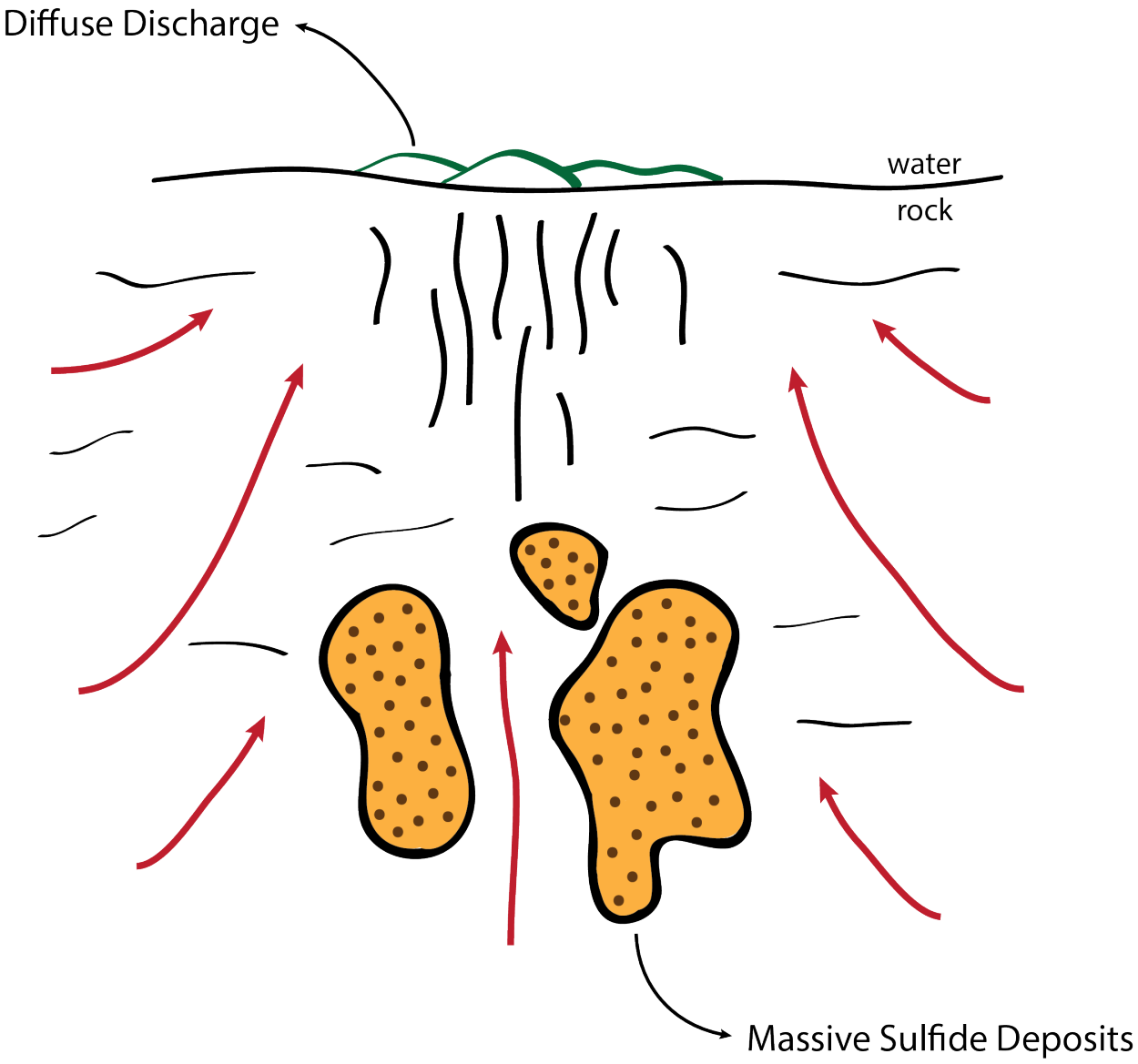

Figure 1.3 A 2-D cross-section showing the formation of massive sulfide deposits below the ocean floor while a low-temperature diffuse hydrothermal system discharges on the seafloor. Illustration inspired from Murnane and Clague (1983).

1.2 Seafloor hydrothermal activity

1.2.1 Tectonics and seafloor volcanism

The lithosphere, the earth's rigid outer shell comprised of the upper mantle and the crust, is separated into several plates varying in size, which move atop of the visco-elastic asthenosphere (Winter, 2001). Tectonic plates are approximately 150 km thick and may collide at convergent boundaries, come apart at divergent boundaries, or slide back and forth at transform faults (Cox and Hart, 2009). Most of the earth's tectonic activity occurs deep underwater in the world's oceans since the oceans cover more than 70% of the earth's surface. Volcanism refers to several different processes and features that cause the expulsion or release of molten rock, pyroclastic fragments, or hot water and steam. Volcanoes and geysers are common terrestrial geologic features that may cause surficial discharge.

Within the world's oceans there are two fundamental petrogenetic provinces (Winter, 2001). The first and most common form of volcanism occurs at plate boundaries, both convergent and divergent. Perhaps the most notable feature of this type of volcanism is the mid-ocean ridge system, which is considered the longest mountain chain in the world. This form of volcanism is how most oceanic crust or mid-ocean ridge basalts (MORB), primarily composed of tholeiitic basalt, are produced (Winter, 2001). New crust is generated at seafloor spreading sites, or divergent boundaries, such as the mid-ocean ridge system. When two plates diverge from each other the mantle flows upward to fill the open space made between the plates. The upper mantle, the deeper side of a plate, is mostly comprised of lherzolite, an ultramafic igneous rock, which is brought upward with mantle flows and undergoes a process called adiabatic decompression (Winter, 2001). Adiabatic decompression melting occurs when the conductive heat loss is nearly zero such that the rising mantle melt will follow a standard curve, called an adiabat, for these conditions (Winter, 2001). This process allows rising mantle material to follow a temperature-pressure slope that is actually shallower and more similar to the solidus curve (Winter, 2001). These flows will produce basaltic partial melt once they reach the solidus temperature (Winter, 2001). Eventually, this basaltic partial melt will rise further up and separate where it hardens to form new basaltic seafloor at the edge of the two diverging plates. The genesis of new crust at these sites form elevated ridges at the edge of each plate that resemble mountain chains.

Although the most common form of submarine volcanism is associated with mid-ocean ridges and plate boundaries, the second form does not occur at plate margins and thus is referred to as intraplate or hot-spot volcanism. Basalt is also the primary magma type for intraplate

volcanism, but in order to specify its origins it is called ocean island basalt (OIB) rather than MORB (Winter, 2001). Although both forms of volcanism do share some similar features and properties, intraplate volcanism has a fairly unique chemical signature making it a separate petrogenetic province (Winter, 2001). While intraplate volcanism is far less common than mid-ocean ridge volcanism, it is also much more variable as well, creating many different products that may have distinct petrography and chemical characteristics (Winter, 2001).

Seamounts are among some of the most common products of intraplate volcanism on the seafloor. Seamounts are similar to islands and form in parallel ways but they are below the surface of the water. Often seamounts are just old eroded islands or young formations that have not yet reached the surface. According to the Global Seamount Census, there are likely more than 100,000 undetected seamounts that are greater than 1 km in height, and possibly up to 25 million seamounts that are greater than 100 m in height (Wessel et al., 2010). Seamounts are sometimes formed near ridge systems or fracture zones, which provide conditions for hot spots to form (Cox and Hart, 2009).

Hot-spot volcanism can occur as a mantle plume rises up due to temperature or chemical anomalies coming from the lower mantle and sometimes even deep within the core. These spots are considered relatively stationary in geographic space while plates move above them. Seamount chains or island chains will indicate plate motion due to the nature of these stationary hot spots. The progression from older to more recently formed features are highlighted in chains, thus indicating the direction of the plate motion. The Galapagos Islands are an excellent example of this product of seafloor intraplate volcanism.

Islands and seamounts are formed as separate structures with space between them because the production of magma at hot spots is often irregular. Another contributing factor for the gaps between seamounts is that the upper portion of the plume is pulled away from the deep heat source when the plate moves such that a new conduit must be created before another seamount may form (Winter, 2001). Mantle plumes are relatively narrow with a diameter often less than 100 km (Wyllie, 1988). The lithosphere expands due to the production of heat from these plumes. There are a number of possible sources of the original formation of a hot spot within the mantle or core. Some of these sources include plumes made up of hotter less dense material that subsequently rise (Anderson, 1975); general temperature anomalies in the core or lower mantle; and possibly rising buoyant melts from lowered melting points due to volatile influxes (Winter, 2001).

Seafloor volcanoes initially form from these mantle plumes, which eventually build into larger and perhaps volcanically inactive seamounts. It is common to observe basaltic lava flows at seamounts. There are three primary basalt lava flows: pillow, pahoehoe, and a'a (Peterson and Tilling, 1980). Pillow lavas are significantly more abundant than the latter two since pillow

basalts are often observed along the mid-ocean ridge system and at seamounts or intraplate volcanoes. As basaltic magma flows into the deep cold waters at the seafloor, a shell or rind will form along the outside of the elongate bulbous pillow. This outer shell is solid but also elastic so it may grow in size as more magma flows into it (Rakovan, 2005). These bulbs will eventually harden until they are no longer elastic and form a tubular or spherical lobe that can vary in size but may be about 1 m in diameter (Rakovan, 2005). As basaltic magma continues to flow up and outward, pillow lava may form on top of older layers of pillow lava. This can create pillow flows or large formations of stacked and overlain pillow basalts along steep slopes or gentle plains near seamounts and ridges. Basaltic lava flows that do not form as pillows will form as either lobate or sheet flows.

Mid-ocean ridge and intraplate volcanism often creates perfect conditions for hydrothermal systems to develop. These systems may be observed after active volcanoes have extruded pillow lavas and flows, and perhaps even when the seamount appears dormant (Winter, 2001). Hydrothermal systems may also form early in the stages of a seamount or ridge.

1.2.2 High and low temperature hydrothermal vent systems

Hydrothermal vents are features that typically form at spreading centers or hot spots when the surrounding seawater circulates through fractures and cracks on the seafloor where a heat source in the ocean crust fuels circulation of fluids. Hydrothermal vents are very common along the mid-ocean ridge system. The heat flow at ridges, in particular, is tremendously high and helps facilitate the movement of seawater through the crust. Submarine volcanoes or seamounts also provide a suitable environment for the formation of hydrothermal vents. As the seawater filters down into the fractured hot rock below, it alters minerals present in the oceanic crust. As it become buoyant it comes back out and this change causes dissolved elements to precipitate out as mineral deposits on the surface of the seafloor.

In 1977 the discovery of hydrothermal vents and their connection to chemosynthetic activity was not only geologically exciting but also biologically unexpected (Corliss et al., 1979). There is rich diversity of life at many hydrothermal vents where the source of energy for the basis of the food chain is not the sun but chemicals from the earth. Bacteria can synthesize energy through chemosynthesis, which is analogous to how plants synthesize energy from the sun through photosynthesis. Hydrothermal vents provide unique ecosystems for many different types of organisms to survive and thrive under seemingly remarkably hostile and dynamic settings.

One of the leading theories for the origin of life stems from the concepts surrounding the process of chemosynthesis. There are six stages of chemosynthesis that demonstrate the progression from earth-originated mineral rich hydrothermal fluids to the first living cell (Corliss et al., 1981; Martin et al., 2008). In general, this chemosynthetic theory suggests that the development of a living cell is likely to occur wherever the right chemical and physical conditions exist, and perhaps hydrothermal vents are ideal environments for these conditions. At hydrothermal sites lavas may discharge and remain active from less than ten years to over 50,000 years between eruptions (Hammond, 1997). These occurrences can lead to the formation of black and white smokers as well as diffuse flow systems that eventually harbor rich ecosystems (Delaney et al., 1998; Embley et al., 2004). Diverse biological communities are able to develop quickly after these eruptions even at sites that have been completely destroyed from volcanic activity.

There are major differences between hydrothermal vents of low temperatures compared to those of high temperatures, thus often hydrothermal systems will be classified into one of these two categories. High temperature hydrothermal systems occur when the mineral-rich water is heated up to temperatures that range typically from 350ºC to 450ºC and are at least over 100ºC (Sheirer et al., 2006). The fluid comes up to the surface in a channelized and vigorous discharge because there are very few fractures in the seafloor such that the fluids are directed to fewer openings. This channelized discharge creates chimneys such as black smokers or white smokers (Figure 1.1). High-temperature systems are more acidic at depth with pH levels ranging from 3-5, while pH levels in the effluent at black smokers may even be more acidic at about pH 2-3 (Harder, 1976; Murnane and Clague, 1988; Martin et al., 2008). There is less mixing deep in the crust at high-temperature vents since fractures are filled on the surface so the water to rock ratio below the surface is far less than it is for low-temperature sites (Stakes and O'Neil, 1982; Murnane and Clague, 1988). In comparison to smectites such as nontronite, more amorphous iron oxide precipitates are known to form as the temperatures increase at vent sites (Malahoff et al., 1982; De Carlo et al., 1983). It has also been found that both smectites and amorphous iron oxides tend to incorporate trace elements of high abundances within the hydrothermal fluid flow of high-temperature systems (Shanks and Bischoff, 1977; De Carlo et al., 1983).

Low-temperature hydrothermal systems are at temperatures that are less than 350ºC and often much less than 100ºC below the rock-water interface. The seafloor surface is highly fractured, which allows the discharge to be diffuse rather than channelized such that the fluid flow may escape through many cracks rather than a few channels. The highly-fractured nature of low-temperature sites yields a horizontal deposit rather than the vertical deposit often associated with high-temperature venting. Due to these fractures, there is also a tremendous amount of mixing of seawater in the crust such that the water-rock ratio is often very high (Murnane and Clague, 1988). Sulfides are deeper below the rock-water interface in the case of the low-

temperature systems while silica-iron-oxides are just below the surface and dissolved into the fluid (Murnane and Clague, 1988). There is evidence that massive sulfides may rest below low-temperature systems where the temperatures are higher (Murnane and Clague, 1988). When the hydrothermal fluids are released from the crust, it is common for nontronite to precipitate as well as some Mn-oxides; this is due to the nature of the water-dominated fluids at low-temperatures (Bischoff, 1980). These fluids are able to leach manganese and iron from the crust much more productively than hotter more concentrated fluids (Bischoff, 1980). Low-temperature systems are also less acidic, pH 4-6, at depth than their high-temperature counterparts (Harder, 1976; Murnane and Clague, 1983). The conditions and local settings largely affect which minerals will precipitate from the hydrothermal fluids. Nonetheless, it is understood that high-temperature sites are fairly abundant in silica-iron-oxides while nontronite and Mn-oxides are often more present at low-temperature systems (Murnane and Clague, 1988).

Overall, low-temperature hydrothermal systems have been significantly less studied in comparison to high-temperature channelized sites (Von Damm and Lilley, 2004; Sheirer et al., 2006). This is largely because diffuse sites are less extreme in appearance compared to black and white smokers such that they were not immediately recognized as hydrothermal systems (Sheirer et al., 2006). It is believed that diffuse flow systems may be indicators of potential future high-temperature systems as well as deep massive sulfide deposits. The filling in of fractures from repetitive seawater-crustal circulation during diffuse discharge may help establish surficial environments suitable for chimneys to form, as the heat source below perhaps becomes more directed and results in an increase in temperature for the system.

1.2.3 Nontronite

Nontronite [$(Ca_{0.5},Na)_{0.3}Fe_2^{3+}(Si,Al)_4O_{10}(OH)_2 \cdot nH_2O$] is the ferric member of the montmorillonite-beidellite-nontronite series of type I dioctahedral smectites (Deer et al., 1963). The layer charge of nontronite is typically within the tetrahedral sheet as nontronite contains a dioctahedral sheet that is made up of Fe^{3+} cations (sometimes substituted by Al^{3+} and Mg^{2+}) and a tetrahedral sheet composed of Si^{4+} (sometimes substituted by Fe^{3+} or Al^{3+}, or both). Typically, Ca^{2+} or Mg^{2+} will balance out this layer charge. In general nontronite is usually characterized as having about 40-50 wt. % SiO_2 and 30-40 wt. % Fe_2O_3 with additional trace elements (Deer et al., 1963).

Nontronite occurrences associated with hydrothermal activity have been discovered at several seamounts and seafloor ridges in Hawaii, the Eastern Pacific, the mid-Atlantic ridge,

and the Aeolian volcanic arc using drilling, coring, and dredging techniques (De Carlo et al., 1983; Murnane and Clague, 1983; Dekov et al., 2007; Dekov et al., 2010). There is only one known documented case of hydrothermally sourced nontronite explored in situ with photo documentation (Alt, 1988). These nontronite deposits were documented on the summit of Red Seamount near the East Pacific Rise (EPR) during an ALVIN dive (Alt, 1988). Although these deposits extensively covered the peak of Red Seamount, their appearance throughout this entire site did not match the venting configuration of the present study. Rather, they appeared to be more mounded and lacking in any clearly defined pattern (Alt, 1988).

There are also several occurrences of nontronite in terrestrial locations. Nontronite has been identified in soil systems throughout the world including Hawaii, Fiji, New Zealand, and Australia (Sherman et al., 1962). In Germany, Austria, France, and the United States, nontronite has been located in highly weathered zones of lava flows, in fresh basalt with highly altered peridotite nodules, within vesicles of weathering basalt, and as thin coatings around sand grains overlaying basalt (Köster et al., 1999). There are several documented locations of nontronite occurring as an alteration product of gneisses and slates (Ross and Hendricks, 1945; Isphording, 1975). There are multiple nontronite occurrences found throughout the Americas, Europe, Asia, Africa, and Australia that are similar in compositions but have formed through different processes, some involving bacterial and others not, some hydrothermal and others not.

Perhaps some of the more peculiar detections of nontronite, however, have been on Mars. Across various ancient and relatively modern surficial Martian terrains, nontronite has been identified via spectral observations detected using orbital data from the Compact Reconnaissance Imaging Spectrometer for Mars (Bibring et al., 2005; Poulet et al., 2005; Loizeau et al., 2007; Bishop et al., 2008; Wray et al., 2009; Ehlmann et al., 2011; Gainey et al., 2014). Although these occurrences are far from those identified on the seafloor at hydrothermally active locations and from those observed on land throughout Earth, many nontronite sites are similar in that they are spatially associated with basalt and sulfides.

Nontronite is also becoming known for its impressive potential uses in molecular engineering, as it is particularly common in bentonites, a well-known highly versatile group of clays that are predominantly comprised of smectites (Eisenhour and Brown, 2009). For more than 3000 years, bentonites have been utilized for medicinal purposes and cleaning products while recently their uses have become far more widespread in a number of industries such as metal casting, drilling and extraction (Eisenhour and Brown, 2009).

Hydrothermal nontronite formation often occurs at cool surface temperatures of about 20ºC to 80ºC under oxidizing conditions that are further followed by reducing conditions through the process of aging (Harder, 1976). Hydrothermal nontronite may also directly precipitate out from hydrothermal fluids, and can form from the alteration of seafloor sediments including

volcanic glasses and rocks. At low-temperature systems, nontronite may form through a reaction between Fe-Si-hydroxides. Finally, nontronite is also known to form through biologically-mediated processes that feature iron oxidizing bacteria (FeOB) and other microbes (further discussed in 1.2.5).

1.2.4 Massive sulfide deposits

Massive sulfides refer to sulfur-rich metal deposits formed from fluids containing metals such as iron, copper, zinc, and lead that were leached out of the crust by acidic hydrothermal fluids (Hoagland et al., 2010). These deposits are economically significant and have historically been mined in some locations such as the Western South Pacific, although the technologies and strategies used to exploit these deposits are environmentally controversial and in need of proper management strategies (Boschen et al., 2013).

Massive sulfides are products of hydrothermal processes and may precipitate out of hydrothermal fluids at the seafloor or below it. Buoyancy differences trigger hydrothermal fluids to upwell through the fractures in the crust which may eventually exit through a chimney as a channelized discharge or it may be discharged through several fractures as a diffuse discharge. As high-temperature fluids discharge out of black smokers, metal sulfides typically precipitate out to form massive sulfides that are rich in copper, zinc, and iron (Humphris and McCollom, 1998). This process occurs as the hydrothermal fluids mix with the cold seawater.

At low-temperature vent systems, the highly fractured seafloor allows seawater to permeate deeper into the crust such that the fluids moving up will mix in the subsurface rather than outside of a chimney (Figure 1.3). Sulfides will precipitate below the surface thus leaving the upward moving fluids depleted in metals. This is often how white smokers are formed rather than black smokers (Humphris and McCollom, 1998).

Overall, these interactions between hydrothermal fluids and seawater cause elements to precipitate out of the fluids and dissolve out from the seawater at various stages. The exchanges of various metals and compounds contribute to the regulation of seawater chemistry throughout all of the world's oceans (Humphris and McCollom, 1998).

1.2.5 Bacteria and biomineralization at hydrothermal systems

At some hydrothermal vent sites there are specific types of bacteria that are able to facilitate the oxidation of reduced iron. These are referred to as FeOB. FeOB were some of the first few groups of microscopic organisms that were recognized as facilitating geological processes such as the oxidation of iron as early as the 1830s (Emerson et al., 2010). FeOB are believed to have existed on Earth since the beginning of life, thus the study of their functionality and presence in a variety of environments may offer new perspectives on the relationship between biological organisms and the physical and geological processes on Earth (Emerson et al., 2010).

Many studies propose that microbial bacteria play a major role in the global cycling of various elements (Tazaki, 1999). Biomineralization is the process in which bacteria interact with dissolved elements to aid in the precipitation of minerals and chemical compounds. It is known that microbial mats provide conditions that support the precipitation of clay minerals as well as Fe, Mn, and Si (Tazaki, 1997; Ueshima and Tazaki, 2001; Li et al., 2012). Nontronite is a clay mineral that may form biogenically. Typical hydrothermal nontronite morphological structures are similar in scale and shape to that of microbial structures (Köhler et al, 1994; Ueshima and Tazaki, 2001). Often microscopic observations of nontronite include oblate spheroids and bulbous tubular filamentous structures, typically on the order of less than 1 to 10 **µm (**Köhler et al, 1994; Ueshima and Tazaki, 2001).

In order to form a protective boundary from the harsh conditions on the seafloor, specialized bacteria have the ability to form biofilms through the secretion of extracellular polymer substrates (EPS) (Dekov et al., 2010). The geochemistry of these secreted EPS offer highly reactive surfaces for Fe-Si-oxyhydroxides and thus act as a “template” for the synthesis of such oxides (Dekov et al., 2010; Ueshima and Tazaki, 2001). Nontronite formation and growth can occur within the EPS while Fe-Si-hydroxides typically were seen to form on the outside of the EPS (Ueshima and Tazaki, 2001). Nontronite formation under these conditions often exhibits a bulbous structure of honeycomb-like precipitates (Ueshima and Tazaki, 2001). This characteristic honeycomb fabric is believed to be present at initial formation of the hollowed-out nontronite microtubes (Köhler et al., 1994). As the hydrothermal system dies down, the degradation of the nontronite structures often appears more like finely layered clay sheets on the surface where secondary nontronite intergrowth may also occur (Köhler et al., 1994).

1.3 Low-temperature diffuse hydrothermal mineralization on seamounts

Low-temperature diffuse venting may occur at several different marine geological environments such as rift valleys, ridges, spreading centers, basins, and seamounts. Low-temperature venting with Fe-Si-oxide and nontronite formation has been observed at several seamounts throughout the world, notably including Seamount 5 and the Red Seamount (near the East Pacific Rise, EPR; Alt, 1988), the Eolo Seamount (Aeolian volcanic arc, Tyrrhenian Sea; Dekov et al., 2007), the Loihi Seamount (Hawaiian archipelago; De Carlo et al., 1983; Emerson and Moyer, 2002), and the Kasuga 3 Seamount (Northern Mariana island arc; McMurtry et al., 1993).

Diffuse flow on seamounts, in particular, has been encountered and documented but significant exploration and research focus has been placed on seafloor hydrothermal activity at ridges and plate boundaries rather than hotspot volcanoes and island archipelagoes. Alt's study (1988) is one of the earliest documentations of hydrothermal nontronite formation that includes in situ imagery via ALVIN. The summit of Red Seamount was purported to be covered in blue-green nontronite with Fe-Mn crusts, while at the summit of Seamount 5 deposits of hydrothermal Fe-oxides were observed to be at least 1 m thick (Alt, 1988). Imagery from Red Seamount show oxide deposits in small mounds against a near-vertical surface (Figure 1.4; Alt, 1988). The geochemical analyses of these nontronite deposits are consistent with previous studies of seafloor hydrothermal nontronites (Table 1.1 and 1.2). Alt (1988) described the nontronite as having a striking color zonation in the crust of the deposits with the mineralization occurring across a strong oxidation gradient. Observations such as layers of oxides can assist in understanding the Eh, or oxidation-reduction (redox) potential, of the system and thus the overall conditions or setting for the formation of the deposits. Every chemical species has a specific Eh that describes its potential to be reduced. The reference point is H, (which is similar to pH) in that all species are compared to the reduction potential of H. A higher Eh refers to a stronger affinity for electrons, which results in the species being reduced more readily (Stumm and Morgan, 1981). The exterior being more oxidized, Alt (1988) described how FeOB play a surficial role in the growth of an exterior layer of Fe. A formation temperature for nontronite from this seamount was determined through $d^{18}O$ isotopic analysis to be about 30-40ºC (Alt et al., 1987).

Kasuga 3 Seamount was also explored and documented with ALVIN (McMurtry et al., 1993). At Kasuga 3, fresh lava flows were coated in orange Fe-oxide deposits and these crusts were described as broken apart while forming a network of fissures that had been delineated by black Mn-oxides. Three samples were collected, one of which included a massive clay

(nontronite) that had developed out of a crack in the seafloor (McMurtry et al., 1993). Again, it was described as having layers of Fe- and Mn-oxides that contained small vent chimneys or orifices. The major element chemistry from this particular seamount is outlined for comparison in Table 1.1 as well. Again, a distinct layering gradation was discussed by McMurtry et al. (1993) to be a result of an oxidation-reduction gradient. Through oxygen isotopic analysis, the formation temperature for this hydrothermal authigenic seamount nontronite was determined to be 22.5ºC (McMurtry et al., 1993).

Seafloor hydrothermal fields within the Hawaiian island archipelago have been explored at several sites. The summit of the Loihi Seamount (a submarine shield volcano) has been sampled and surveyed a number of times (Malahoff et al., 1982) revealing glass-covered pillow basalts and several fields of hydrothermal nontronite and Fe-oxides. In an effort to expand on some of the previous studies exploring hydrothermal venting at Loihi, De Carlo et al. (1983) documented the mineralogy and geochemistry of dredged nontronite and Fe-oxides at Loihi. They concluded a formation temperature possibly ranging from 31-57ºC from oxygen isotope analysis (De Carlo et al., 1983). A strong oxidation-reduction gradient was also suggested in order to explain some of the layering of colored materials in the dredged samples. X-ray diffraction analyses showed a distinctive nontronite pattern from a greenish subsample of the dredged material (Figure 1.5). De Carlo et al. (1983) describe a notable general trend that amorphous Fe-oxide, nontronite Al/Fe ratio, and trace element concentrations all increase or enrich while $d^{18}O$-derived formation temperatures also increase.

There are also rich communities of FeOB at Loihi Seamount that have been imaged and documented by Emerson and Moyer (2002) with the deep-sea submersible *Pisces V*. Although there was no nontronite recovered at this site, these hotter vent sites were extensively covered in Fe-oxides and their corresponding FeOB communities (Figure 1.6).

Dekov et al. (2007) described microscopic morphological features of nontronite (Figure 1.7) sourced via sediment coring atop the Eolo Seamount. SEM micrographs show distinct hollowed out nontronite morphologies that are associated with biogenic formation (Alt, 1988; Köhler et al., 1994; Ueshima and Tazaki, 2001; Li et al., 2012). Dekov et al. (2007) suggested a bacteria mediated formation of nontronite through the aging of the hydrothermal precipitates coating the bacterial filaments leading to the hollowed out morphology of the smectite.

Figure 1.4 Surficial oxide deposits from a near-vertical surface on the summit of Red Seamount. Imaged from ALVIN, disturbed sediments on left of image are a result of the manipulator arm's sampling efforts. Image from Alt (1988).

Table 1.1 Major element geochemical data for nontronites from 15 comparable studies. All values are presented in weight %.

Reference	Eolo Seamount	Red Seamount	Juan de Fuca Ridge	Loihi Seamount	Galapagos Rift	Galapagos Mounds	Explorer Ridge	Red Sea
	Dekov et al. (2007)	Alt et al. (1987)	Murnane and Clague (1983)	De Carlo et al. (1983)	Corliss et al. (1978)	Hékinian et al. (1978)	Grill et al. (1981)	Bischoff (1972)
Sample #	T/77-29 (113-5)	1183-14/15	TT152-11G	20-2G	N2	DSDP L54 bulk	69-11-2	average
SiO_2	46.70	50.30	46.70	56.60	53.00	50.80	46.40	36.60
Al_2O_3	4.45	0.01	0.32	2.71	0.04	0.35	1.59	2.45
Fe_2O_3	28.10	33.60	33.30	25.50	33.10	29.50	29.30	31.60
FeO	-	-	0.40	-	-	-	0.11	-
MnO	-	0.13	0.04	0.04	0.23	0.11	0.29	0.45
MgO	1.16	3.49	2.80	2.94	2.80	3.70	3.22	1.26
CaO	1.16	0.35	0.40	1.04	0.11	0.30	0.50	0.43
Na_2O	1.32	0.49	1.00	2.00	1.39	2.05	1.07	2.71
K_2O	0.89	4.06	3.40	0.61	2.24	3.24	2.87	0.78
P_2O_5	-	-	0.04	-	-	-	-	-
TiO_2	-	-	0.02	0.76	-	0.03	0.13	-
LOI	16.30	-	11.24	-	-	9.94	13.92	19.30
H_2O	-	-	-	-	-	-	-	-
Total	100.10	92.40	100.60	92.20	-	100.02	99.40	95.6

(continued)

Reference	Red Sea	Bauer Basin	FAMOUS	EPR 18°S	Lau Basin	TAG	Kasuga 3 Seamount
	Cole (1988)	Dymond and Eklund (1978)	Hoffert et al. (1978)	Dill et al. (1994)	Stoffers et al. (1990)	Severmann et al. (2004)	McMurtry et al. (1993)
Sample #	10094 252-260	average	average	RS 1	SO 35 KD80	2901-2	S-8b
SiO_2	46.40	52.30	39.70	42.20	58.70	49.40	53.90
Al_2O_3	0.35	2.44	0.24	0.05	0.23	0.30	0.71
Fe_2O_3	33.00	29.70	35.90	35.60	33.10	35.40	29.60
FeO	-	-	-	0.68	-	-	-
MnO	-	0.64	3.74	0.02	0.06	0.00	1.04
MgO	0.45	6.10	2.79	1.38	2.24	0.30	1.88
CaO	0.10	0.47	1.68	0.25	0.32	0.06	0.84
Na_2O	3.90	0.60	1.82	0.47	1.27	0.20	2.02
K_2O	0.10	2.04	3.03	0.20	0.62	1.00	1.50
P_2O_5	-	-	-	0.19	0.03	0.50	-
TiO_2	-	0.03	0.02	0.01	0.06	0.02	0.41
LOI	16.20	-	7.95	18.10	-	12.60	8.65
H_2O	-	-	-	-	-	-	-
Total	100.5	94.3	96.9	99.2	96.6	99.8	100.6

Table 1.2 Geochemical data for trace and REE of nontronite from ten previous studies. All values presented in ppm.

Reference	Eolo Seamount	Red Seamount	Juan de Fuca Ridge	Loihi Seamount	Galapagos Rift	Galapagos Mounds	FAMOUS	EPR 18°S	Lau Basin	TAG
	Dekov et al. (2007)	Alt et al. (1987)	Murnane and Clague (1983)	De Carlo et al. (1983)	Corliss et al. (1978)	Hékinian et al. (1978)	Hoffert et al. (1978)	Dill et al. (1994)	Stoffers et al. (1990)	Severmann et al. (2004)
Sample #	T/77-29 (113-5)	1183-14/15	TT152-11G	20-2G	N2	DSDP L54 bulk	average	RS 1	SO 35 KD80	2901-2
Ag	0.01	-	-	-	-	-	-	-	-	-
As	351	2	-	12	2.9	-	-	12	-	-
Ba	22	38	130	-	68	-	73	39	<10	-
Be	2.35	-	-	-	-	-	-	-	-	-
Bi	0	-	-	-	-	-	-	-	-	-
Cd	0.16	-	-	6.9	-	-	-	-	-	-
Co	1	1.6	1.13	43	0.91	22	5	<7	<10	-
Cr	5	2.7	4.8	45	4.1	11	9.5	<7	33	-
Cs	1.5	3.3	4.8	-	-	-	-	-	-	-
Cu	5.3	330	23	89	8	14	67	-	48	-
Ga	1	-	-	-	-	-	5	-	-	-
Ge	2.02	-	-	-	-	-	-	-	-	-
Hf	<5	0.05	0.12	-	-	-	-	-	-	-
In	0.003	-	-	-	-	-	-	-	-	-
Li	2	-	-	1	-	-	-	-	-	-
Mo	28	-	-	-	-	-	-	-	-	-
Nb	0.9	-	-	-	-	-	-	-	-	-
Ni	3	<45	-	118	14	16	49	<7	<10	-
La	2.7	0.17	2.01	-	2.2	-	-	-	-	0.46
Ce	6.3	0.22	4.17	-	2.3	-	-	<15	-	0.58
Pr	0.9	-	-	-	-	-	-	-	-	0.06
Nd	4	<3	-	-	-	-	-	-	-	0.26
Sm	1	0.05	0.71	-	0.49	-	-	-	-	0.07
Eu	0.24	0.01	0.19	-	0.15	-	-	-	-	0.11
Gd	1.1	-	-	-	-	-	-	-	-	0.05
Tb	0.19	<0.02	0.15	-	-	-	-	-	-	0.01
Dy	1.5	-	-	-	-	-	-	-	-	0.05
Ho	0.36	-	-	-	-	-	-	-	-	0.01
Er	1.27	-	-	-	-	-	-	-	-	0.03
Tm	0.23	-	-	-	-	-	-	-	-	0.00
Yb	1.65	0.02	0.56	-	0.30	-	-	-	-	0.03
Lu	0.28	0.08	0.10	-	0.03	-	-	-	-	0.00
Pb	3.9	80	-	340	-	60	-	135	<5	-
Rb	11	125	111	-	-	-	-	17	21	-
Sb	0.38	2	3.05	-	0.9	-	-	-	-	-
Sc	1	0.36	0.7	-	0.19	-	-	-	-	-
Sn	0.1	-	-	-	-	-	-	<3	-	-
Sr	71	-	50	-	-	-	223	14	66	-
Ta	0.06	0.02	0.05	-	-	-	-	-	-	-
Th	0.6	0.08	0.18	-	-	-	-	-	-	-
Tl	0.064	-	-	-	-	-	-	-	-	-
U	0.62	<0.15	0.16	-	-	-	-	16	-	-
V	18	-	-	-	-	-	94	22	45	-
W	7	-	-	-	-	-	-	16	-	-
Y	7.1	-	-	-	-	-	-	-	-	-
Zn	9	670	136	640	29	35	14	-	43	-
Zr	13	-	-	-	-	-	-	<7	-	-

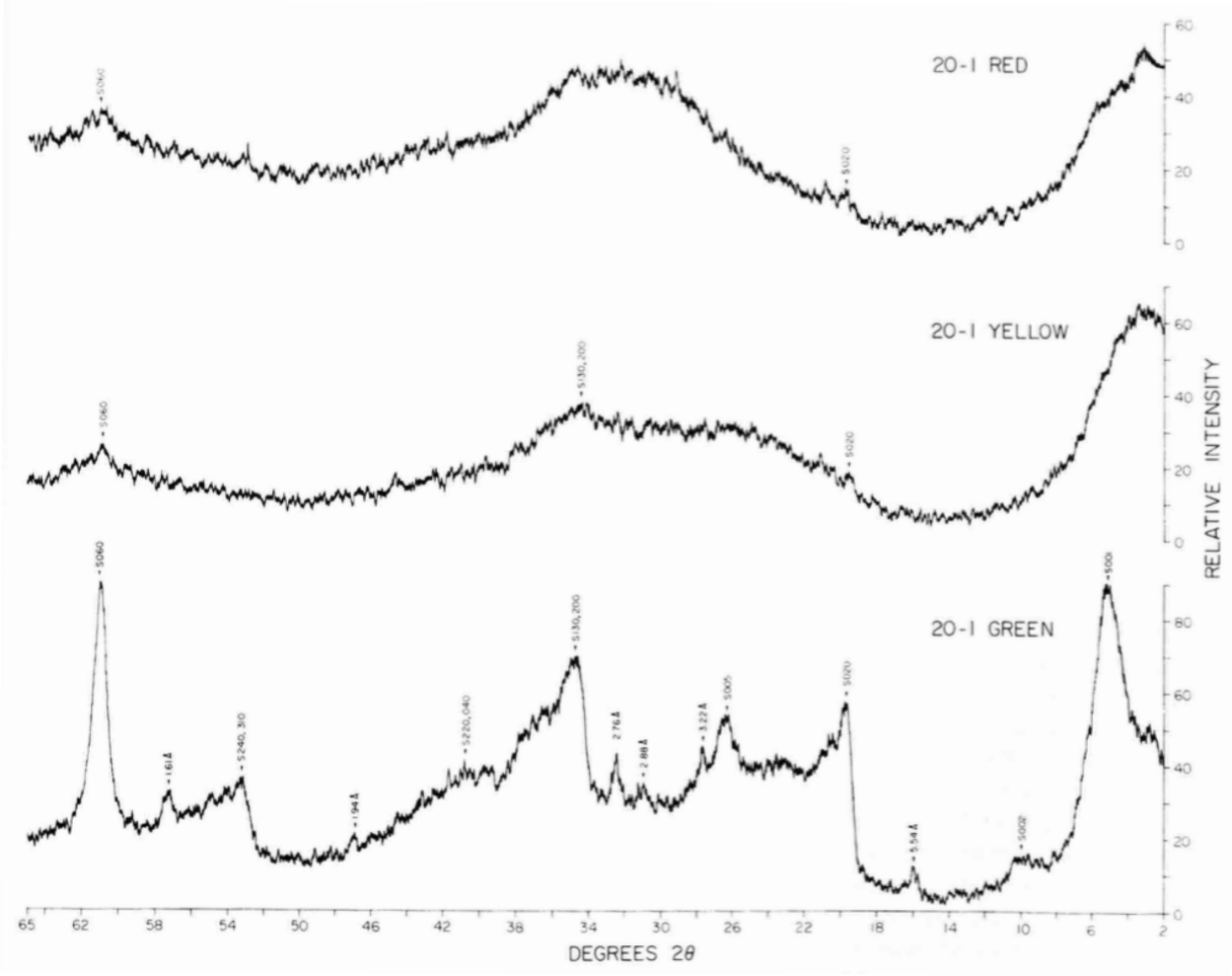

Figure 1.5 X-ray diffractograms of hydrothermal deposits from Loihi Seamount. 20-1 green is after 24 hours of exposure to ethylene glycol. S refers to smectite or nontronite peaks. Scan speed was at 2º 2theta/minute. (De Carlo et al., 1983).

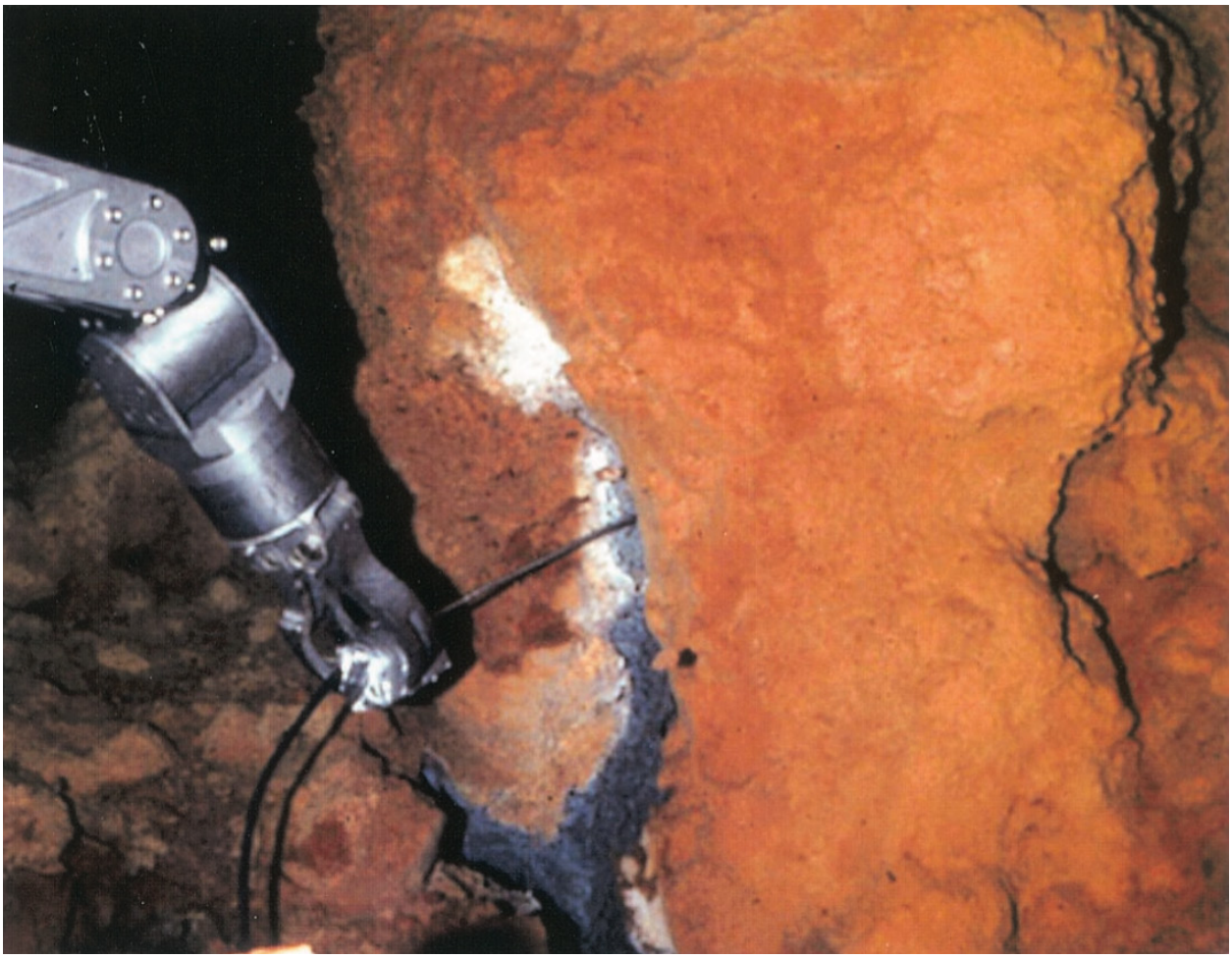

Figure 1.6 One of the Loihi hydrothermal vent locations described by Emerson and Moyer (2002). A temperature probe is being inserted into the vent opening. Image from Emerson and Moyer, 2002.

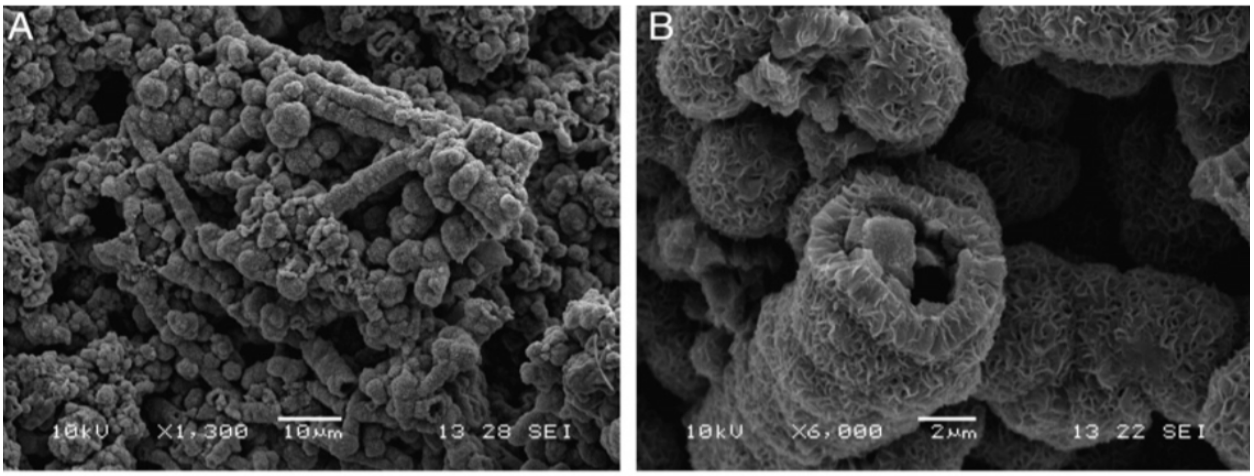

Figure 1.7 SEM micrographs of nontronite morphology. (A) filamentous aggregates of fine lamellar nontronite with microspheres. (B) nontronite lamellar crystals with distinct honeycomb appearance and hollowed out propagating filaments. Figure from Dekov et al., 2007.

1.4 Tectonic and regional geologic setting of the Galapagos Archipelago

The Galapagos Islands were formed by hot spot volcanism (Behn et al., 2004; Geist et al., 2006). Located on the northern edge of the Nazca plate, the Galapagos Islands are bordered by the Cocos plate to the north, the South American plate to the east, the Pacific plate to the west, and the Antarctic plate to the south. The Nazca plate is moving southeast at azimuth 91º in the hot spot reference frame (Gripp and Gordon, 2002) and subducting under the South American plate, while the Cocos plate is moving to the northeast (Figure 1.8). Thus the Galapagos Spreading Center formed from the opposing movement of the Cocos and Nazca plates.

The Galapagos Islands lie just south of the Galapagos Spreading Center and are the product of a mantle plume. The Galapagos Platform (light blue shallow region in Figure 1.9 and 1.10), the shallow ocean platform that the islands rest on, was formed as a result of the excess volcanism from a deep mantle plume. The Galapagos Platform consists of several subaerial islands and numerous seamounts (Geist et al., 2006). All dives (Figure 1.10) during the NA064 cruise were within the Galapagos Marine Reserve (GMC; Figure 1.9) and several were on seamounts (H1435, H1436, H1440).

Sinton et al. (1996) dredged several seamounts throughout the Galapagos in order to establish a geochronology for the Galapagos archipelago (Figure 1.10). In general, their findings confirm that the system models the movement of a hotspot with the age of the seamount and islands increasing with distance from the western side of the Galapagos Platform (Sinton et al., 1996). The Wolf-Darwin lineament or seamount chain in the northwest of the Galapagos Platform are the youngest (approximately 1 Ma or less) recorded seamounts in the region with the youngest being furthest south and closer to the platform (Sinton et al., 1996).

The Wolf-Darwin lineament or seamount chain consists of three seamounts and two islands (Wolf Island and Darwin Island; see Figure 1.9 or Figure 1.10). It is not entirely known how the orientation and placement of this lineament is controlled. There have been several possible formation theories presented, although none of which appear to be fully definitive based on the available evidence. Morgan (1978) has presented the possibility that this line of volcanic activity is a result of the vector sum of the absolute motion of the Nazca plate and north-trending jumps of the Galapagos Spreading Center. Others have considered the possibility that this lineament is on top of a fault that is rooted deep within the lithosphere (Feighner and Richards, 1994). Evidence for this particular formation theory is not as well supported, and would suggest random volcanism along the fault (i.e. no distinct age trend across the lineament), among other problematic assumptions (Morgan, 1978; Feighner and Richards, 1994). Sinton et al. (1996)

challenge these two formation models through their radiometric dating (as displayed in Figure 1.11). Due to a poorly defined age progression along the seamount chain, Sinton et al. (1996) are most in favor of a model rooted in lithospheric weakness (which does not require a linear age progression).

From these age observations, the Wolf-Darwin lineament may not fit the traditional hotspot model for volcanism. It is possible that there are several factors at play in this tectonically complex region. The Galapagos hotspot is likely affecting the activity of these seamounts, but their overall volcanic state may be mostly controlled by faulting and stress from the transform boundary and ridge interaction surrounding the north and eastern sides of the lineament (Sinton et al., 1996).

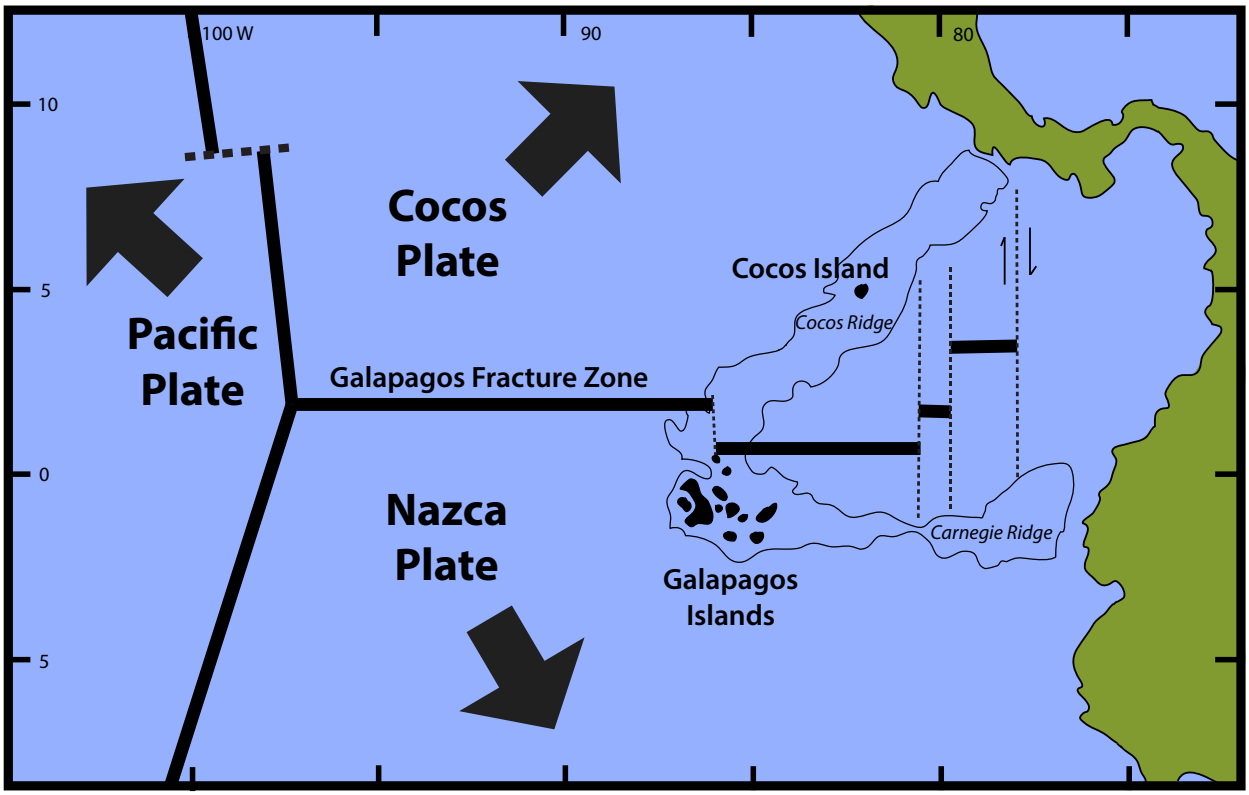

Figure 1.8 The tectonic setting of the Galapagos Islands in the Eastern Pacific. Figure based from models presented in Hey et al. (1972).

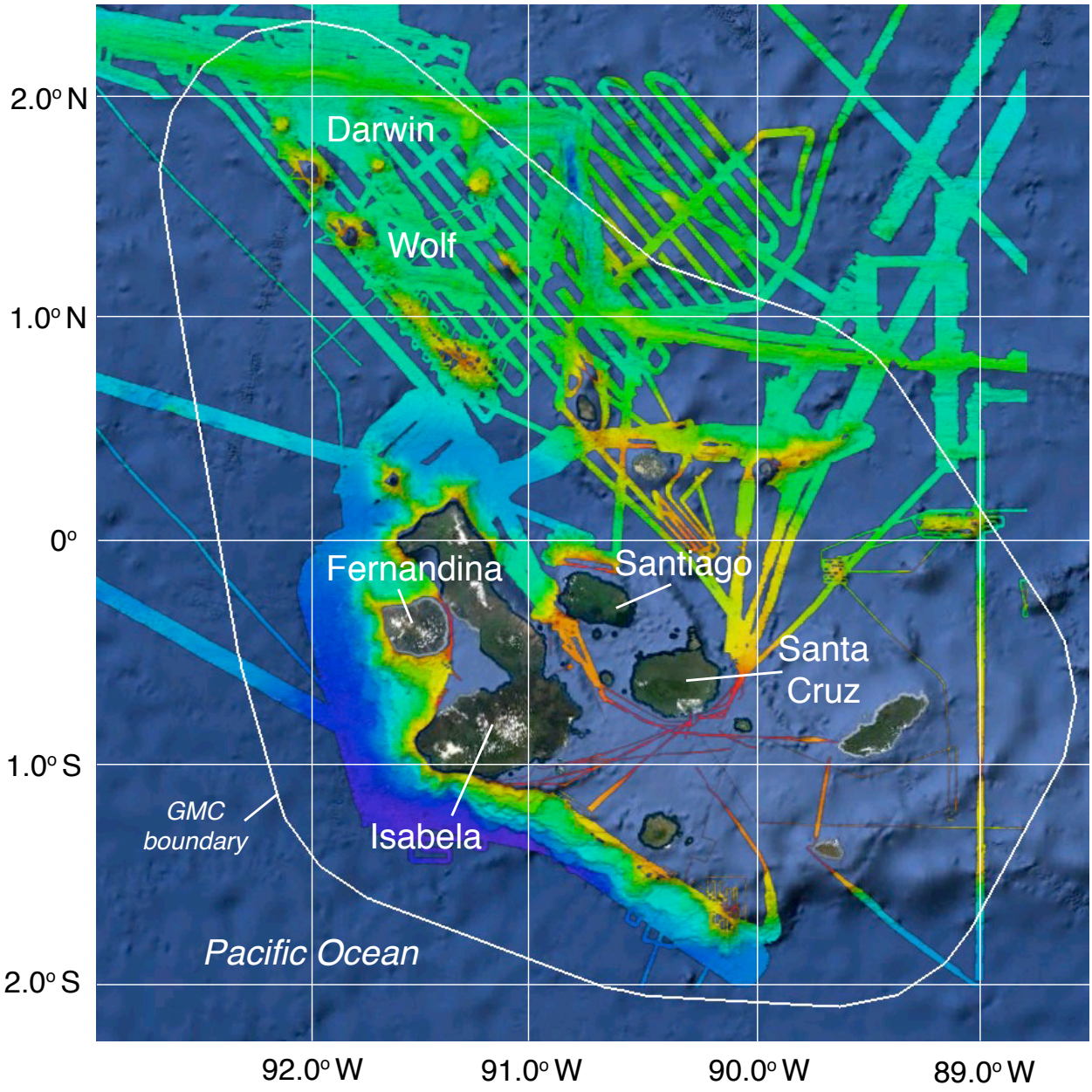

Figure 1.9 Operational area for cruise NA064 of the E/V Nautilus on the Galapagos Island platform. Boundary of the Galapagos Marine Reserve (GMC) shown in white. Multibeam bathymetric data courtesy of Woods Hole Oceanographic Institution.

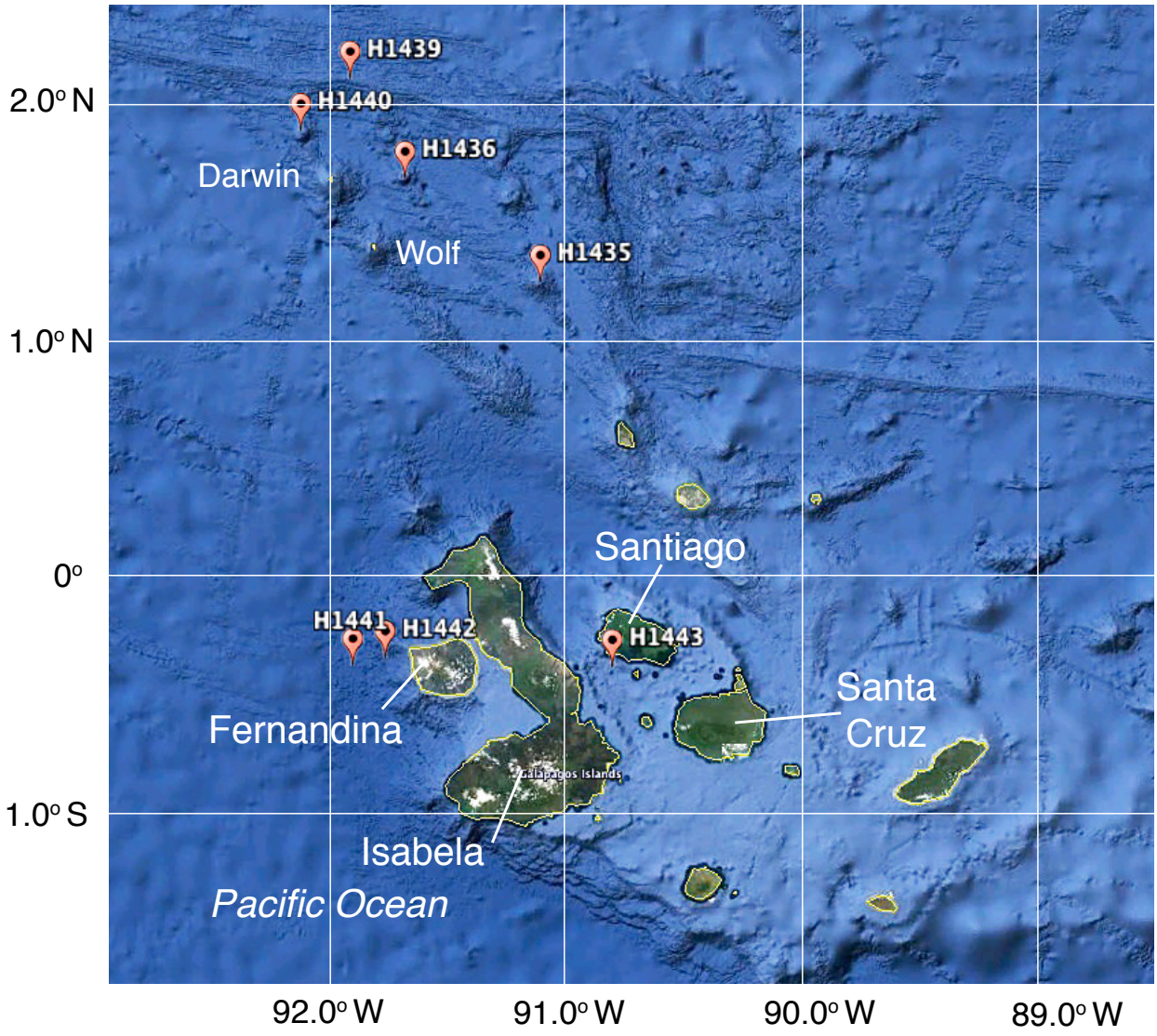

Figure 1.10 Location of all ROV dives completed during cruise NA064 around the Galapagos Islands. Hydrothermal deposits examined for this study were collected during dive H1440.

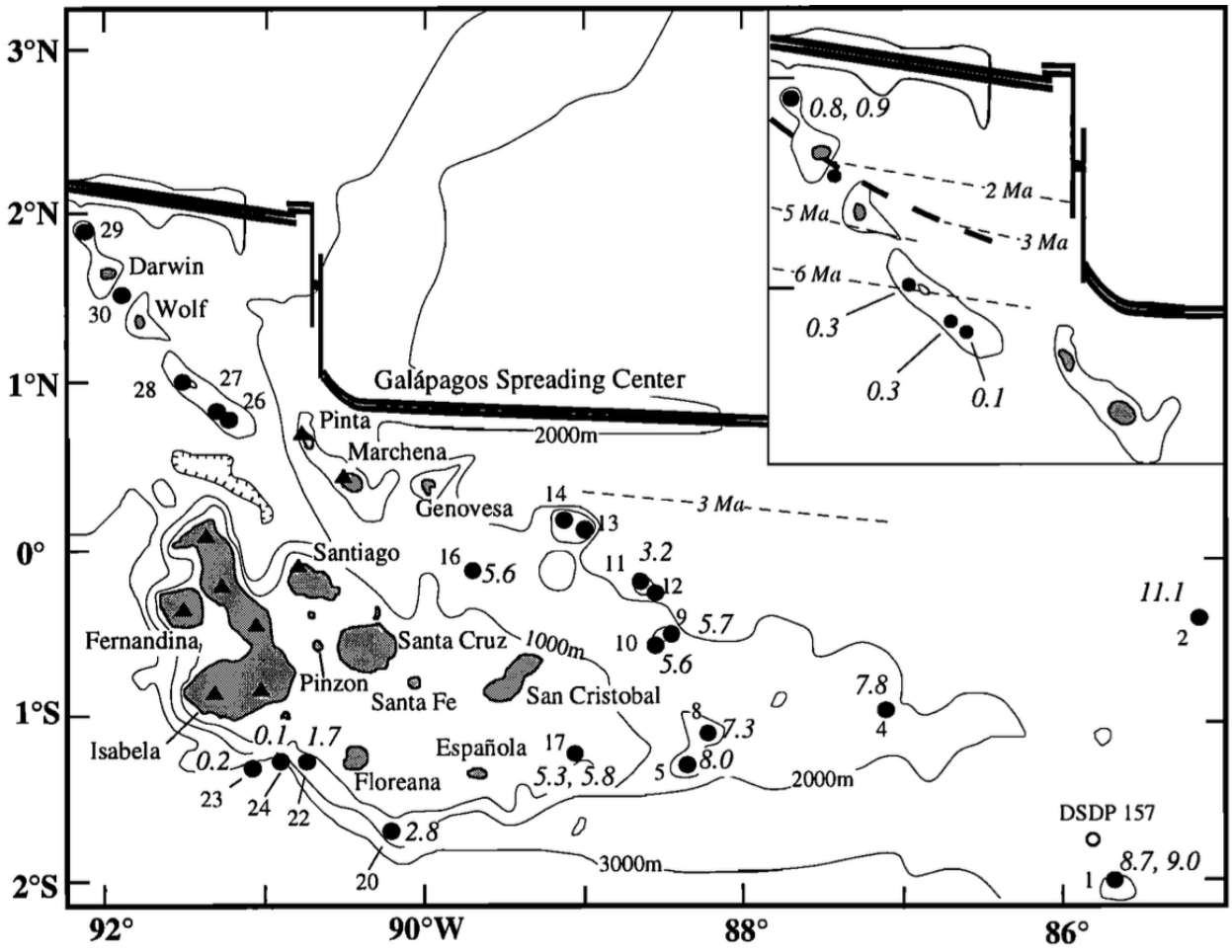

Figure 1.11 The Galapagos Archipelago with specific dredge sites labeled (by their sample numbers, 1-30) and radiometric ages (in italics). Seamount 3 (the focus of this thesis) is labeled as dredge site 29 in the Wolf-Darwin lineament. The inset map is a magnified view of the Wolf-Darwin chain with dashed lines showing the position of magnetic anomaly isochrones (approximated in location). The heavier dashed line represents the location of a pseudofault juxtaposing oceanic crust with ~ 1.8 m.y. difference in age. Figure and description directly from Sinton et al. (1996), with bathymetry and location of the GSC based on work by Wilson and Hey (1995) and unpublished SeaBeam data from Sinton et al. (1996).

2. Introduction

Nontronite is the ferric member of the montmorillonite-beidellite-nontronite series of type I dioctahedral smectites and is the most common hydrothermal clay mineral found in low temperature systems (Deer et al., 1963). Nontronite occurrences associated with diffuse hydrothermal activity have been discovered at several seamounts and seafloor ridges in Hawaii, the Eastern Pacific, the mid-Atlantic ridge, and the Aeolian volcanic arc (De Carlo et al., 1983; Murnane and Clague, 1983; Dekov et al., 2007; Dekov et al., 2010). However, there have been few direct observations of in situ nontronite-bearing hydrothermal deposits. Most studies have recovered samples using dredging or coring techniques (De Carlo et al., 1983; Murnane and Clague, 1983; Dekov et al., 2007). Only studies by Alt (1988) and McMurtry et al (1993) were associated with acquisition of seafloor imaging of the sampled and analyzed deposits.

Understanding diffuse flow low-temperature hydrothermal systems is important for evaluating geochemical exchanges with the ocean and alteration of the ocean crust (Tivey, 2007). Focused high-temperature venting contributes significantly to the overall hydrothermal flux in the oceans, but diffuse flow has been described as playing a major role as well (Bemis et al., 2012). In addition, the presence of such systems may provide clues to the location of sub-surface massive sulfide deposits, which are of economic significance (Murnane and Clague, 1983). Current models suggest that diffuse flow systems with Fe-rich microbially-facilitated deposits are rooted with sulfide deposits that are produced by deposition from hot fluids in the subsurface (Murnane and Clague, 1983).

In 2015 an expedition of the E/V *Nautilus* to the Galapagos Islands conducted remotely operated vehicle (ROV) explorations on seamounts to the north of the main Galapagos Islands. An unusual low-temperature diffuse hydrothermal system was discovered, explored, and sampled near the summit of a seamount adjacent to the Wolf-Darwin lineament. The nontronite-bearing hydrothermal deposits consisted of an extensive area of porous tubes developed in a sinuous pattern on the seafloor. Similarly patterned hydrothermal deposits, smaller in scale, were also observed at the summit of another nearby seamount, although no samples were collected.

In this paper, we report the major and trace element compositions of the nontronite-bearing deposits as determined by ICP-MS/ICP-AES and mineralogy inferred from X-ray diffraction. ROV vehicle imagery of the deposit and adjacent seafloor is used to develop a model for the formation of the unusual sinuous depositional pattern. SEM images provide insights into the potential role of bacteria in facilitating mineral deposition. New discoveries of such deposits suggest that low temperature diffuse hydrothermal systems are common features of many oceanic seamounts.

3. Regional setting

3.1 Wolf-Darwin lineament

The Galapagos Platform consists of several subaerial islands and numerous seamounts (Geist et al., 2006). The northern part of the Galapagos Platform includes many linear chains of seamounts that border the Galapagos Spreading Center (Figure 3.1). In this region, the spreading center is disjointed by a transform fault to the east leading down to the connecting Cocos-Nazca boundary in the southeast. The Wolf-Darwin lineament or seamount chain, which is in the northwest of the Platform, as well as the less-prominent seamount chains to the east, consist of several seamounts of varying ages, activity, and composition (McBirney and Williams, 1969; Nordlie, 1973; Sinton et al., 1996). The youngest (approximately 1 Ma or less) recorded seamounts in this region, the Wolf-Darwin lineament, are furthest south and closer to the platform (Sinton et al., 1996).

The Wolf-Darwin lineament consists of three seamounts and two islands (Wolf Island and Darwin Island; Figure 3.1). It is not entirely known how the orientation and placement of this lineament is controlled. From radiometric age analyses, Sinton et al. (1996) determined that the Wolf-Darwin lineament may not fit the traditional hotspot model for volcanism. There may be several factors at play in this tectonically complex region. The Galapagos hotspot is likely affecting the activity of these seamounts, but their overall volcanic state may be mostly controlled by faulting and stress from the transform boundary and ridge interaction surrounding the north and eastern sides of the lineament (Sinton et al., 1996).

3.2 Seamount 3, occurrence and morphology of hydrothermal deposits

Northwest of Darwin Island is a prominent and relatively young (~0.8-0.9 Ma; Sinton et al., 1996) seamount designated Seamount 3 in this study (Seamount 3; Figure 3.2). Seamount 3 is about 635 m high with its peak at the depth of about 1325 m and its base at a depth of about

1960 m. It is positioned at approximately 1.8837ºN and 92.1335ºW.

The base of Seamount 3 is covered by sediment with isolated pillow lava outcrops, and gradually transitions to patches of talus blocks along its south-east trending slope, which sharply lead into a dense lava talus slope with linear contact to a sedimented side west of 92.11ºW (Figure 3.2). It then transitions back to a highly sedimented seafloor with occasional isolated pillows further north and west upslope, which gradually turn into dense fields of pillow lava and then continues on northwest upslope into more sedimented regions.

Sinuous, overlapping tubular hydrothermal deposits occur near the summit of Seamount 3 (see star in Figure 3.2). This tubular network is partially covered in sediment. The deposits provide solid substrate for small stationary organisms to latch onto around the edges of the hydrothermal field. The patterned network becomes gradually denser and the sediment cover appears to diminish toward the summit. The hydrothermal deposits consist of approximately 20 cm wide tubes that are quite porous and friable (Figure 3.3).

The first sample collected, NA064-064, was of the deposits covered in yellow bacterial mats (Figure 3.3B). The second sample collected, NA064-065, was of the deposits within the same general region, which revealed an interlayered very friable bright green interior, yellow-orange oxidized exterior, and a dark thin crust (Figure 3.4; Figure 3.5).

For the remainder of the dive, the central crater (Figure 3.2) and peak of the seamount, both northwest of the hydrothermal deposits, shifted between mostly pillow lava outcrops and sedimented patches.

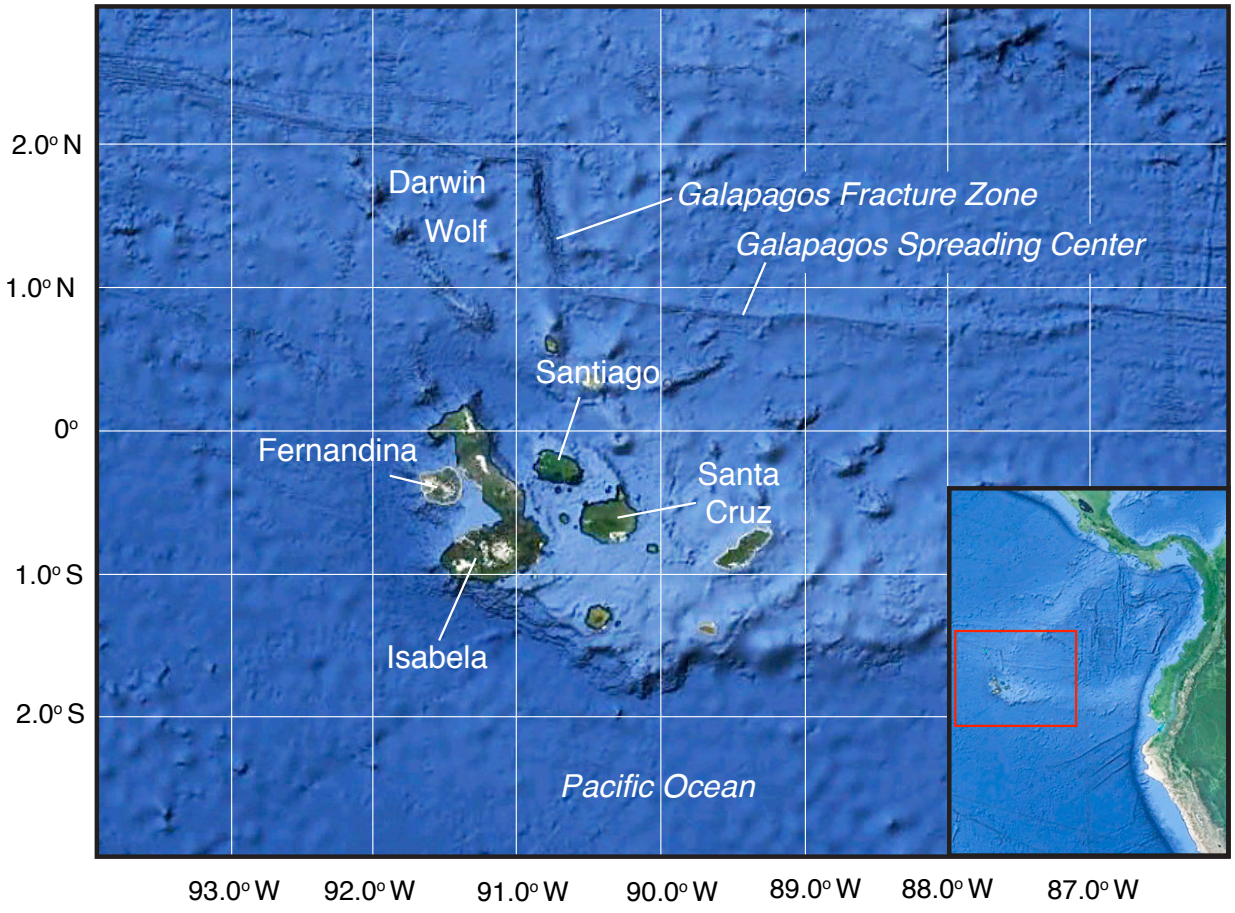

Figure 3.1 The Galapagos Platform (light blue region below islands) and adjacent Galapagos Spreading Center to the north. Inset map on the lower right shows position of the Galapagos Islands relative to South America.

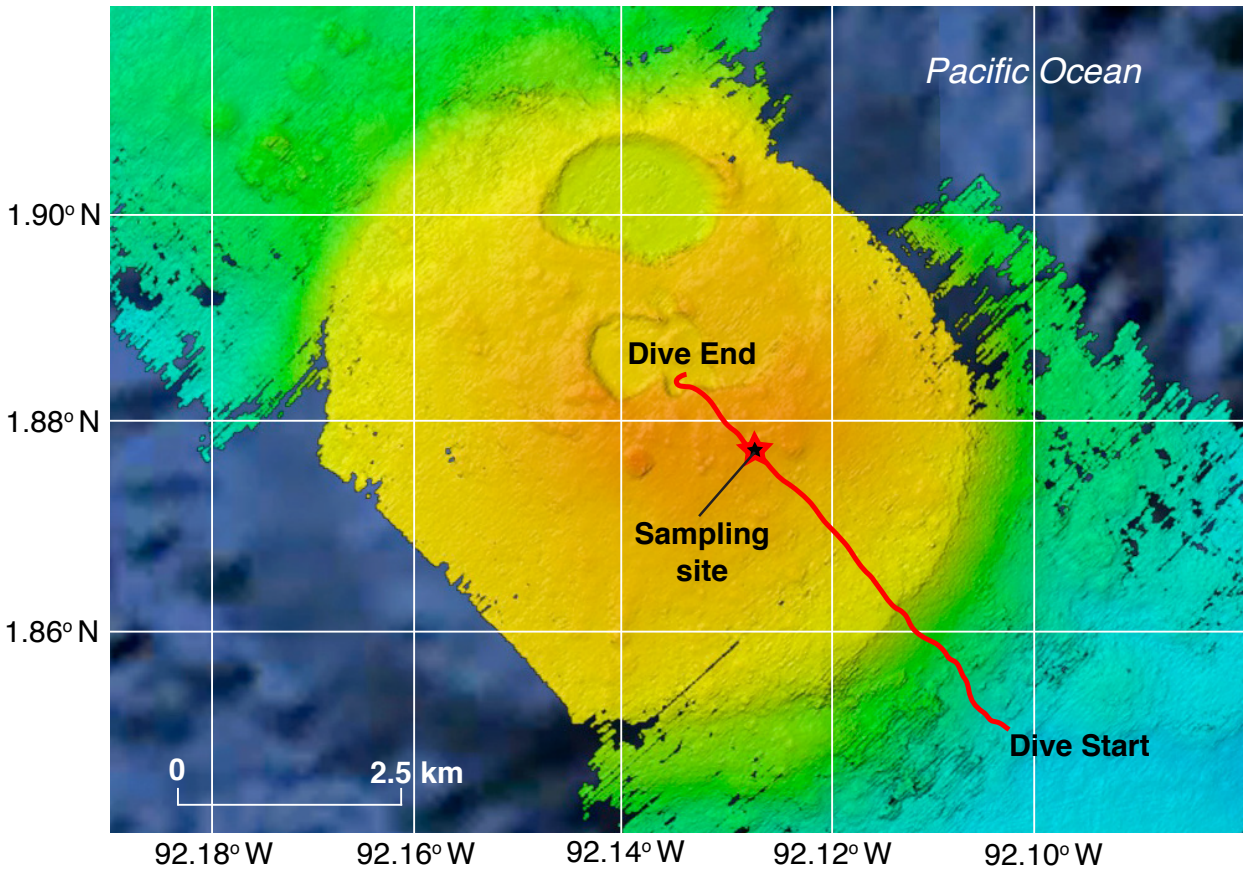

Figure 3.2 Multibeam map of Seamount 3 showing the ROV *Hercules* dive track (red) during dive H1440. Location of site where samples for this study were collected is indicated by the star. Water depth at start of dive was 1960 m and at end of dive was 1324 m. Multibeam bathymetric data courtesy of Woods Hole Oceanographic Institution.

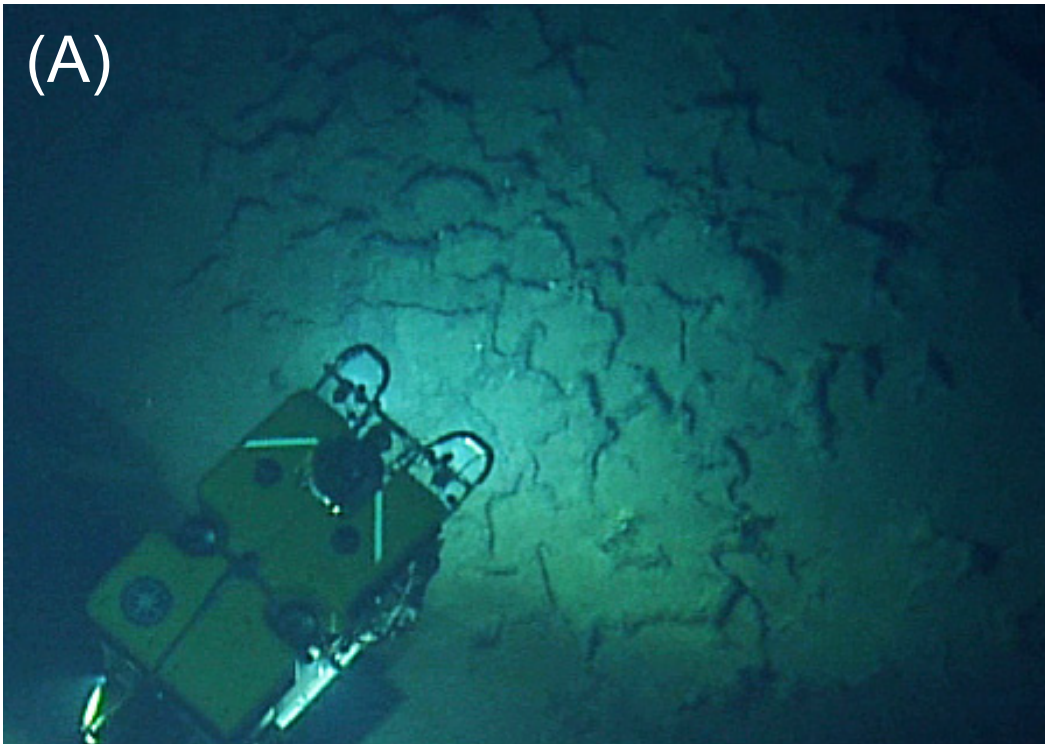

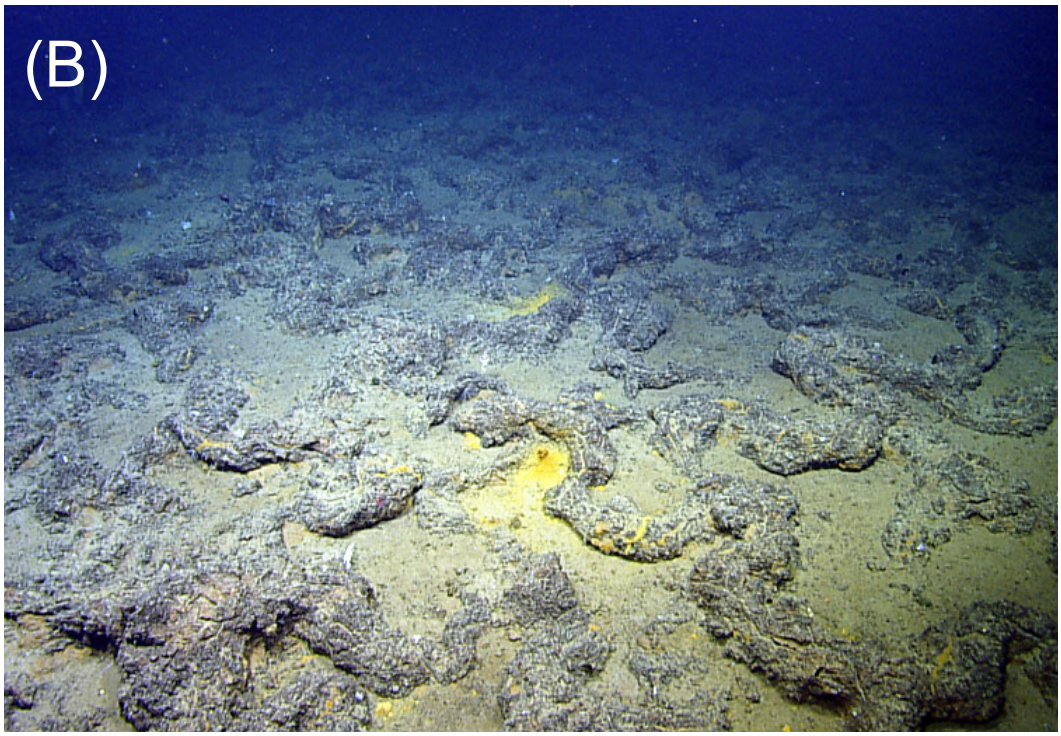

Figure 3.3 (A) Downward looking view from the ROV *Argus* above the ROV *Hercules* (lower left in image) showing the pattern of hydrothermal tube structures. Distance to seafloor from *Argus* is about 20 meters. (B) Tube-like hydrothermal deposits near the summit of Seamount 3. Tube diameter in the center of the image is about 20 cm across. Yellow bacterial mat in center of image. Image from dive H1440, and courtesy of the Ocean Exploration Trust.

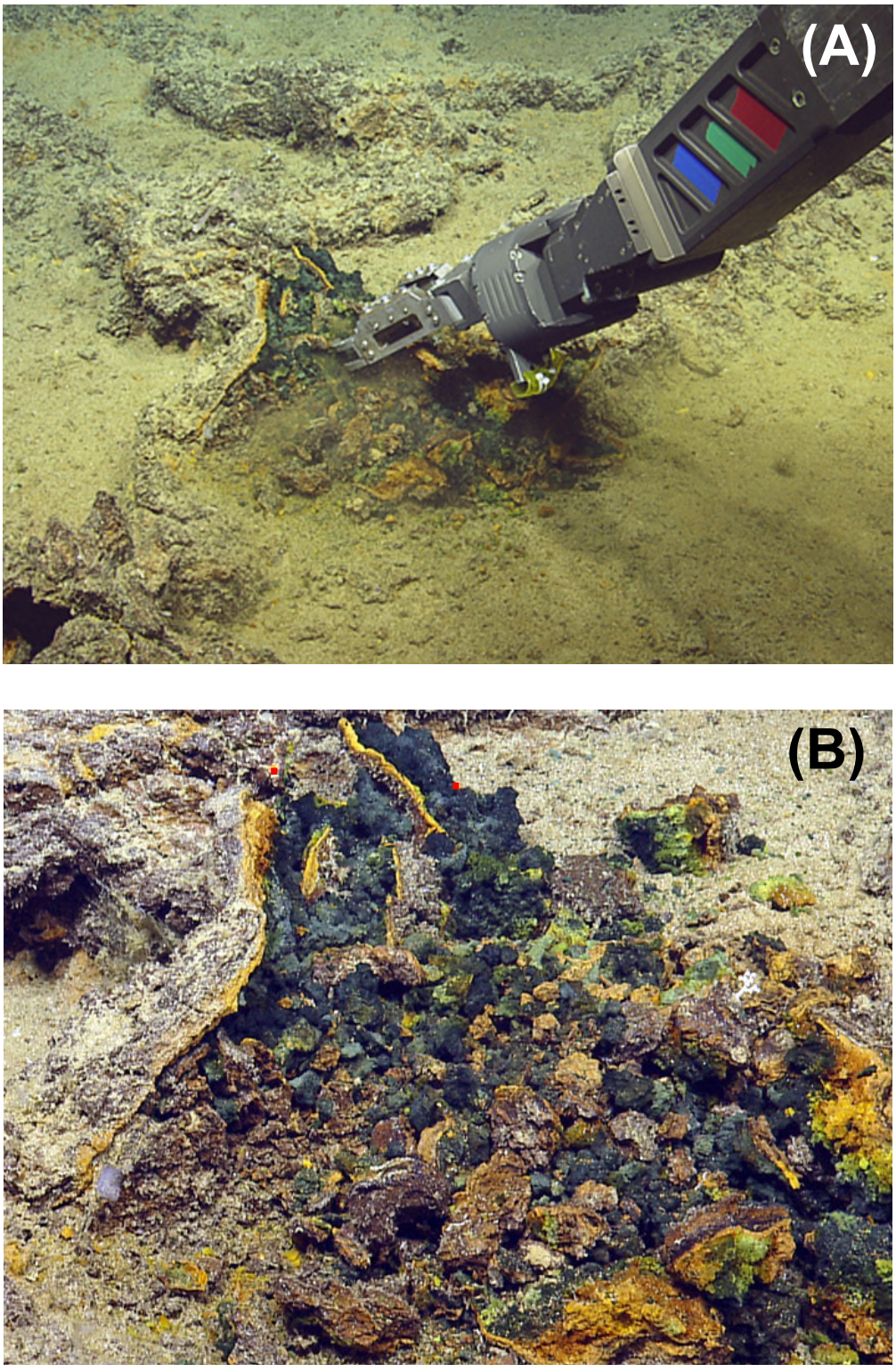

Figure 3.4 (A) Sampling of hydrothermal deposits by the remotely operated vehicle Hercules during dive H1440 in the Galapagos Islands. (B) Close up of the broken interior of a hydrothermal tube showing a strong gradation in color from deep green in the interior to yellow-orange on the exterior crust. The two red laser dots in the upper central part of the image are 10 cm apart.

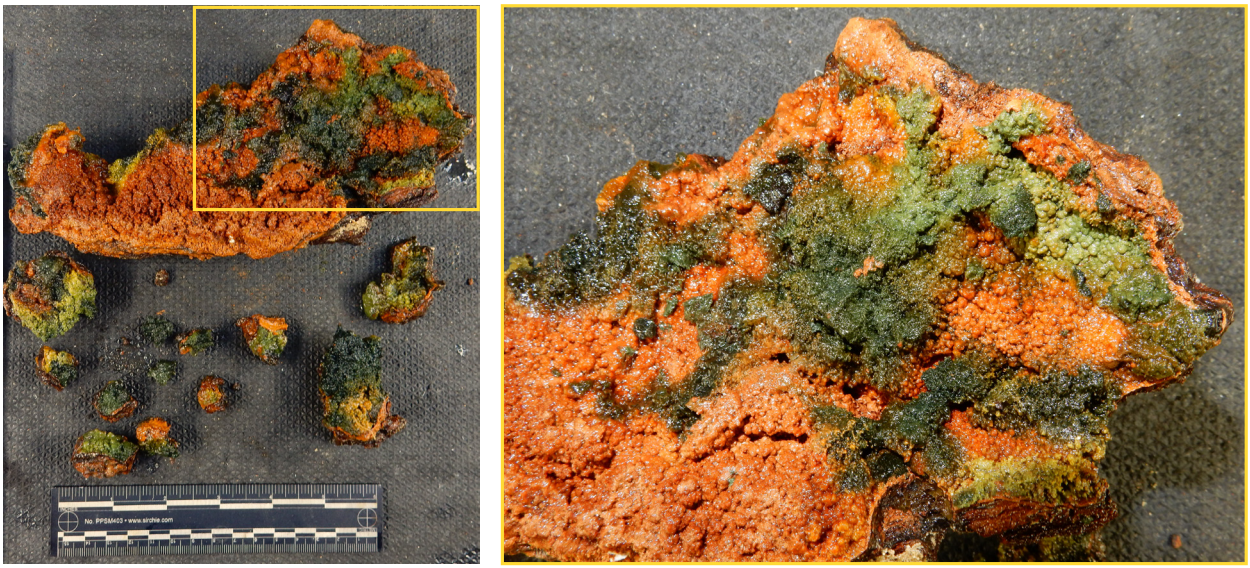

Figure 3.5 Sample NA064-065 interlayered and very friable imaged from the wet lab on the E/V *Nautilus*. Bright green interior and yellow-orange oxidized material with a dark thin outer crust. Right side is a magnified view of the left yellow box.

4. Materials and methods

Sampling of the deposits was performed with the *Hercules* ROV grab tool, a Kraft Predator Force Feedback Manipulator. This tool is a strong dexterous claw that can precisely clutch and store rock samples in the sample chambers on *Hercules*. Two similar samples (NA064-064; NA064-065) were collected from the field of deposits at the summit of Seamount 3 (Table 4.1). By breaking apart the tubular deposits, rocky material from the inside was exposed and collected as well as the crustal material.

Table 4.1 Sample locations and depth at sample locations on Seamount 3.

Sample ID	Latitude (ºN)	Longitude (ºW)	Depth (m)
NA064-064	1.87660315	92.12711038	1227.26
NA064-065	1.876802228	92.12706809	1226.31

Samples were air-dried and cataloged in the E/V *Nautilus* wet lab. Each sample was further divided into four sub-samples: green nontronite (NA064-064A; NA064-065A), bright rusty material with dark bands (NA064-064B; NA064-065B), orange material (NA064-064C; NA064-065C), and remaining bulk sample (NA064-064D; NA064-065D).

The mineralogy of the samples was characterized by X-ray diffraction (XRD), energy-dispersive X-ray spectroscopy (EDS), and scanning electron microscopy (SEM) at Bates College Carnegie Science Center. Fine powders were prepared for XRD analysis by crushing individual sub-samples in a Spex Mixer Mill. Each sub-sample was further ground wet in a mortar and pestle with ethanol. Sub-samples were air-dried and placed in a desiccator for one week. Samples were ground in the mortar and pestle a second time (dry) to a fine powder. Random powder mounts were prepared and scanned in the X-ray diffractometer (Rigaku MiniFlex II Desktop X-ray Diffractometer using Cu K_{α} radiation, 30kV, 15mA) from 2 to 80º 2θ, 0.8º/minute (0.04º/step and 3 seconds/step).

Carbon-coated specimens were prepared for EDS analysis while gold and palladium coated specimens were prepared for SEM analysis (JEOL JSM-7100FLV with a Noran System 7 EDS System) at Bates College Carnegie Science Center. For the EDS analysis, the voltage was set to 15 kV, the dead time was 25%, and the focal working distance was fixed at 10.0 mm. For SEM analysis, the secondary electron electron-micrographs were produced with voltages ranging from 3 kV to 5 kV and a focal working distance ranging from 12.5 mm to 16.6 mm. SEM

analysis was used to look for diagnostic nontronite and Fe-oxide morphologies.

The chemical composition of the samples was determined by inductively coupled plasma mass spectrometry (ICP-MS) for rare earth elements (REE), trace elements, and select major elements. Sample prep for ICP-MS (Thermo X-Series II quadrupole at the University of Rhode Island Graduate School of Oceanography) analysis involved dissolution of powdered samples in HF-HNO_3 acid digestion (methodology from Kelley et al., 2003). Concentrations of Li, Be, Sc, Ti, V, Cr, Co, Ni, Cu, Zn, Ga, Rb, Sr, Y, Zr, Nb, Sb, Cs, Ba, La, Ce, Pr, Nd, Sm, Eu, Gd, Tb, Dy, Ho, Er, Yb, Lu, Hf, Ta, Pb, Th, U, and major elements K and P were determined by ICP-MS. Standards and run conditions are consistent with those of Kelley et al. (2003).

The major element compositions were determined by inductively coupled plasma atomic emission spectroscopy (ICP-AES). Sample digestion for ICP-AES (Perkin Elmer Optima 3100 XL at the University of Rhode Island) analysis involved preparing solutions using $LiBO_2$ flux-fusions (Klein et al., 1991; Miller et al., 1992; Kelley et al., 2003). Concentrations of Si, Mn, Fe, Mg, Ti, Ca, Al, and Na were determined by ICP-AES. Standards and run conditions are consistent with those of Kelley et al. (2003).

Image analysis was performed using nine screen-captures from the live HD video feed captured by ROV *Hercules* during the dive on Seamount 3. Six images of the overlapping tubular pattern of the deposits were selected from both close-up *Hercules* views and zoomed out *Argus* views. Three images from nearby pillow lava formations were selected at similar scales. The spatial dimensions of all tubular deposits and the pillow lava features were measured using a pixel ruler in Adobe Illustrator. Pairs of major and minor axes measurements for all features observed in the images were plotted on a chart for the purpose of comparing spatial dimensions of hydrothermal deposits to potential sedimented pillow lava.

5. Results

5.1 Mineralogy and morphology of the hydrothermal deposits

X-Ray Diffraction

X-ray diffractograms of sub-samples NA064-64A, NA064-64B, NA064-64C, NA064-65A, NA064-65B, and NA064-65C are presented in Figure 5.1. Analysis reveals an overall diffractogram signature similar to that of several other hydrothermal nontronites (De Carlo et al., 1983; Murnane and Clague, 1983). Both samples and all six subsamples show patterns with little variability between diffractograms. The sub-samples of green nontronite, NA064-64A and NA064-65A, display nearly identical patterns with overall higher intensity peaks. The diffractograms for NA064-64B, NA064-64C, and NA064-65C follow the same pattern as those of NA064-64A and NA064-65A; although NA064-64B has lower intensity peaks. The diffractogram of NA064-65B is considerably different than that of the other five sub-samples. It resembles the general expected nontronite pattern although it shows very weak peaks and more noise; the overall trend fits Fe-oxide patterns. In the sub-samples of the dark black/grey banded material (mostly crustal), NA064-64C and NA064-65C, there is a small but noticeable peak around 12º 2theta (indicated in Figure 5.1). This suggests that in addition to nontronite and Fe-oxide, these sub-samples contain a 7-Å Mn mineral (Murnane and Clague, 1983).

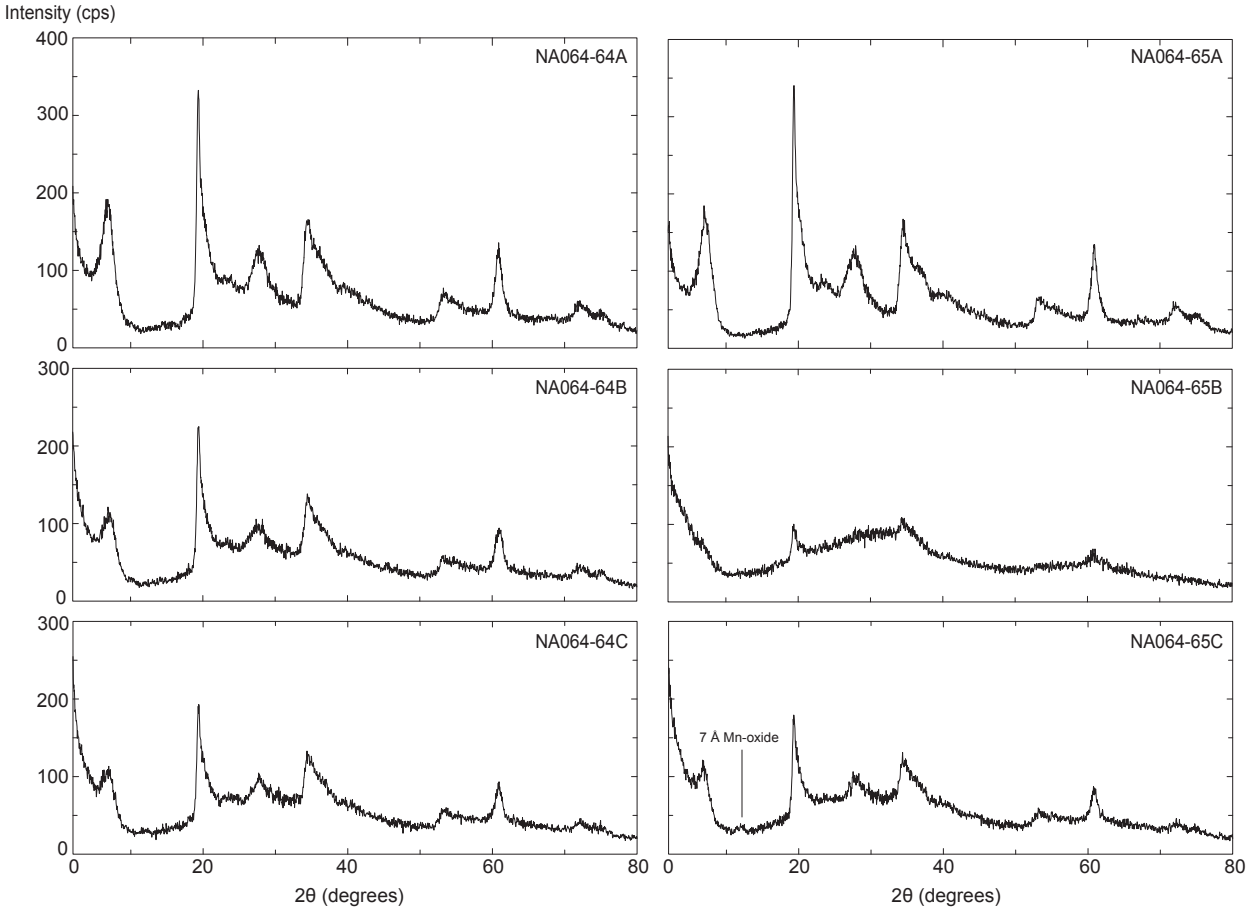

Figure 5.1 X-ray diffractograms of sub-samples NA064-64A, NA064-64B, NA064-64C, NA064-65A, NA064-65B, and NA064-65C. Established nontronite is consistently observed throughout all sub-samples. Small peak at about 12º 2theta in NA064-65C shows a 7-Å Mn-oxide phase. Scans run at 0.8º/minute (0.04º/step and 3 seconds/step).

Scanning Electron Microscopy - Energy-Dispersive X-ray Spectroscopy

SEM-EDS analyses confirmed that grains present in the specimens were high in Fe-oxide (up to nearly 95 wt. % Fe_2O_3 in some regions and an average of over 60 wt. % Fe_2O_3 across all samples) and Si-oxides (up to nearly 50 wt. % SiO_2 in some regions and an average of about 17 wt. % SiO_2 across all samples), which is consistent with the identification of nontronite (De Carlo et al., 1983; Murnane and Clague, 1983; Dekov et al., 2007). Na_2O and P_2O_5 was present in most specimens usually under or about 5 wt. %. Carbon was present in some samples at concentrations up to about 30 wt. % in a few specimens. Trace amounts of MnO, MgO, K_2O, N, and Cl were detected in some specimens. Al2O3, CaO, S, Br, Pd, and Cd were detected at very low concentrations (nearly all well under 2 wt. %) in some specimens. A total of 19 regions on 9 different specimens from all 6 sub-samples (NA064-64A, NA064-64B, NA064-64C, NA064-65A, NA064-65B, and NA064-65C) were analyzed with SEM-EDS. Specimens including "gp" in their label notates that these stubs were coated in gold-palladium while all other stubs were coated in carbon.

The morphological structures of the nontronite and oxides present are consistent across several regions and specimens, although some specimens exhibit notable variability. A general sponge-like basic structure of the nontronite is displayed in a specimen from sub-sample NA064-64A (Figure 5.2). This structure appears to be porous while consisting of many lepispheres (similar to Köhler et al., 1994). Specimen 65A(1) from sub-sample NA064-65A exhibits hollow branching filaments that zigzag and stack or overlap (Figure 5.3, *left*). These tubular filaments of about 2-5 μm in diameter, consist of flat bulbs made up of small overlapping sheets (Figure 5.3, *right*). These structures were most notably observed in specimens from NA064-65A and NA064-65B. EDS analysis of these structures show that they consist of more than 40 wt. % SiO_2, nearly 50 wt. % Fe_2O_3, and contain trace amounts of Na_2O, MgO, and K_2O (2 to 7 wt. % respectively). A different specimen, 65Agp(1) of sample NA064-65A exhibits characteristic nontronite oblate microspheres that are coated in finely layered smectite sheets (Figure 5.4). These structures contain over 24 wt. % SiO_2, nearly 70 wt. % Fe_2O_3, and contain trace amounts of Na_2O, MgO, K_2O, and C (>0.5 wt. % respectively).

Several specimens from sample NA064-64B contain structures that resemble Fe-oxides, nontronite, and associated bacterial structures (Figure 5.5). Similar to the general structure observed in part of NA064-64A (Figure 5.2), NA064-64B also has a spongy basic although more web-like structure (Figure 5.5 A). Specimen 64Bgp(2) includes several regions of stacked Fe-oxide encrusted filaments that are consistent with microbial FeOB (Figure 5.5 B). Among the stacks of these similar segments in specimen 64Bgp(3) are oblate microspheres that propagate off of the filaments (Figure 5.5 C). EDS analysis indicates that the filaments of 64Bgp(2) have about 10 wt. % SiO_2, nearly 74 wt. % Fe_2O_3, almost 8 wt. % P_2O_5, and contain trace amounts of Na_2O, MgO, CaO, Cl, and C. The spheres of 64Bgp(3) have about 11 wt. % SiO_2, nearly 70 wt.

% Fe_2O_3, and over 5 wt. % of Na_2O, P_2O_5, and C (each). More oblate spheres were observed in other specimens of NA064-64B that propagate outward and possibly exhibit surface features that are reminiscent of the honeycomb precipitate morphology of nontronite (Figure 5.5 D). Some of the observed microspheres include a small hole or donut-like central indent (specimen 64B(1), Figure 5.5 E). Tubular filaments with a diameter about 1-2 μm also show hollow features adjacent to more microspheres (Figure 5.5 F). Several more microspheres with central indents are present in specimen 64Bgp(1) that are extremely rich in Fe_2O_3 (almost 95 wt. %) and poor in SiO_2 (0.51 wt. %) (Figure 5.5 G and H). These microspheres also contain almost 3 wt. % MnO, and trace amounts of Al_2O_3, CaO, and C. The sub-sample of NA064-64B consists of banded crustal material from the deposits, thus the high Fe_2O_3 content with relatively high MnO present seems to fit the possibility of a Mn-oxide crust interlayered with Fe-oxide nodules.

Possible bacterial structures identified through SEM imaging with EDS analyses confirming their high levels of carbon may offer insight into formation processes. Several SEM images were captured for various regions where EDS data was not collected. These images also demonstrate similar notable microscopic morphologic features of these deposits.

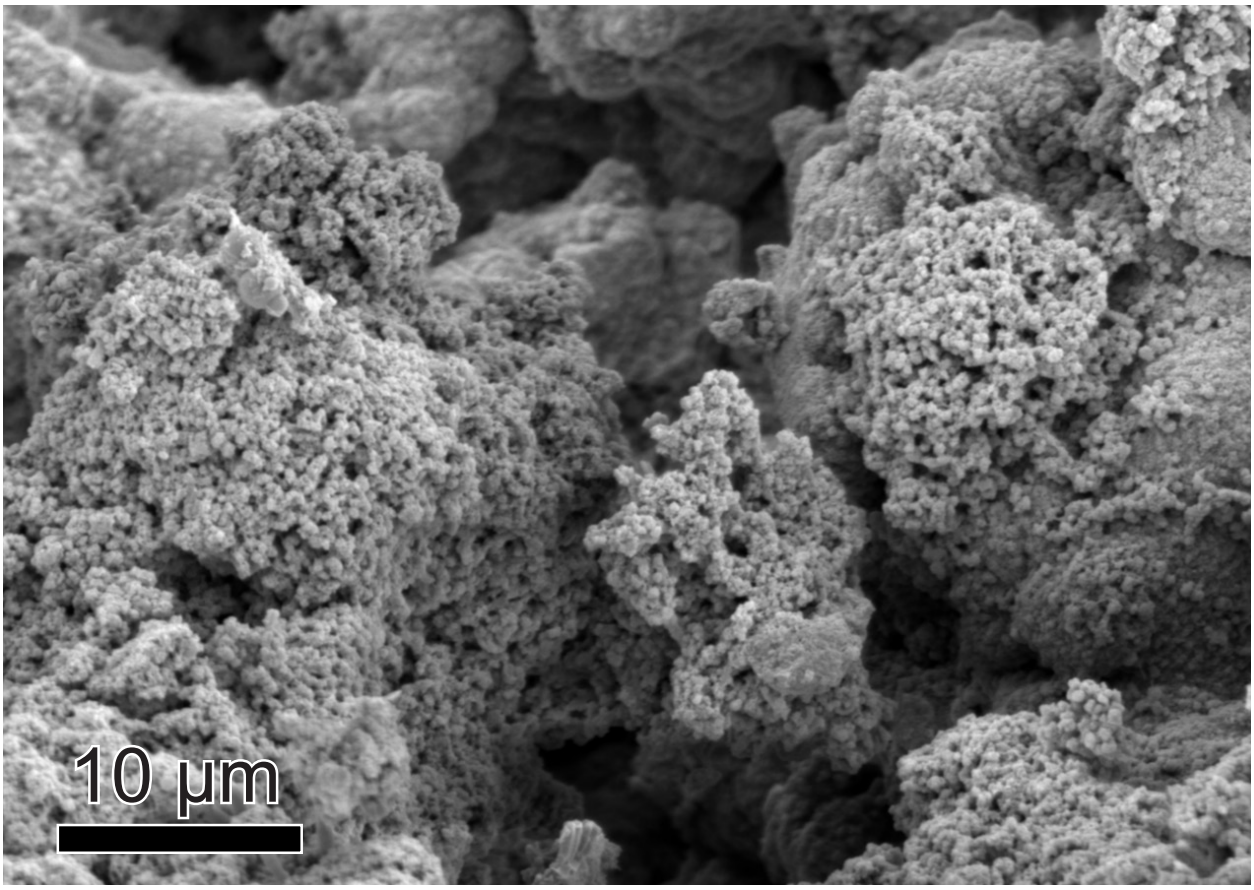

Figure 5.2 Scanning electron micrograph of a specimen from sample NA064-64A showing the sponge-like clay basic structure of the nontronite grains.

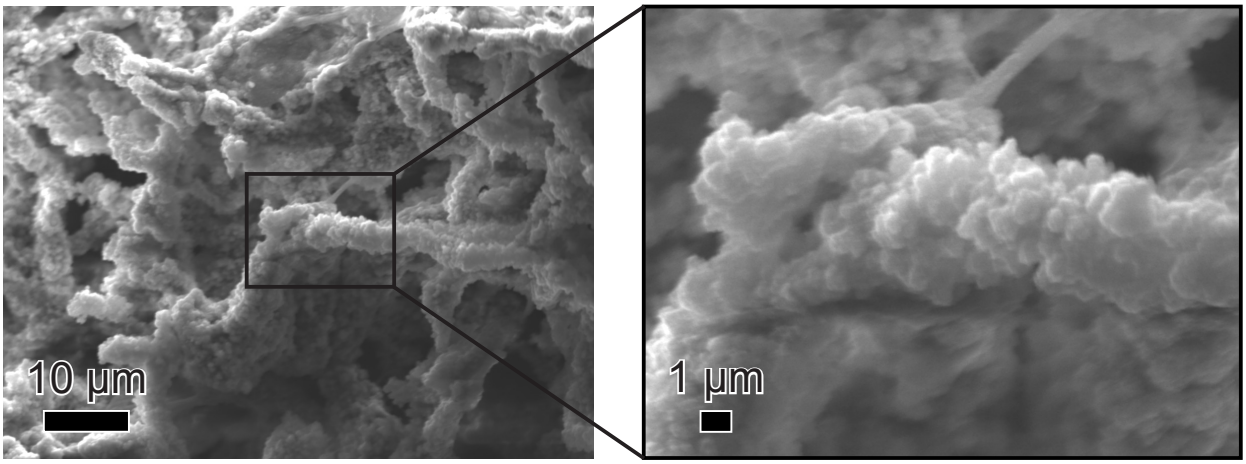

Figure 5.3 Scanning electron micrographs of specimen 65A(1) from sample NA064-65A showing hollow branching filamentous aggregates of nontronite with higher weight percentages of Si-oxides in comparison to Fe-oxides determined from EDS analyses. Branches consist of characteristic fine clay sheets. (EDS analysis of the layers on the filaments).

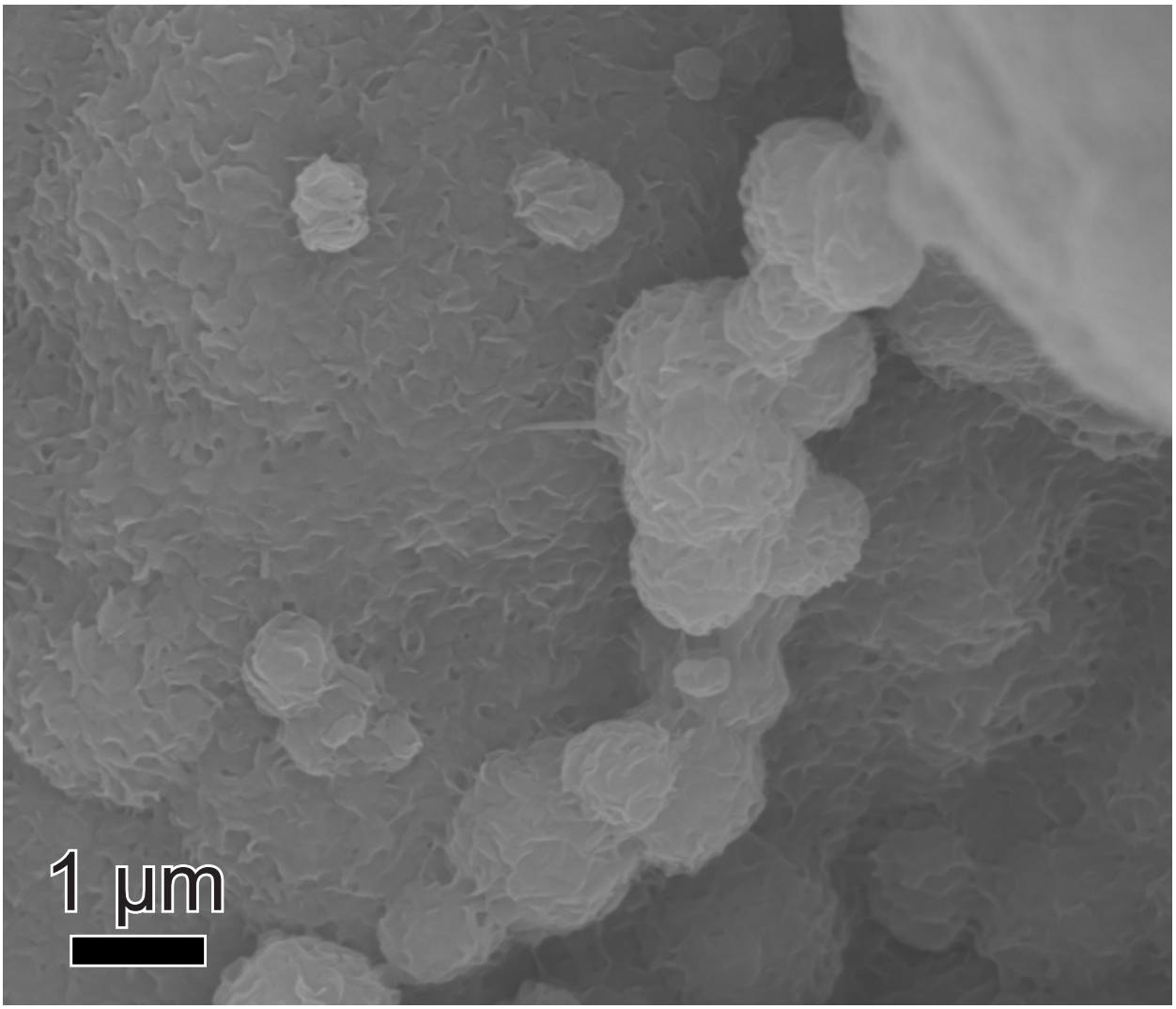

Figure 5.4 Scanning electron micrograph of specimen 65Agp(1) from sample NA064-65A showing oblate microspheres of remnant microbial structures coated in overlapping clay sheets with relatively equal levels of Fe and Si oxides determined from EDS analyses.

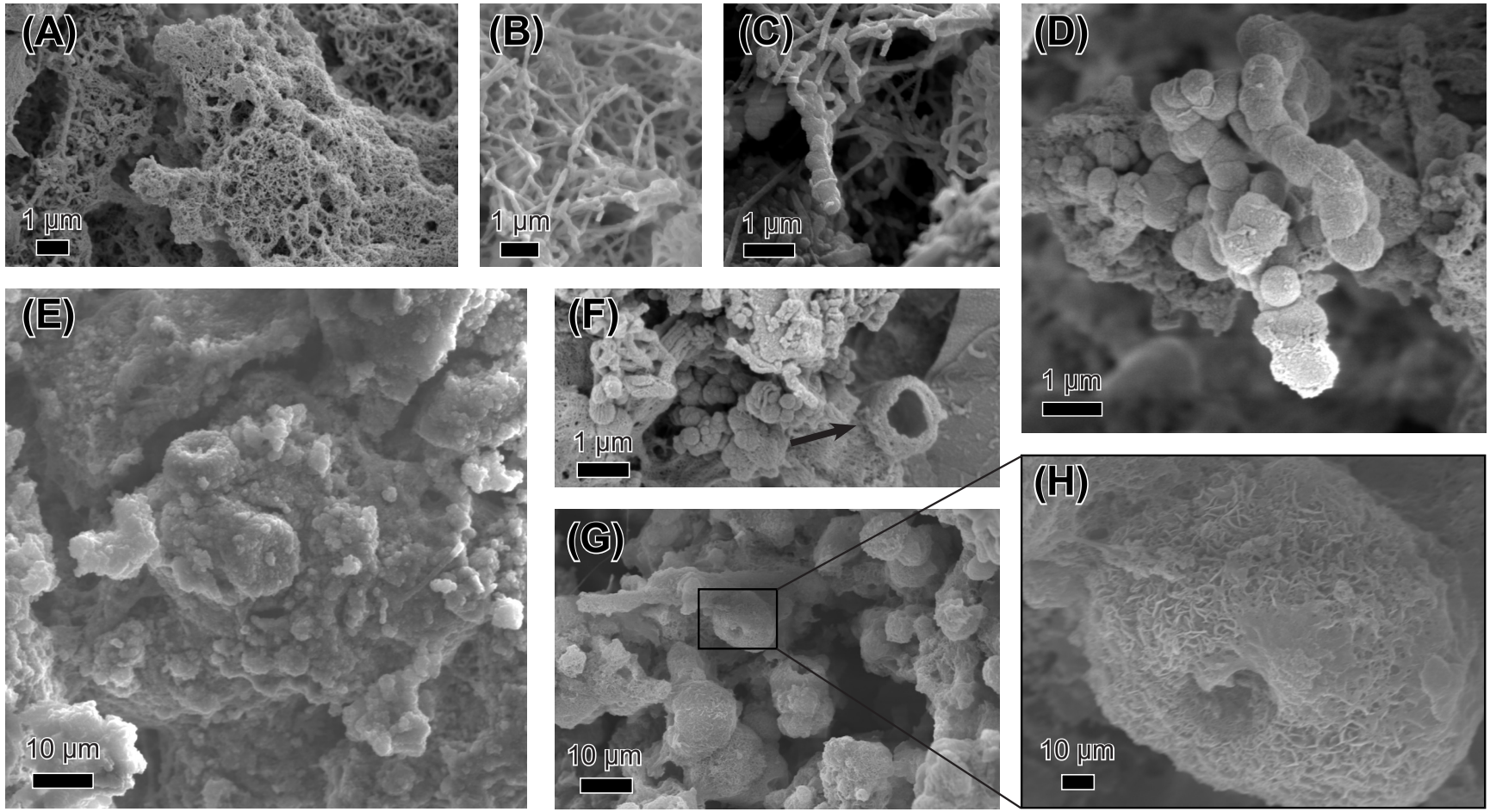

Figure 5.5 Scanning electron micrographs of several specimens from sample NA064-64B. (A) Web-like basic structures of Fe-oxides. (B) Fe-oxide encrusted filamentous microbe-like structures forming overlapping stick-like segments from specimen 64Bgp(2). (C) More Fe-oxide filament structures similar to those in (B), with propagating oblate microspheres stemming off of the filaments. EDS analysis indicated that the spheres have less Fe-oxide and more Si-oxide present in comparison to its skinnier filamentous counterpart observed in (B). (D) Clusters of oblate microspheres increasing in size from the outer edges of the image to the center. Surface of spheres may exhibit reminiscent honeycomb-like precipitates. (E) Image of specimen 64B(1) of prominent microspheres with defined central hole likely previously occupied by bacterial structures. EDS indicates Fe-oxide rich microspheres. (F) Arrow points toward broken hollow filamentous aggregate. (G,H) From specimen 64Bgp(1), a close-up view of a hollow microspheres that are very rich in Fe-oxide (Fe_2O_3), nearly 95 wt. %, indicated through EDS analysis.

5.2 Chemistry of the hydrothermal deposits

Major element composition

The major element chemical data for all six sub-samples and the two bulk samples (NA064-64A, NA064-64B, NA064-64C, NA064-64D, NA064-65A, NA064-65B, NA064-65C, and NA064-65D) along with data from samples of 15 comparable studies and locales are presented in Tables 5.1 and 1.1, respectively. The chemistry across all 8 sub-samples from the present study is consistent with that of nontronite and Fe-oxides. Overall, the deposits contain 38-51 wt. % of SiO_2 and 40-50 wt. % of Fe_2O_3. Sub-samples NA064-64A and NA064-65A are the most SiO_2-rich and the least Fe_2O_3-rich while NA064-65B is the least SiO_2-rich and the most Fe_2O_3-rich. MnO is most abundant in the crustal banded sub-samples (NA064-64C and NA064-65C) and the bulk samples (NA064-64D and NA064-65D) which is likely consistent with the possible presence of a Mn-oxide phase as observed in the XRD data. MgO and Na_2O are present in all sub-samples in trace amounts, 1.5-2.5 wt. % each. In previous studies, nontronite typically contains about 40-55 wt. % of SiO_2 and 28-34 wt. % of Fe_2O_3 (Table 1.1).

While the samples of the present study are overall more rich in Fe-oxide compared to most other studies (Figure 5.6; Table 1.1; Table 5.2), the two nontronite sub-samples (which are not strictly nontronite and likely still contain some Fe-oxide) are geochemically much more similar to previous nontronite values having higher concentrations of MgO (Figure 5.6) in comparison to hydrothermal deposits of Fe-oxide alone.

Table 5.1 Geochemical data for major elements of all six sub-samples and the two bulk samples. All values presented in wt. %. NA064-64A, NA064-64B, NA064-65B, and NA064-65D have totals normalized to 100.

Reference	Seamount 3, Galapagos Present Study							
Sample #	NA064-64A	NA064-64B	NA064-64C	NA064-64D	NA064-65A	NA064-65B	NA064-65C	NA064-65D
SiO_2	48.81	42.55	44.69	41.13	52.40	40.12	44.64	42.68
Al_2O_3	0.25	0.28	0.20	0.22	0.05	0.09	0.10	0.08
Fe_2O_3	43.82	49.51	46.42	48.77	40.57	51.66	46.41	48.29
FeO	-	-	-	-	-	-	-	-
MnO	0.16	0.14	1.03	1.05	0.01	0.05	0.80	0.82
MgO	2.36	1.95	2.26	2.02	2.40	1.71	2.28	2.08
CaO	0.54	0.89	0.90	1.03	0.30	1.00	0.88	1.04
Na_2O	2.06	1.73	2.31	2.37	2.11	2.11	2.54	2.28
K_2O	1.31	1.11	1.05	1.09	1.84	1.28	1.41	1.34
P_2O_5	0.67	1.81	1.17	1.35	0.26	1.96	1.10	1.38
TiO_2	0.01	0.01	0.01	0.02	0.00	0.00	0.01	0.00
LOI	7.84	9.97	9.04	9.47	6.49	9.12	8.60	8.45
H_2O	4.68	9.08	7.39	5.00	8.42	10.72	7.92	8.76
Total	100.00	100.00	100.05	99.04	99.94	100.00	100.17	100.00

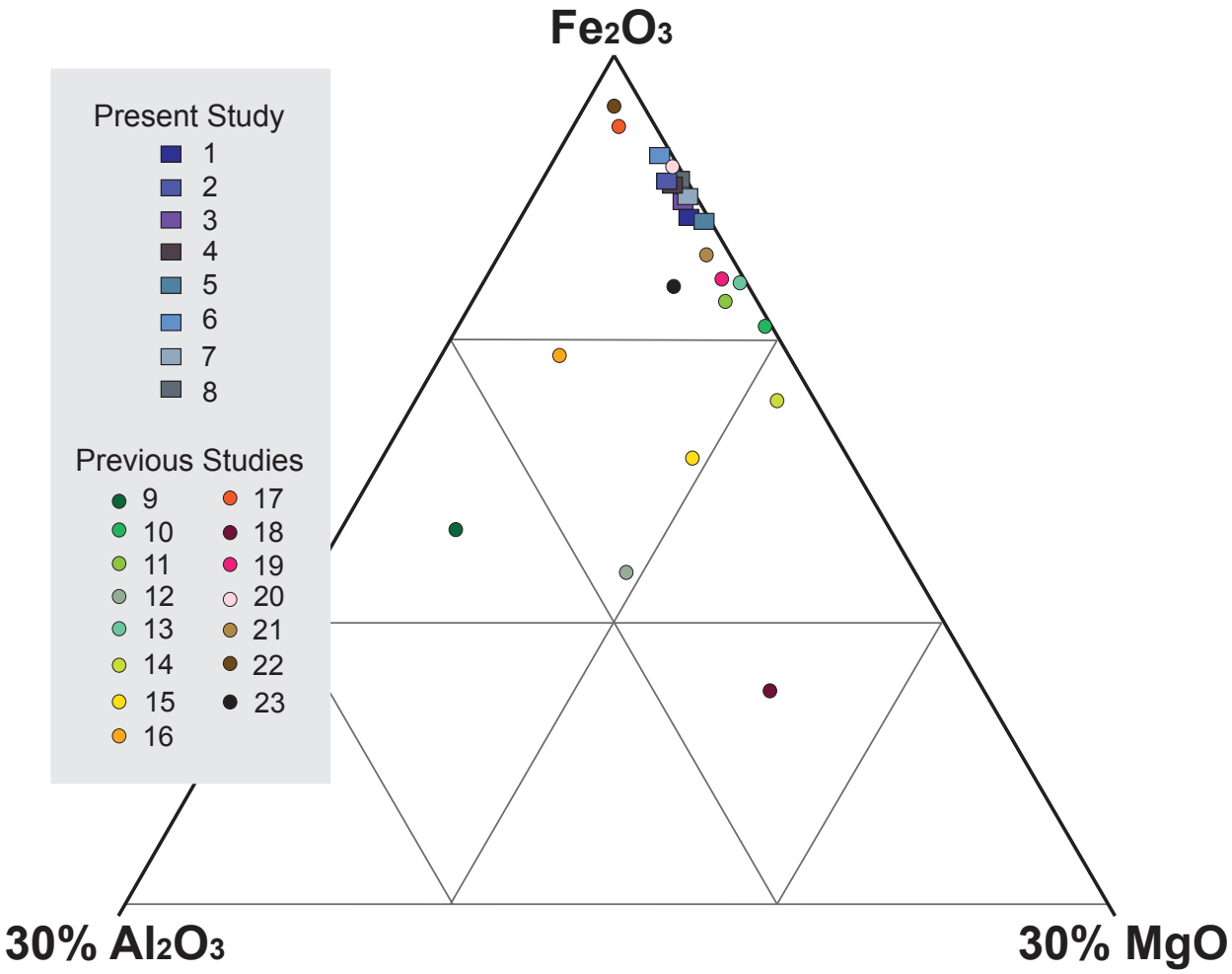

Figure 5.6 Fe_2O_3 – MgO – Al_2O_3 ternary diagram of 23 samples, 15 from previous comparable studies and 8 from the present study are plotted as wt. %. See Table 5.2 for the references to each diagram number.

Table 5.2 Corresponding 15 comparable studies and 8 sub-samples from present study, each with their respective ternary diagram number.

Ternary Diagram #	Sample Name	Source	Location
1	NA064-64A	Present Study	Seamount 3
2	NA064-64B		
3	NA064-64C		
4	NA064-64D		
5	NA064-65A		
6	NA064-65B		
7	NA064-65C		
8	NA064-65D		
9	T/77-29 (113-115)	Dekov et al. (2007)	Eolo Seamount
10	1183-14/15	Alt et al. (1987)	Red Seamount
11	TT152-11G	Murnane and Clague (1983)	Juan de Fuca Ridge
12	20-2G	De Carlo et al. (1983)	Loihi Seamount
13	N2	Corliss et al. (1978)	Galapagos Rift
14	DSDP Leg 54, bulk	Hékinian et al. (1978)	Galapagos Mounds
15	69-11-2	Grill et al. (1981)	Explorer Ridge
16	average	Bischoff (1972)	Red Sea
17	10094 252-260	Cole (1988)	Red Sea
18	average	Dymond and Eklund (1978)	Bauer Basin
19	average	Hoffert et al. (1978)	FAMOUS
20	RS 1	Dill et al. (1994)	EPR 18ºS
21	SO 35 KD80	Stoffers et al. (1990)	Lau Basin
22	2901-2	Severmann et al. (2004)	TAG
23	S-8b	McMurtry et al. (1993)	Kasuga 3 Seamount

Trace and rare earth element composition

The trace and rare earth element chemistry for all six sub-samples and the two bulk samples (NA064-64A, NA064-64B, NA064-64C, NA064-64D, NA064-65A, NA064-65B, NA064-65C, and NA064-65D) are presented in Table 5.3. Trace and REE chemical data from samples of 10 comparable studies and locales are presented in Table 1.2.

The 8 sub-samples from the present study contain very similar trace and REE chemistry trends (Figure 5.7). The differences in intensity or quantity of various elements among the 8 sub-samples are to be expected since they were separated based on appearance and apparent composition, while they share similar Fe-oxide and nontronite trends overall. Ba, Li, Ni, La, Rb, Sr, V, Y, Zn, and Zr are the most abundant trace and rare earth elements. Although these ten elements varied as well among samples from previous studies, they were also the most prominent among the trace and REE.

The REE distribution patterns for the present study show negative Ce and Eu anomalies. The bulk samples (NA064-64D and NA064-65D, shown as orange) are both more enriched overall than the 6 sub-samples. The sub-samples for NA064-65 (NA064-65A, NA064-65B, NA064-65C) are least enriched in REE with the green nontronite sub-sample (NA064-65A) being the least of all sub-samples. The sub-samples for NA064-64 (NA064-64A, NA064-64B, NA064-64C) are significantly more enriched and similar overall compared to those of 65. These trends are similar to those of the Lilliput hydrothermal deposits (Dekov et al., 2010). These patterns also follow typical REE distribution patterns for deep seawater (Douville et al., 1999; Dekov et al., 2010).

Table 5.3 Geochemical data for trace and REE of all six sub-samples (64A, 64B, 64C, 65A, 65B, and 65C) and the two bulk samples (64D and 65D). All values presented in ppm.

Reference	Seamount 3, Galapagos							
	Present Study							
Sample #	NA064-64A	NA064-64B	NA064-64C	NA064-64D	NA064-65A	NA064-65B	NA064-65C	NA064-65D
Ag	-	-	-	-	-	-	-	-
As	37.74	60.45	48.73	62.20	8.06	37.93	45.24	60.14
Ba	101.97	89.94	119.77	118.77	6.77	29.63	90.64	67.28
Be	0.05	0.02	0.04	0.05	-	-	0.05	0.07
Bi	-	-	-	-	-	-	-	-
Cd	-	-	-	-	-	-	-	-
Co	0.66	0.58	1.54	1.75	0.08	0.08	1.10	1.93
Cr	3.17	3.32	2.74	3.90	-	0.05	3.76	3.95
Cs	0.55	0.43	0.39	0.56	1.10	0.60	0.61	0.81
Cu	2.61	3.57	3.78	3.69	0.28	0.54	5.24	7.34
Ga	0.41	0.16	0.32	0.25	0.02	0.03	0.15	0.19
Ge	-	-	-	-	-	-	-	-
Hf	0.06	0.03	0.04	0.06	0.01	0.01	0.06	0.05
In	-	-	-	-	-	-	-	-
Li	2.40	2.12	9.06	9.50	1.34	1.78	7.35	7.87
Mo	-	-	-	-	-	-	-	-
Nb	0.14	0.09	0.13	0.15	0.00	0.01	0.10	0.13
Ni	4.16	2.56	15.08	15.50	0.76	0.89	14.14	34.44
La	-	-	-	-	-	-	-	-
Ce	1.14	1.34	1.12	1.17	0.48	0.75	0.44	0.90
Pr	0.32	0.39	0.34	0.34	0.14	0.22	0.18	0.33
Nd	1.49	1.78	1.55	1.58	0.65	1.05	0.82	1.54
Sm	0.28	0.33	0.29	0.29	0.11	0.17	0.16	0.29
Eu	0.09	0.10	0.09	0.10	0.03	0.05	0.05	0.09
Gd	0.47	0.51	0.48	0.53	0.20	0.30	0.28	0.50
Tb	0.07	0.08	0.08	0.08	0.03	0.04	0.05	0.08
Dy	0.55	0.59	0.55	0.63	0.21	0.34	0.37	0.60
Ho	0.16	0.16	0.15	0.19	0.06	0.10	0.11	0.17
Er	0.51	0.52	0.49	0.62	0.19	0.34	0.36	0.57
Tm	-	-	-	-	-	-	-	-
Yb	0.52	0.51	0.49	0.63	0.17	0.32	0.39	0.60
Lu	0.09	0.09	0.08	0.11	0.03	0.06	0.07	0.11
Pb	0.40	0.44	0.50	0.50	0.03	0.21	0.44	1.10
Rb	20.25	16.11	15.37	18.34	33.04	19.53	19.34	20.57
Sb	0.86	1.26	1.53	1.75	0.38	0.93	1.40	2.42
Sc	0.43	0.27	0.82	0.64	0.01	0.03	1.15	0.34
Se	0.03	0.03	0.06	0.06	0.01	0.02	0.06	0.08
Sn	-	-	-	-	-	-	-	-
Sr	128.35	223.71	213.96	265.06	69.47	271.84	237.02	268.88
Ta	0.00	0.00	0.00	0.01	-	-	0.00	0.00
Th	0.03	0.02	0.02	0.02	0.01	0.00	0.03	0.02
Tl	-	-	-	-	-	-	-	-
U	0.33	0.21	0.63	1.03	0.25	0.19	0.73	1.33
V	42.24	22.30	58.92	74.71	3.24	3.57	68.72	103.82
W	-	-	-	-	-	-	-	-
Y	8.17	8.11	7.20	10.59	3.43	6.80	6.61	9.06
Zn	29.45	22.62	39.73	45.24	15.29	12.09	33.40	62.52
Zr	3.68	2.08	3.24	3.75	0.30	0.34	4.04	4.71

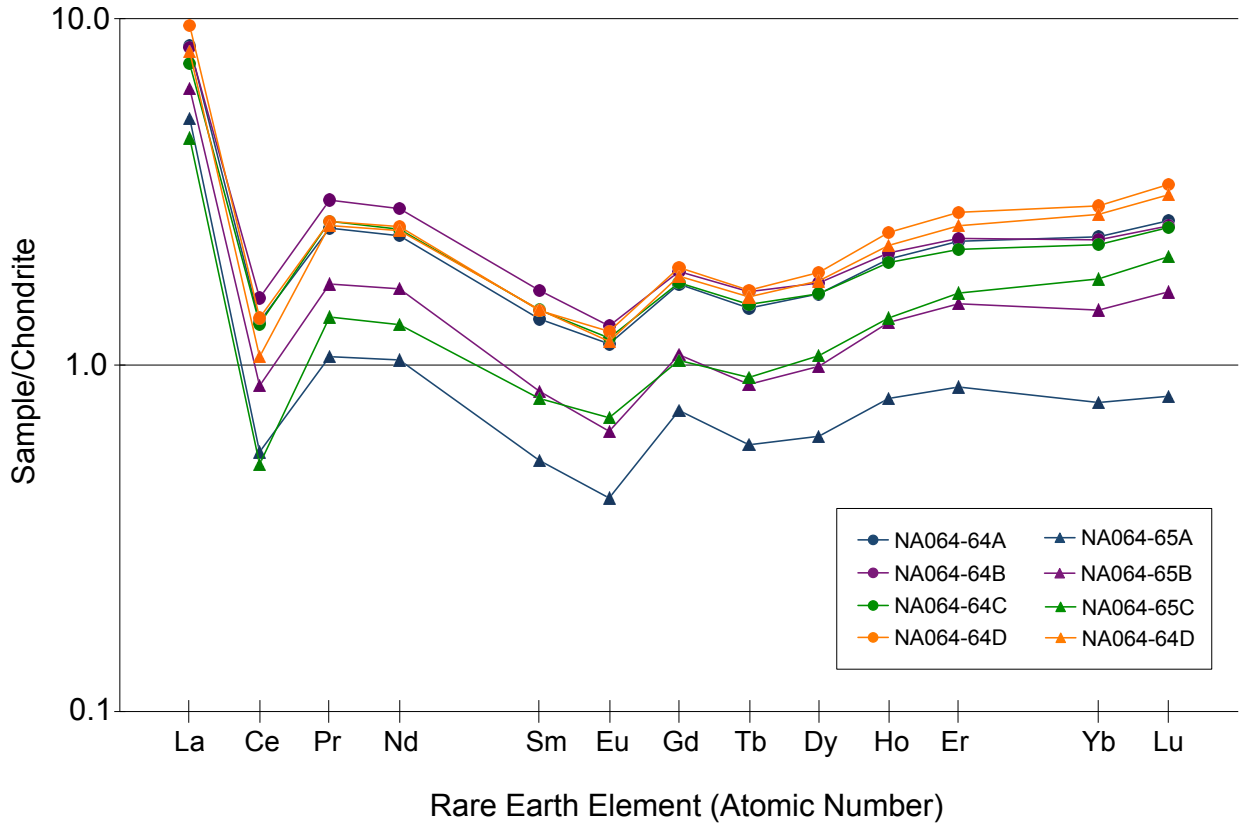

Figure 5.7 CI chondrite-normalized (Sun and McDonough, 1989) REE distribution patterns for all six sub-samples (64A, 64B, 64C, 65A, 65B, and 65C) and the two bulk samples (64D and 65D). General trend is comparable to that of seawater (Douville et al., 1999; Dekov et al., 2010).

6. Discussion

6.1 Mineralogy and chemistry of the deposits

X-ray diffraction patterns of samples from Seamount 3 of the Wolf-Darwin Seamount Chain confirm the presence of nontronite specifically in NA064-64A and NA064-65A and the diffractogram tracings of NA064-65B are characteristic of Fe-oxides and some nontronite. These deposits are similar in their mineralogical and chemical composition to those of previous studies from other oceanic seamounts (Corliss et al., 1978; Hékinian et al., 1978; Grill et al., 1981; De Carlo et al., 1983; Murnane and Clague, 1983; Alt et al., 1987; Dekov et al., 2007). Overall, the chemical consistency between the samples from the present study and those from other studies suggest that the setting is hydrothermal in origin and the formation of both nontronite and Fe-oxides are from low-temperature diffuse venting processes. Although no oxygen isotopic analyses were performed on the samples of this study, the presence of nontronite indicates formation temperatures between 20º C and 80º C based on similar past studies (De Carlo et al, 1983; McMurtry et al., 1983; Murnane and Clague, 1983; Alt et al., 1987; Stoffers et al., 1990; McMurtry et al., 1993; Köhler et al., 1994; Severmann et al., 2004; Dekov et al., 2007).

Nontronite compositions published in previous studies had about 46-57 wt.% SiO_2 and about 25-34 wt.% of Fe_2O_3 (Corliss et al., 1978; Hékinian et al., 1978; Grill et al., 1981; De Carlo et al., 1983; Murnane and Clague, 1983; Alt et al., 1987; Dekov et al., 2007). In general the nontronite compositions from Seamount 3 are lower in SiO_2 and higher in Fe_2O_3. Higher Fe/Si ratios have been suggested as indicators of temperatures on the higher side of the formation range (20º-80º C; Murnane and Clague, 1983). Although analyzed with bulk samples and not pure nontronite, the average Fe/Si ratios of samples in this study do appear to be higher than those observed in other studies (De Carlo et al., 1983; Murnane and Clague, 1983; Alt et al., 1987; Stoffers et al., 1990; McMurtry et al., 1993; Severmann et al., 2004; Dekov et al., 2007). This may suggest that the formation temperature was on the higher end, closer to 40-80ºC rather than the low end of 20-40ºC that was observed in some studies (Stoffers et al., 1990; McMurtry et al., 1993).

A negative Ce anomaly was observed in the REE data (Figure 5.7), which is indicative of hydrothermal origins (Hékinian et al., 1993). As the hydrothermal fluids mix with the seawater, mineral grains are precipitated out and this oxidative process results in negative Ce anomalies (Bao et al., 2008). Ce, a valence-variable element, is often isotopically fractionated more easily

from seawater under such oxidative conditions (Koeppenkastrop and De Carlo, 1992; Bao et al., 2008). Likewise, the negative Eu anomaly suggests hydrothermal fluids of low temperatures (<100ºC) in comparison to high-temperature systems with channelized flow (Hékinian et al., 1993; Dekov et al., 2007).

6.2 Origin of the nontronite and Fe-oxide deposits

Several hypotheses for seafloor nontronite formation have been presented in previous studies. Most have described the processes as hydrothermal in origin, although some non-hydrothermal hypotheses have been presented (Cole and Shaw, 1983; Dekov et al., 2007). The relationship between Fe-oxide and nontronite formation is central in some models. The models that will be discussed below include: (1) replacement (non-hydrothermal), (2) alteration (non-hydrothermal), (3) direct precipitation of Fe-oxides and nontronite from hydrothermal fluids, (4) direct precipitation of Fe-oxides from hydrothermal fluids with nontronite forming through aging processes, (5) microbially mediated precipitation of Fe-oxides and nontronite fueled by hydrothermal fluids, and (6) microbially mediated precipitation of Fe-oxides fueled by hydrothermal fluids with nontronite forming through aging processes. The two non-hydrothermal models (1 and 2) presented are not likely relevant to the formation of the Seamount 3 deposits for several reasons. As for the hydrothermal models (3, 4, 5, and 6), there is evidence that all may describe the origins and formation of the deposits from Seamount 3. It is possible that a combination of processes best accounts for the precipitation of these deposits.

6.2.1 Non-hydrothermal formation models

Dekov et al. (2007) outlined a possible ‘replacement’ hypothesis (model 1) which involves the replacement of silica-rich minerals within local sediments for the Fe-Si based smectite, nontronite. This was deemed unlikely by Dekov et al. (2007) for nontronite from the Eolo seamount because their samples were mostly monomineralic and lacked a combination of expected admixed detrital material. Cole and Shaw (1983) described three possible methods of formation, one of which is similar to the replacement process in that it involves the alteration of local volcanic rocks and glasses (not-hydrothermal; model 2).

Both of these non-hydrothermal processes are unlikely for Seamount 3 nontronite

formation. There are several reasons for suggesting that the deposits from this study are hydrothermal in origin. Some diagnostic characteristics of hydrothermally-originated deposits were outlined by Köhler et al. (1994), including: purity and monomineralic qualities, low Al content, low content of accessory minor elements, and warm formation temperatures (low-temperature, but warm in comparison to ambient seawater and non-hydrothermal processes). In addition to these, REE distribution trends that follow seawater trends and low-temperature anomalies (the Ce and Eu negative anomalies) also apply as a diagnostic tool for low-temperature diffuse hydrothermal venting. The unusual configuration of the Seamount 3 deposits is likely a product of pattern-controlled hydrothermal fluid flow. It would be highly unlikely for non-hydrothermal mineral precipitation, such as the replacement or alteration processes, to occur in such a distinct and unusual pattern. Although pillows below the surface could be weathered and replaced at their contacts, we would expect to see this on and around the pillows. For a pattern to form above them, there would need to be fluid flow upwelling and forcing the replacement and precipitation to occur on the surface rather than just at the pillow sites below.

6.2.2 Hydrothermal formation models

There are several possible hydrothermal precipitation mechanisms (models 3, 4, 5, and 6) to explain the nontronite and Fe-oxyhydroxide deposits on Seamount 3. The precipitation of nontronite and Fe-oxyhydroxides may be biologically-mediated from hydrothermal fluids or abiogenic (directly deposited from hydrothermal fluids). As described in Dekov et al (2010), there are three modes of Fe-Si-oxyhydroxide precipitation: microbially-mediated, abiogenic (including microbes within the precipitate matrix but not facilitating precipitation), or a combination of the two.

In abiogenic processes direct precipitation from hydrothermal fluids (models 3 and 4) is possible (De Carlo et al., 1983; Murnane and Clague, 1983; Dekov et al., 2010) and suggested as a possibility by most hydrothermal nontronite and Fe-oxide studies. Direct precipitation would occur under specific oxidation-reduction conditions (Harder, 1976, 1978). This model involves the oxidation of cooler distal hydrothermal fluids at the seafloor, followed by the precipitation of Fe and Mn oxides, and eventually nontronite through a few different possible processes. First, high-temperature hydrothermal fluids (>350º C) at depth (3-5 km) interact with the local rock and mix with seawater continuously as it flows through the porous crust (Murnane and Clague, 1983; Alt, 1988). This hot acidic and reducing fluid (that formed at depth) upwells toward the seafloor and further reacts with cooler shallower seawater, rocks, and minerals. It is possible that sulfide precipitation occurs below the surface but higher up from the original fluid formation, where the fluids are still much warmer than they become at the surface (Murnane and Clague, 1983; Alt, 1988). Once these fluids approach the seafloor, they are much cooler after significant

interaction with seawater. Although the amount of mixing and rate of mixing may affect the composition of the fluid, typically it will be rich in Si, Fe, and Mn (Edmond et al., 1979; Alt, 1988). At the surface, exposure to seawater mixing and thus oxidizing conditions results in the oxidation of Fe^{2+} to Fe^{3+} and this reaction drives the precipitation of the dissolved ferrous iron into Fe-oxyhydroxides (Rozenson and Heller-Kallai, 1976; Murnane and Clague, 1983). It is possible that a sediment layer, such as that observed at Seamount 3, may also offer a redox buffer (Murnane and Clague, 1983). The oxidized iron (Fe^{3+}) may be broken down through hydrolysis and then precipitated again to form poorly ordered Fe-oxyhydroxides (Dekov et al., 2010).

Since iron oxidizes more readily that Mn (Stumm and Morgan, 1981; Alt, 1988), a layered appearance is often observed with Fe-oxides closer to the active venting and Mn further away as a crust or just dispersed in the water column (although eventually through aging a Mn-oxide crust will likely form). Such a gradation was observed at the hydrothermal field at Seamount 3. Sub-sampling was based on those gradations and apparent divides into Mn-oxide, Fe-Si-oxide, and nontronite. As reduced iron interacts with oxidized Mn, a redox reaction may occur. Reduced iron (Fe^{2+}) upwelled with the hydrothermal fluids may be oxidized at the surface as it reacts with the base of the Mn-oxide crust; this will cause a reduction of Mn^{4+} to Mn^{2+} (Honnorez et al., 1981). Then the Mn^{2+} (reduced Mn) may be remobilized and re-oxidized as it interacts with surrounding oxygenated seawater, thus forming another Mn-oxide outer crust atop the existing Mn-oxide crust (Honnorez et al., 1981).

It has been hypothesized, that amorphous Fe-Si-oxyhydroxides may form nontronite or Fe-phyllosilicate smectite (Köhler et al., 1994; Kloprogge et al., 1999; Dekov et al., 2007). These Fe-Si-oxyhydroxides can be source material for nontronite formation through aging processes (model 4) of the deposits where the nontronite is not directly hydrothermal in origin (Dekov et al., 2007).

For nontronite to form by abiogenic precipitation (model 3), the presence of reduced iron (Fe^{2+}) in the upwelling hydrothermal fluids is essential, as Harder (1978) described, because it helps stabilize and control the formation of the nontronite octahedral layer. This is necessary for the orientation of SiO_4 tetrahedra required to form a smectite (or even just general clay mineral) lattice (Dekov et al., 2007). The Eh must also remain below zero in order to maintain some ferrous iron for nontronite formation and avoid oxidizing all of the Fe^{2+} and the precipitation of ferrihydrite instead of nontronite (Jambor and Dutrizac, 1998). The general temperature conditions are also very specific for seafloor hydrothermal nontronite formation. Nontronite typically will not form outside of the temperature range of 15 to 96º C (Dekov et al., 2007). At higher temperatures (occurring at high-temperature channelized vents), Fe-oxyhydroxides will typically form instead (De Carlo et al., 1983). These conditions all describe a hydrothermal origin and possibly one that is abiogenic. More information is required to determine whether the precipitation of the oxides and smectite are biologically mediated.

Alt (1988) described how ratios of Fe to H_2S and silica contents may play a major role in determining whether Fe-oxides, and later nontronite, will form. If Fe/H_2S is less than 1 (i.e. more H_2S than Fe in solution) then Fe will precipitate out early, before reaching the surface. Under these conditions, it is believed that sulfides (H_2S) will form subsurface. This will leave the remaining upwelling hydrothermal fluids Mn-rich and thus primarily form Mn-oxide deposits on the seafloor (Murnane and Clague, 1983; Alt, 1988). Whereas if Fe/H_2S is more than 1 (solution very rich in Fe) then there will still be some Fe in hydrothermal fluids upwelled to the surface (post sulfide formation) and so the necessary ingredients for Fe-oxide deposits are available for their formation on the seafloor. From this, it may be concluded that the Fe/H_2S ratio for hydrothermal fluids at Seamount 3 is greater than 1 due to the presence of Fe-oxides in the deposits. These studies and conditions describe potential settings for direct hydrothermal or hydrothermal-biogenic Fe-oxide precipitation (a possible precursor to nontronite).

There are several possible biogenic models for hydrothermal nontronite and associated Fe-oxide formation that also occur across a strong oxidation gradient (model 5 and 6). These models have been described from samples taken in situ and through experimental work. Fe-oxidizing bacteria has been understood to play a large role in the precipitation of Fe-oxyhydroxides at hydrothermal vents (Emerson and Moyer, 2002; Emerson et al., 2010).

In the present study (and in Alt, 1988), any efforts to identify the bacteria species associated with Fe-oxide and nontronite formation would be tentative at best. Sampling protocols were not implemented for the identification of bacteria during the exploration of Seamount 3. In order to properly identify such microbial structures, strains would need to be cultured. While the ROV ascended up the water column above Seamount 3, most of the fluffy yellow bacterial mat material winnowed off of the samples as they were in an open rock box. Not only were the bacterial mats not sampled with the intent of culturing and identifying, but samples were stored in bags and crates for a few months before any analyses were conducted. Any possible remaining bacteria would not have been in a condition for proper analysis. Thus, these hypotheses are highly speculative for the present study.

For a biogenic formation to be possible evidence of microbes or FeOB should be present in SEM micrographs or in ROV imagery there should be clear indications of bacterial mats on the surface which are common environments for FeOB. Spherical and web-like microstructures were observed in SEM micrographs from specimens of Seamount 3 samples and in several other deposits (Köhler et al., 1994; Ueshima and Tazaki, 2001; Dekov et al., 2010; Li et al., 2012). This general morphology is believed to be controlled by microbes (living in mats on the seafloor exposed to oxygenated water) that oxidize iron and thus are linked to the deposition of Fe^{3+}. The observed microstructures (even without direct observations of bacteria itself) and morphology of these deposits and many others are strikingly similar to the structures of FeOB. If such bacteria become encrusted in Fe-oxide or nontronite, then the morphology of these oxides and clays will

be controlled by the structure of the bacteria.

Alt (1988) described twisted ribbons, filaments, and general structures that resemble FeOB within the hydrothermal material (sample 1643-1) from Red Seamount (East Pacific Rise). These structures tended to be coated in Fe-oxyhydroxides suggesting that FeOB may be contributing to the formation of this active deposit on Red Seamount. Alt (1988) also observed a color zonation or layering (within the Fe-oxide samples from Red Seamount) similar to that of the present study. With evidence of such twisted ribbons, he concluded that bacteria likely helped actively precipitate Fe from hydrothermal fluids. The morphology observed of the apparent bacterial structures and their encrustation of Fe-oxide is indicative of such bacteria playing an active role in oxide and possibly nontronite formation (model 5) (Buchanan and Gibbons, 1974). However, some studies suggest that nontronite formation may occur after biologically facilitated (or abiogenic, direct hydrothermal, precipitation as discussed in model 4) precipitation of Fe-oxides or oxidation of Fe (model 6). Biogenic, in the same way that abiogenic, poorly-ordered Fe-Si-oxyhydroxides can be source material for nontronite formation through aging processes of the deposits where the nontronite is not directly hydrothermal in origin (Dekov et al., 2007). Therefore, this particular model (model 6) suggests that nontronite would not directly be biogenic in its formation but rather transitively through the precursor biogenic Fe-Si-oxyhydroxides.

Alternatively, Ueshima and Tazaki (2001) presented an experimental model for biogenic nontronite formation through microbial polysaccharides, fitting into model 5. In the deposits studied by Ueshima and Tazaki (2001), it was observed that specific bacteria are able to secrete extracellular polymer substrates (EPS) in order to protect from the severe environmental conditions that surround them. This EPS acts as a biofilm and a reactive geochemical surface. Ueshima and Tazaki (2001) determined that nontronite formation occurs within the EPS on top of bacterial cells while Fe-oxyhydroxides actually form outside of the EPS. Although they investigated this phenomena on polysaccharide EPS, EPS can consist of lipids, proteins, and other types of organic compounds (Fortin et al., 1997; Ueshima and Tazaki, 2001). For nontronite to form, time is required as precipitation is slow. There must be this framework available for the nontronite formation, such as that provided by EPS where a ‘template’ is offered to orient the required tetrahedra silicate sheet (polysaccharide, for example) onto the polymers of the EPS (Ueshima and Tazaki, 2001).

Bacterial growth is favored toward the outer part of the deposits, where contact with oxygenated seawater can be maintained. They will migrate outwards as deposits grow. The gradient will continue as nontronite forms, reducing conditions will remain closest to the hydrothermal fluids and oxidizing conditions will remain more distally near the bacteria on the crust. This would correspond to a gradient within the tubular deposits (Figure 2.3). This would also be an explanation for the strong color gradation that was observed in this study. Soft yellow

Fe-oxide mats observed in situ from ROV imagery offer evidence that bacteria may be present and assisting in the precipitation of such deposits (support for models 5 and 6). Wherever there is a source of reduced Fe, oxygen, and nutrients, FeOB will likely be present (Emerson et al., 2010). The SEM micrographs from the present study reveal structures that are similar to the morphology of other documented bacterial structures (Köhler et al., 1994; Ueshima and Tazaki, 2001; Dekov et al., 2007; Dekov et al., 2010; Li et al., 2012; among several others). The structures of the present study are particularly similar to the globular aggregates, oblate microspheres, and filamentous structures of the hydrothermal precipitates in Li et al. (2012) as well as the thread-like bacterial structures encrusted in Fe-sulfides from Dekov et al. (2010). The microspheres from the present study appear to have a central hole where an abandoned bacterium likely once resided, thus forming Fe-oxide around it. Perhaps this presents strong evidence for microbially-mediated precipitation of Fe-oxides at the very least (included in models 5 and 6).

These structures are similar to some of the observed honeycomb-like hollow filaments of Dekov et al. (2007). Visual comparisons of SEM imagery suggest that nontronite and Fe-oxide formation at Seamount 3 likely involves a biogenic model or a mix of biogenic (models 5 and 6) and abiogenic processes (models 3 and 4). It is unclear from the available evidence whether the nontronite from the present study formed through aging processes (model 6, or perhaps model 4) of precursor Fe-oxide or if the nontronite was precipitated directly within EPS of microbes. It is also possible that some of the nontronite and Fe-oxides formed under specific hydrothermal conditions such that they directly precipitated (models 3 and 4).

The surface appearance of the microstructures do not have a well-defined honeycomb exterior like that observed of freshly precipitated nontronite (Köhler et al., 1994; Ueshima and Tazaki, 2001), which offers potential support for models not involving microbes (De Carlo et al., 1983) since the surface features do not entirely match those of biogenic deposits. However, these microstructures look similar to some of the Fe-Si-oxyhydroxides seen in Dekov et al. (2010) and Li et al. (2012). With such high SiO_2 contents in the samples from Seamount 3, it is likely some of the microstructures observed are Si-oxyhydroxides, not just Fe-oxides and nontronite. Perhaps this may explain some of the inconsistencies in morphology with those of strictly nontronite and young (experimentally precipitated) nontronite (Ueshima and Tazaki, 2001).

Several studies discussed the possibility of recrystallization and how this process may change the appearance of the microstructures (Alt, 1988; Köhler et al., 1994). Differences in mineralogy at active sites of hydrothermal deposition compared to non-active sites may be a product of recrystallization processes (Alt, 1988). This may describe some of the observed differences in the chemistry and mineralogy of the Seamount 3 samples and those of possibly more active sites. Alt (1988) described how such differences may actually result from the variable compositions of Si or Al and pore fluid chemical variations in general for available material for such secondary intergrowth. Köhler et al. (1994) provided an SEM collection of

microstructures that show such secondary intergrowth of nontronite, which bear similarities to some of the observed structures of the present study. For such reasons, it is possible that the hydrothermal system of the present study is beginning to deactivate and thus the observed microstructures are more degraded from recrystallization. There are also surface sediments atop of the tubular deposits, suggesting that they are not extremely recent.

6.3 Pattern and tube formation model

The pattern of the tube-shaped sinuous deposits at Seamount 3 is the first of its kind observed in situ. Some structure or feature that is sedimented and not visible is likely controlling the fluid flow, effectively controlling the formation pattern of the deposits by channelizing the fluid flow into the observed pattern. This suggests that there must be formations below the sedimented seafloor that appear to have the opposite pattern to the tubular network. Pillow lavas are common formations on and around seamounts, and were observed on and around Seamount 3 as well as several other seamounts in the Galapagos Archipelago. It is hypothesized that pillow lavas are controlling the distribution of the fluid flow to the surface. Such pillow lavas would be sedimented over time to the point where they are not observable on the surface in most places. Fluid pathways remain open within the gap spaces between pillows and in turn these spaces create winding tubular sinuous patterned deposits on the surface above.

In order to examine this hypothesis, image analysis was performed on ROV bottom photographs of the deposits on Seamount 3 as well as exposed pillow lava fields from the same seamount. The deposits and pillows were traced and their spatial dimensions (major and minor axes) were measured and scaled to the ROV in the same images (Figure 6.1). There is a clear similarity between the spatial dimensions of both of these features (Figure 6.2), suggesting that sedimented pillows control the deposit pattern.

Pillow lava erupts and coalesces with complicated internal structures. In this pillow-controlled fluid flow model, the first phase of the system starts with pillows covering the surface and below the surface as hydrothermal fluids begin to flow up through their cracks (Figure 6.3, 1). Sediments then cover up some of the pillows and fluid flow further develops into channels between pillows (Figure 6.3, 2). Continued sedimentation eventually covers all of the pillows and the tubular deposits begin to form as fluid flow persists along previously established pathways (Figure 6.3, 3). Finally, pillows are completely covered by sediment and tubes continue growing from fluid below (Figure 6.3, 4).

The formation of the tubes is likely a result of the limited crack space for the fluids to come through and then the continuation of the fluid flow from below fueling more precipitation from the inside out. The fluffy or irregular formation of the tubes structure is a product of the possible bacteria living on the surface (Alt, 1988). The hydrothermal fluids may be denser due to the process of phase separation (fractionation of elements between liquid and vapor phases, volatile elements will partition into vapor and ions into liquid) and thus tend to hug the seafloor as well and form horizontally orientated (and in this case tubular) deposits rather than vertical chimneys. It is also possible that the fluid flow is so minimal at Seamount 3 that vigorous plumes are not generated and fluids just seep out along cracks and mix with seawater quickly. Typically diffuse venting fluids do not rise very much but rather cool and dilute quickly, forming deposits at first interactions with the ambient seawater.

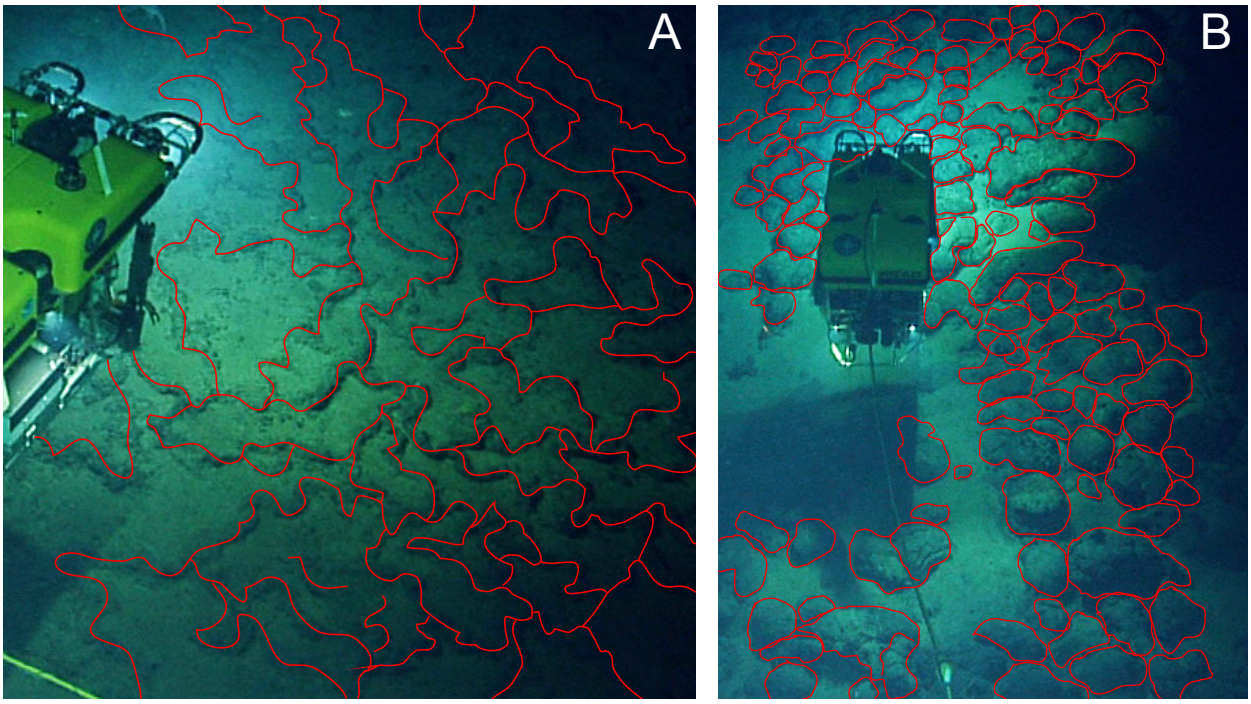

Figure 6.1 (A) Hydrothermal deposits outlined in red. (B) Pillow lavas outlined in red. The spatial dimensions of each closed polygon were measured for image analysis of both hydrothermal deposits and pillow lava. ROV *Hercules* was used for scaling the dimensions of the image measurements. (Images courtesy of the Ocean Exploration Trust.)

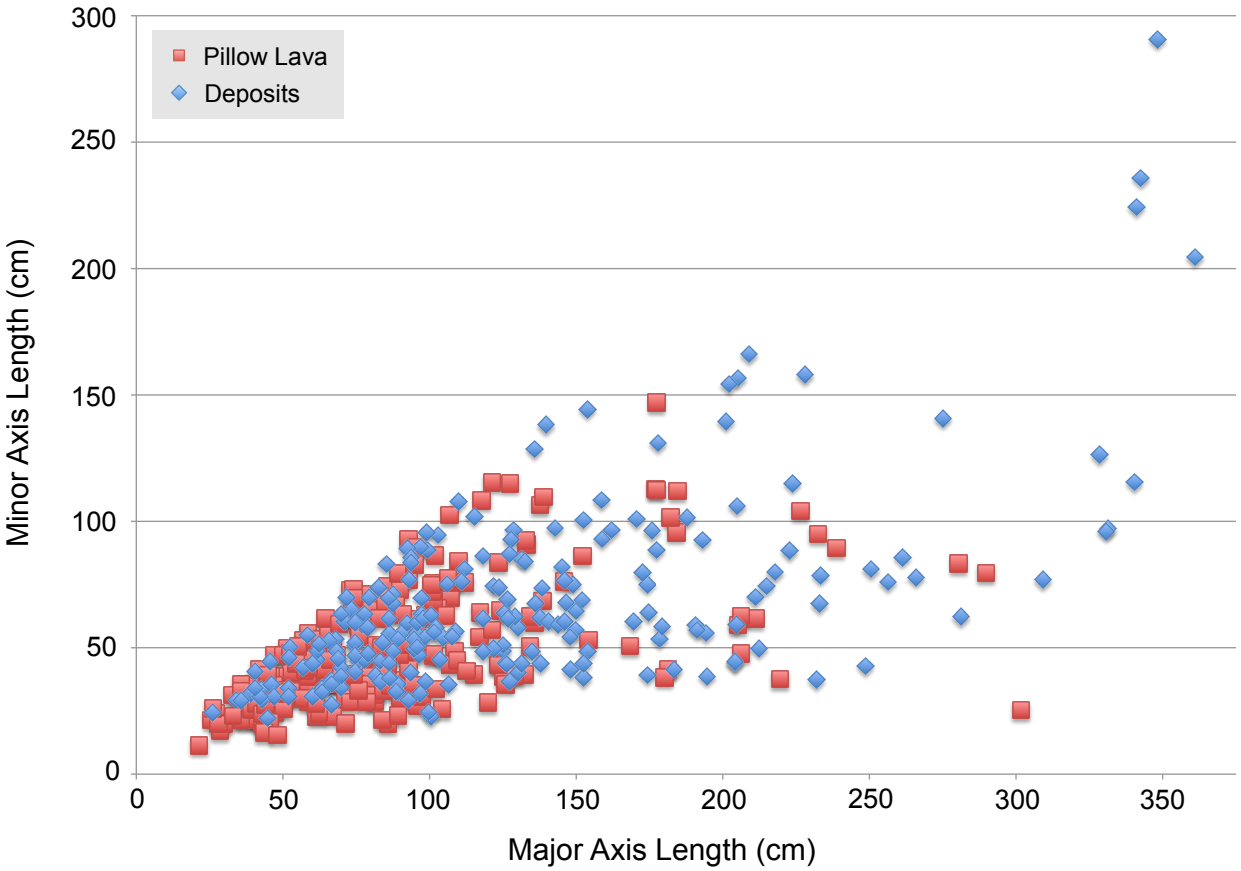

Figure 6.2 Major vs. minor axis length of pillow lavas (red squares) from regions nearby the deposits and the deposits themselves (blue diamonds).

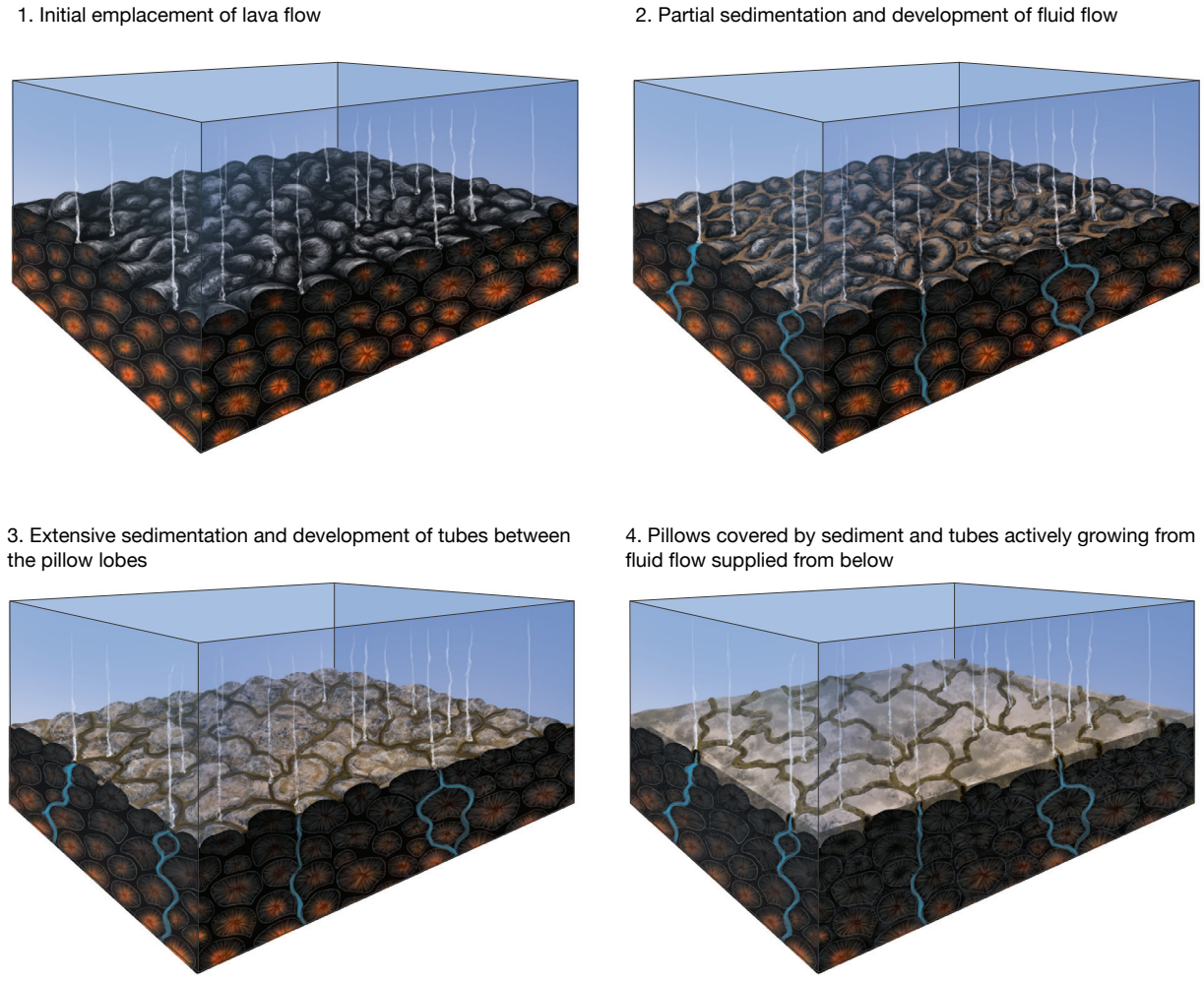

Figure 6.3 Formation model for the tubular sinuous patterned network of deposits. Block model shows the transition from (1) initial emplacement of flow, pillows cover the seafloor and sub-surface with venting fluids above. (2) partial sedimentation and fluid flow development, (3) extensive sedimentation and development of tubes between pillow lobes, and finally (4) pillows fully sedimented with tubes actively growing form fluid flow supplied below the surface. (Figure model designed by Steven Carey and Megan Lubetkin, illustration by Kathleen Cantner).

7. Conclusion

The hydrothermal deposits collected from the summit of Seamount 3, Wolf-Darwin lineament, Galapagos Archipelago, are similar in chemistry and mineralogy to other seafloor nontronites and Fe-Si-oxyhydroxides. The formation of such deposits likely involves some biogenetic processes, as indicated by the presence of bacterial structures and bacterial mats during in situ sampling. The system may be deactivating based on the sedimentation in situ atop the deposits and the observed SEM morphology of possible degraded microtubes with recrystallized nontronite or secondary intergrowth from aging processes (Köhler et al., 1994).

ROV image analysis of spatial dimensions suggests that the unusual patterned network of these hydrothermal deposits is likely controlled by sedimented pillow lavas below the surface. Although this is the first observation of such a patterned network of deposits, it is presumably not extremely rare. Pillow lavas are common formations on and around seamounts as they are the only form of basaltic lava flow in the ocean. There are an estimated 25 million-plus uncharted seamounts of 100 m and up in the world's oceans (Wessel et al., 2010). Thus, this occurrence may be fairly common atop seamounts throughout the world's oceans.

Future studies that explore hydrothermal nontronite formation on seamounts may observe this patterned network and should, if possible, attempt to core the surface or excavate to confirm the presence of pillow lava below the surface. Collecting water samples of venting fluids could also prove helpful for the determination of possible formation hypotheses, so it is suggested that water samples at or near the rock sampling site should also be collected.

8. References

Alt, J. C. (1988). Hydrothermal Oxide and Nontronite Deposits on Seamounts in the Eastern Pacific. Marine Geology 81(227-239).

Alt, J. C., P. Lonsdale, R. Haymon and K. Muehlenbachs (1987). Hydrothermal sulfide and oxide deposits on seamounts near 21ºN, East Pacific Rise. Geological Society of America 98 (157-168).

Anderson, A.T. (1975). Some basaltic and andesitic gases. Reviews of Geophysics and Space Physics, 13, (37-55).

Bao, S., H.Y. Zhou, X.T Peng, F.W. Ji, and H.Q. Yao (2008) Geochemistry of REE and yttrium in hydrothermal fluids from the Endeavor segment, Juan de Fuca Ridge Geochemical Journal, 42, (359-370).

Behn, M.D., C.P. Conrad, and P.G. Silver, (2004). Detection of upper mantle flow associated with the African superplume. Earth Planetary Science Letters 224(259-274).

Bemis, K., R.P. Lowell, and A. Farough. (2012). Diffuse flow on and around hydrothermal vents at mid-ocean ridges. Oceanography 25(1)(182–191). doi.org/10.5670/oceanog.2012.16.

Bibring, J.P., Langevin, Y., Gendrin, A., Gondet, B., Poulet, F., Berthé, M., Soufflot, A., Arvidson, R., Mangold, N., Mustard, J. and Drossart, P. (2005). Mars surface diversity as revealed by the OMEGA/Mars Express observations. Science, 307(1576-1581).

Bischoff. J. L (1972). A ferroan nontronite from the Red Sea Geothermal System. Clays Clay and Minerals 20(217-223).

Bischoff, J. L. (1980). Geothermal system at 21 N, East Pacific Rise: Physical limits on geothermal fluid and role of adiabatic expansion. Science 207(1465-1469). doi: 10.1126/science.1159699

Bishop, J.L., E.Z.N.Dobrea, N.K. McKeown, M. Parente, B.L. Ehlmann, J.R. Michalski, R.E. Milliken, F. Poulet, G.A. Swayze, J.F. Mustard, and S.L. Murchie (2008). Phyllosilicate diversity and past aqueous activity revealed at Mawrth Vallis, Science 321(830-833).

Blumenberg, M., R. Seifert, and W. Michaelis (2007). Aerobic methanotrophy in the oxic–anoxic transition zone of the Black Sea water column. Organic Geochemistry 38.1(84-91).

Boschen, R. E., A.A. Rowden, M. R Clark, & J. P. A Gardner (2013). Mining of deep-sea seafloor massive sulfides: a review of the deposits, their benthic communities, impacts from mining, regulatory frameworks and management strategies. Ocean & Coastal Management 84(54-67).

Cagatay, M.N. (1993). Hydrothermal alteration associated with volcanogenic massive sulfide deposits; examples from Turkey. Economic Geology, 88(606-621).

Chia, W. (2015). Scanning Electron Microscope: Overview. SEM Group 7-3 Blog. http://sem-7-3.blogspot.com/

Cole, T.G. (1988). The nature and origin of smectite in the Atlantis II Deep, Red Sea. The Canadian Mineralogist 26(4)(755-763).

Cole, T.G. and H. F. Shaw (1983). The nature and origin of authigenic smectites in some recent marine sediments. Clay minerals 18(3)(239-252).

Corliss, J. B., M. Lyle, J. Dymond and K. Crane (1978). The chemistry of hydrothermal mounds near the Galapagos Rift. Earth and Planetary Science Letters 40(12-24).

Corliss, J.B., J. Dymond, L.I. Gordon and J.M. Edmond (1979). On the Galapagos Rift. Science 203(16).

Corliss, J.B., J.A. Baross and S.E. Hoffman (1981). An Hypothesis Concerning the Relationships Between Submarine Hot Springs and the Origin of Life on Earth. Oceanologica Acta, Special issue.

Cox, A. and B.R. Hart (2009) Plate Tectonics: How it Works. Hoboken, NJ, USA: Wiley-Blackwell, 2009. ProQuest ebrary.

DeCarlo, E. H., G. M. McMurtry and H.-W. Yeh (1983). Geochemistry of hydrothermal deposits from Loihi submarine volcano, Hawaii. Earth and Planetary Science Letters 66(438-449).

Deer, W.A., R.A. Howie, W.S. Wise and J. Zussman (1963). Rock-forming minerals. Vol. 4B, Framework silicates: silica minerals, feldspathoides and the zeolites. Geological Society.

Dekov, V. M., G. D. Kamenov, J. Stummeyer, M. Thiry, C. Savelli, W. C. Shanks, D. Fortin, E. Kuzmann and A. Vertes (2007). Hydrothermal nontronite formation at Eolo Seamount (Aeolian volcanic arc, Tyrrhenian Sea). Chemical Geology 245(103-119).

Dekov, V. M., S. Petersen, C.-D. Garbe-Schonberg, G. D. Kamenov, M. Perner, E. Kuzmann and M. Schmidt (2010). Fe-Si-oxyhydroxide deposits at a slow-spreading centre with thickened oceanic crust: The Lilliput hydrothermal field (9°33′S, Mid-Atlantic Ridge). Chemical Geology 278(186-200).

Delaney, P., H.J. Choi, J. Ihm, S.G. Louie and M.L. Cohen (1998). Broken symmetry and pseudogaps in ropes of carbon nanotubes. Nature 391, 6666, (466-468).

Dill, H.G., G. Siegfanz, and V. Marchig (1994). Mineralogy and chemistry of metalliferous muds forming the topstratum of a massive sulfide- metalliferous sediment sequence from East Pacific Rise 18°S: its origin and implications concerning the formation of ochrous sediments in Cyprus-type deposits. Marine Georesources and Geotechnology, 12 (2), (159–180).

Douville, E., P. Bienvenu, J.L. Charlou, J.P. Donval, Y. Fouquet, P. Appriou and T. Gamo (1999). Yttrium and rare earth elements in fluids from various deep-sea hydrothermal systems. Geochimica et Cosmochimica Acta, 63(5) (627-643).

Dymond, J. and W. Eklund (1978). A microprobe study of metalliferous sediment components. Earth and Planetary Science Letters 40(2)(243-251).

Edmond, J. M., C. Measures, B. Magnum, B. Grant, F. R. Sclater, R. Collier, A. Hudson, L. I. Gordon and J. B. Corliss (1979). On the formation of metal-rich deposits at ridge crests Earth and Planetary Science Letters 46(19-30).

Edmond, J.M., C. Measures, R.E. McDu, L.H. Chan, R. Collier, B. Grant, L.I. Gordon, and J.B. Corliss. (1979). Ridge crest hydrothermal activity and the balances of the major and minor elements in the ocean: e Galapagos data. *Earth and Planetary Science Letters.* 46, (1–18).

Ehlmann, B.L., J.F. Mustard, S.L. Murchie, J.P. Bibring, A. Meunier, A. A. Fraeman and Y. Langevin (2011). Subsurface water and clay mineral formation during the early history of Mars. Nature, 479(7371)(53-60).

Eisenhour, D.D. and R. K. Brown (2009). Bentonite and its impact on modern life. Elements 5(2)(83-88).

Embley, R.W., E.T. Baker, W.W. Chadwick, J.E. Lupton, J.A. Resing, G.J. Massoth, and K. Nakamura (2004). Explorations of Mariana Arc volcanoes reveal new hydrothermal systems. Eos. Transactions American Geophysical Union, 85(4)(37-40).

Emerson, D., E. J. Fleming and J. M. Mcbeth (2010). Iron-Oxidizing Bacteria: An Environmental and Genomic Perspective Annual Review of Microbiology 561-579.

Emerson, D. and C. L. Moyer (2002). Neutrophilic Fe-Oxidizing Bacteria Are Abundant at the Loihi Seamount Hydrothermal Vents and Play a Major Role in Fe Oxide Deposition. Applied and Environmental Microbiology 68(6)(3085-3093).

Feighner, M. A., and M.A. Richards (1994). Lithospheric structure and compensation mechanisms of the Galápagos Archipelago. Journal of Geophysical Research: Solid Earth, 99(B4)(6711-6729).

Fortin, D., F.G. Ferris and S.D. Scott (1998). Formation of Fe-silicates and Fe-oxides on bacterial surfaces in samples collected near hydrothermal vents on the Southern Explorer Ridge in the northeast Pacific Ocean. American Mineralogist 83(11)(1399-1408).

Freundchen (2012). Illustration of the Bragg diffraction. Wikimedia Commons. https://commons.wikimedia.org/wiki/File:Bragg_XRD.svg

Gainey, S.R., E.M. Hausrath, J.A. Hurowitz, and R.E. Milliken (2014) Nontronite dissolution rates and implications for Mars. Geochimica et Cosmochimica Acta.126, (192–211).

Geist, D., B. A. Diefenbach, D. J. Fornari and M. D. Kurz (2006). Construction of the Galápagos platform by large submarine volcanic terraces. Geochemistry, geophysics, geosystems G3 9(3) doi: 10.1029/2007GC001795.

Green, K. E., R. P. V. Herzen and D. L. Williams (1981). The Galapagos Spreading Center at 86ºW: A Detailed Geothermal Field Study Journal Of Geophysical Research 86(B2)(979-986).

Grill, E.V., R.L. Chase, R.D. MacDonald and J.W. Murray (1981). A hydrothermal deposit from Explorer Ridge in the northeast Pacific Ocean. Earth and Planetary Science Letters, 52(1)(142-150).

Gripp, A. E. and R. G. Gordon (2002). Young tracks of hotspots and current plate velocities. Geophysical Journal International 150(2)(321-361).

Hammond, S. R. (1997) Offset caldera and crater collapse on Juan de Fuca ridge-flank volcanoes. *Bull. Volcanol.* 58, (617–627).

Harder, H. (1976). Nontronite synthesis at low temperatures. Chemical Geology 18(3)(169-180).

Harder, Hermann. (1978) Synthesis of iron layer silicate minerals under natural conditions. Clays and Clay Minerals 26.1(65-72).

Hekinian, R., B.R. Rosendahl, D.S. Cronan, Y. Dmitriev, R.V. Fodor, R.M. Goll, M. Hoffert, S.E. Humphris, D.P. Mattey, J. Natland, N. Peterson, W. Roggenthen, E.L. Schrader, R.K. Srivastava and N. Warren (1978). Hydrothermal deposits and associated basement rocks from the Galapagos spreading center. Oceanologica Acta, 1(473-482).

Hekinian, R., M. Hoffert, P. Larque, J.L. Cheminee, P. Stoffers and D. Bideau (1993). Hydrothermal Fe and Si oxyhydroxide deposits from South Pacific intraplate volcanoes and East Pacific Rise axial and off-axial regions. Economic Geology, 88(8)(2099-2121).

Hey, R., G.L. Johnson and A. Lowrie (1977). Recent plate motions in the Galapagos area. Geological Society of America Bulletin 88(10)(1385-1403).

Hoagland, P., S. Beaulieu, M.A.Tivey, R.G. Eggert, C.German, L. Glowka and J. Lin (2010). Deep-sea mining of seafloor massive sulfides. Marine Policy 34(3)(28-732).

Hoffert, M., A. Perseil, R. Hekinian, P. Choukroune, H.D. Needham, J. Francheteau, and X. Le Pichon (1978) Hydrothermal deposits sampled by diving saucer in transform fault A near 37°N on the Mid-Atlantic Ridge, FAMOUS area. Oceanologica Acta 1 (1), (73–86).

Honnorez, J., R.P. von Herzen, T.J. Barrett, K. Becker, M.L. Bender, P.E. Borella, H.W. Hubberten, S.C. Jones, S.I. Karato, C. Laverne and S. Levi (1981). Hydrothermal mounds and young ocean crust of the Galapagos: Preliminary Deep Sea Drilling results, Leg 70. Geological Society of America Bulletin, 92(7)(457-472).

Humphris, S.E. and T. McCollom (1998). The cauldron beneath the seafloor. Oceanus, 41(2)(18).

Humphris, S.E., P.M. Herzig, D.J. Miller, J.C. Alt, K. Becker, D. Brown, G. Brugmann, H. Chiba, Y. Fouquet, J.B. Gemmell and G. Guerin (1995). The internal structure of an active sea-floor massive sulfide deposit. Nature 377(6551)(13-716).

Isphording, W. C (1975). Primary nontronite from the Venezuelan Guayana. American Mineralogist 60(840-848).

Jens Molecular and Nanoscale Analysis Laboratory. ICP-MS Instrumentation. http://eecelabs.seas.wustl.edu/ICP-MS.aspx

Kelley, K. A., T. Plank, J. Ludden, and H. Staudigel, (2003) Composition of altered oceanic crust at ODP Sites 801 and 1149, Geochemistry Geophysics Geosystems, 4(6), 8910.

Klein, E. M., C. H. Langmuir, and H. Staudigel, (1991) Geochemistry of basalts from the southeast Indian Ridge, 115°E – 138°E, J. Geophys. Res., 96, 2089–2107.

Kloprogge JT, S. Komarneni and J.E. Amonette (1999). Synthesis of smectite clay minerals: A critical review. Clays and Clay Minerals 47(529–554)

Koeppenkastrop, D. and H. Eric (1992). Sorption of rare-earth elements from seawater onto synthetic mineral particles: An experimental approach. Chemical geology, 95(3)(251-263).

Köhler, B., A. Singer, and P. Stoffers (1994) Biogenic nontronite from marine white smoker chimneys. Clay and Clay Minerals, 42, 6, (689-701).

Köster, H.M., U. Ehrlicher, A. Gilg, R. Jordan, E. Murad, and K. Onnich (1999) Mineralogical and chemical characteristics of five nontronites and Fe-rich smectites. Clay Minerals, (579-599).

Li, J., H. Zhou, X. Peng, Z. Wu, S. Chen, and J. Fang (2012) Microbial diversity and biomineralization in low-temperature hydrothermal iron-silica-rich precipitates of the Lau Basin hydrothermal field. FEMS Microbial Ecology, 81, (205-216).

Loizeau, D., Mangold, N., Poulet, F., Bibring, J.P., Gendrin, A., Ansan, V., Gomez, C., Gondet, B., Langevin, Y., Masson, P. and Neukum, G., 2007. Phyllosilicates in the Mawrth Vallis region of Mars. Journal of Geophysical Research: Planets, 112(E8).

Malahoff, A., G.M. McMurtry, J.C. Wiltshire and H.W. Yeh, (1982). Geology and chemistry of hydrothermal deposits from active submarine volcano Loihi, Hawaii. Nature 298(234 – 239) doi:10.1038/298234a0

Malahoff, A., R.H. Feden and H.S. Fleming (1982). Magnetic anomalies and tectonic fabric of marginal basins north of New Zealand. Journal of Geophysical Research: Solid Earth 87(B5)(4109-4125).

Martin, W., J. Baross, D. Kelley, and M.J. Russell (2008) Hydrothermal vents and the origin of life. Nature Reviews. Microbiology, 6, (805-814).

McBirney, A. R. and H. Williams (1969). Geology and Petrology of the Galápagos Islands. GSA Memoirs 118(1-197).

McMurtry, G. M., P. N. Sedwick, P. Fryer, D.L. Vonderhaar and H.W. Yeh (1993). Unusual geochemistry of hydrothermal vents on submarine arc volcanoes: Kasuga Seamounts, Northern Mariana Arc. Earth and Planetary Science Letters 114(4)(517-528)

Miller, D. M., C. H. Langmuir, S. L. Goldstein, and A. L. Franks (1992) The importance of parental magma composition to calc-alkaline and tholeiitic evolution: evidence from Umnak Island in the Aleutians, Journal of Geophysical Res., 97, (321-343).

Mittelstaedt, E., A. Davaille, P.E. Van Keken, N. Gracias and J. Escartin, (2010). A noninvasive method for measuring the velocity of diffuse hydrothermal flow by tracking moving refractive index anomalies. Geochemistry, Geophysics, Geosystems, 11(10)doi: 10.1029/2010GC003227

Morgan, W.J., (1978) Rodriguez, Darwin, Amsterdam..., a second type of hotspot island, J. *Geophys. Res.*, 83, (5355-5360).

Murnane, R. and D. A. Clague (1983). Nontronite from a low-temperature hydrothermal system on the Juan de Fuca Ridge. Earth and Planetary Science Letters 65(343-352).

Nordlie, B. E. (1973). Morphology and Structure of the Western Galápagos Volcanoes and a Model for Their Origin. Geological Society of America Bulletin 84(9)(2931-2956).

Peterson, D.W. and R.I. Tilling, (1980). Transition of basaltic lava from pahoehoe to aa, Kilauea Volcano, Hawaii: field observations and key factors. Journal of Volcanology and Geothermal Research 7(3)(271-293).

Poulet, F., J.P. Bibring, J.F Mustard, A. Gendrin, N. Mangold, Y. Langevin, R.E. Arvidson, B. Gondet, C. Gomez, M. Berthé, and S. Erard (2005). Phyllosilicates on Mars and implications for early Martian climate. Nature 438(7068)(623-627).

Rakovan, J. (2005) Pillow Basalt. Word to the Wise. Rocks & Minerals, 80, (287).

Ross, C.S. and S.B. Hendricks (1945). Minerals of the montmorillonite group, their origin and relation to soils and clays. Professional Paper (No. 205-B).

Rozenson, I. and L. Heller-Kallai (1976). Reduction and oxidation of Fe3+ in dioctahedral smectites-1: Reduction with hydrazine and dithionite. Clays and Clay Minerals 24(271-282).

Severmann, S., C.M. Johnson, B.L. Beard, C.R. German, H.N. Edmonds, H. Chiba and D.R.H. Green (2004). The effect of plume processes on the Fe isotope composition of hydrothermally derived Fe in the deep ocean as inferred from the Rainbow vent site, Mid-Atlantic Ridge, 36 14′ N. Earth and Planetary Science Letters 225(1) (63-76).

Severmann, S., R.A. Mills, M.R. Palmer and A.E. Fallick. (2004). The origin of clay minerals in active and relict hydrothermal deposits. Geochimica et Cosmochimica Acta, 68(1)(73-88).

Scheirer, D.S., T.M. Shank and D.J. Fornari (2006). Temperature variations at diffuse and focused flow hydrothermal vent sites along the northern East Pacific Rise. Geochemistry, Geophysics, Geosystems 7(3).

Shanks, W.C. and J.L. Bischoff (1977). Ore transport and deposition in the Red Sea geothermal system: a geochemical model. Geochimica et Cosmochimica Acta 41(10)(1507-1519).

Sherman, G.D., H. Ikawa, G. Uehara, and E. Okazaki (1962) Types of Occurrence of Nontronite and Nontronite-like Minerals in Soils. Pacific Science, Vol. XVI, (57-62).

Singer, A., P. Stoffers, L. Heller-Kallai and D. Szafranek (1984). Nontronite in a deep-sea core from the South Pacific. Clays and Clay Minerals 32(375-383).

Singer, A. and P. Stoffers (1987). Mineralogy of a hydrothermal sequence in a core from the Atlantis II Deep, Red Sea. Clay Minerals 22(3)(251-267).

Sinton, C. W., D. M. Christie and R. A. Duncan (1996). Geochronology of Galapagos seamounts. Journal of Geophysical Research: Solid Earth 101(B6)(13689-13700).

Stakes, D.S. and J.R. O'Neil (1982). Mineralogy and stable isotope geochemistry of hydrothermally altered oceanic rocks. Earth and Planetary Science Letters, 57(2)(285-304).

Stoffers, P., A. Singer, G. McMurtry, A. Arquit and H.W. Yeh (1990). Geochemistry of a hydrothermal nontronite deposit from the Lau Basin, Southwest Pacific. Geologisches. Jahrbuch D, 92(615-628).

Stumm, W. and J.J. Morgan, (1981). Aquatic chemistry: an introduction emphasizing chemical equilibria in natural waters. John Wiley.

Sun, S.S. and W.F. McDonough (1989). Chemical and isotopic systematics of oceanic basalts: implications for mantle composition and processes. Geological Society, London, Special Publications, 42(1)(313-345).

Tazaki, K. (1997). Biomineralization of layer silicates and hydrated Fe/Mn oxides in microbial mats; an electron microscopical study. Clays and Clay Minerals, 45(2)(203-212).

Tazaki, K. (1999). Architecture of biomats reveals history of geo-, aqua-, and bio-systems. Episodes Journal of international Geoscience 22(21-25).

Thompson, G., S.E. Humphris, B. Schroeder, M. Sulanowska and P.A. Rona (1988). Active vents and massive sulfides at 26 degrees N (TAG) and 23 degrees N (Snakepit) on the Mid-Atlantic Ridge. The Canadian Mineralogist 26(3)(697-711).

Tivey, M.K. (2007). Generation of seafloor hydrothermal vent fluids and associated mineral deposits. Oceanography 20(1)(50–65) doi.org/10.5670/oceanog.2007.80.

Ueshima, M. and K. Tazaki (2001). Possible Role of Microbial Polysaccharides in Nontronite Formation Clays and Clay Minerals 49(4): 292-299.

Von Damm, K.L. and M.D. Lilley (2004). Diffuse flow hydrothermal fluids from 9 50′ N East Pacific Rise: Origin, evolution and biogeochemical controls. The Subseafloor Biosphere at Mid-Ocean Ridges (245-268).

Wessel, P., D.T. Sandwell and S.S. Kim (2010). The global seamount census. Oceanography 23(1)(24).

Wilson, D.S. and R.N. Hey (1995). History of rift propagation and magnetization intensity for the Cocos-Nazca sspreading Center. Journal of Geophysical Research: Solid Earth 100(B6)(10041-10056).

Winter, J.D. (2009). Principles of Igneous and Metamorphic Petrology (2nd Edition) Pearson.

Wray, J.J., S.L. Murchie, S.W. Squyres, F.P. Seelos and L.L. Tornabene (2009). Diverse aqueous environments on ancient Mars revealed in the southern highlands. Geology 37(11)(1043-1046).

Wyllie, P. J. (1988). Solidus curves, mantle plumes, and magma generation beneath Hawaii. Journal of Geophysical Research 93(B5)(4171–4181).

Appendix A: Detailed analytical methodology

A.1 X-Ray Diffraction

X-ray diffraction (XRD) is an analytical method used to characterize the mineralogy of a sample. Minerals consist of many atoms that are organized in a regular periodic way. This organized arrangement of atoms within a mineral is referred to as its crystal lattice. The space between layers of the lattice is referred to as the d spacing.

X-rays, a form of electromagnetic radiation, interact with crystal lattices in a specific way. When a wave of directed X-rays strikes a plane of regularly organized atoms within the lattice, the scatterers (which in this case are the electrons that are part of each atom) re-radiate some of the intensity of the incoming X-rays in the form of a spherical wave. These spherical waves of X-rays are also regularly arrayed. Under specific conditions the re-radiated spherical waves will interfere constructively and thus create a reflection spot on the recorded diffraction pattern.

These specific conditions are outlined by Bragg's Law (Equation A.1). Bragg's Law equation describes the relationship between a whole number n, the wavelength of the incoming X-rays as λ, *d* as the spacing between planes of the lattice, and θ is the angle that the incoming rays makes when it hits the first plane of the lattice. Two beams of X-rays are directed toward the plane of the lattice, which creates a specific angle, theta. Once these X-rays are re-radiated by the scatterers within the lattice, the spherical waves will interfere constructively only when they travel a distance that differs by a whole number multiple (n) of their wavelength, that is when the two waves are fully in-phase. In this case, the upper of the two waves will travel a shorter distance, that of $d \sin\theta$ less. If the wavelength of the X-rays is known and the angle theta that the two X-rays create as they hit the lattice plane is measured, then the d spacing between the arrays of atoms may be determined based on this law. This relationship is illustrated in Figure A.1.

$$n\lambda = 2d\sin\theta \qquad \textbf{Equation A.1}$$

The six sub-samples were crushed as described in the materials and methods section. The resulting powders consisted of fine grain sizes appropriate for powder X-ray diffraction in the Rigaku Miniflex diffraction system. Powder diffraction mounts were prepared for each of the six samples. A flat piece of glass was pressed evenly over the surface of the mount to produce a consistent plane for X-ray diffraction measurement. All six mounts were placed in a six-position auto-sampler (Figure A.2). Diffracted X-rays are detected by the machine at several different angles. D-values and percent composition of the sample are derived from this data. This derivation is completed using Bragg's Law as described above.

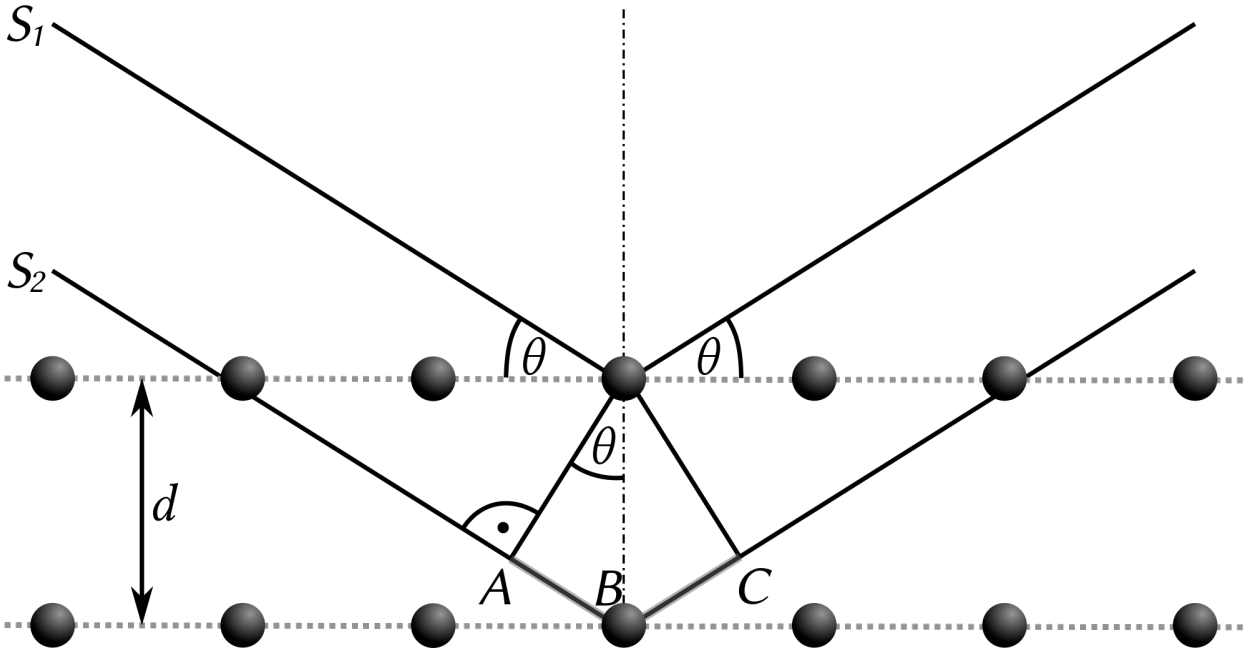

Figure A.1 Illustration of Bragg's Law (Equation A.1). S_1 and S_2 represent the two incoming beams of X-rays (which are also waves). The dark circles are individual atoms aligned in a crystal lattice. The space between the layers of the lattice is *d* and the angle created by the intersection of the X-ray beams with the first plane of the lattice is θ. (Figure by Freundchen, Wikimedia Commons, 2012)

Figure A.2 (LEFT) Six-position auto-sampler inside of the Rigaku Miniflex diffraction system. All six powdered sub-samples are shown in their prepared mounts. Each sample holder is 2.54 cm across. (RIGHT) Rigaku MiniFlex II table top XRD.

A.2 Scanning Electron Microscopy

A scanning electron microscope (SEM) is a type of microscope that uses a beam of fast moving electrons rather than a light source to capture images or electron micrographs of the microscopic features of a sample (Figure A.3). The sample or specimen is prepared with a coating to avoid charging while scanning the image. This coating makes the sample conductive and suitable for imaging with electrons. The electron beam directed at the specimen is a current; if the specimen is not conductive then the current cannot go to ground. Therefore, if the specimen is not conductive, it will act as a resistor and accumulate electrons, similar to a crude lens.

There are two types of coatings that may be used, carbon or a mix of gold and palladium. For SEM work, the gold and palladium coating is more effective at producing clearer images, while the carbon coating is more suitable for EDS work. The gold and palladium coating is better for imaging purposes because it is a better conductor so it reduces charging that may lead to unwanted artifacts in the images. The gold and palladium coating is applied using a sputtering method that lays the coating on the specimen more evenly. Through the process of sputtering, a much finer and more uniform grain size is applied to the surface of the specimen. This helps improve appearance while making it highly conductive.

Samples were coated in gold-palladium imaging analysis. A small chunk of each sub-sample was glued to an aluminum stub and coated in gold and palladium using the Anatech USA Hummer Sputtering System. Stubs are placed in a specimen holder and injected into the specimen chamber. Electrons do not travel far or very well in air so it is necessary to remove all air within the specimen chamber to create a vacuumed space for imaging with electrons.

An anode attracts the electrons and accelerates them into a strong beam. The SEM sends the beam of electrons through a series of coil-shaped electromagnets, which focus and direct the beam of electrons in a specific and precise direction toward the targeted region (Figure A.3). As the beam moves closer to the targeted region of the sample, a set of scan coils steers the electron beam back and forth so that it may scan the full targeted region rather than just a single point. Electrons from the channelized scanning beam hit the surface of the sample and this interaction causes two types of electrons to come off.

Atoms on the surface can absorb the energy of the electrons and then give off their own electrons as the electron beam hits the sample's surface. These secondary electrons are detected by the secondary electron detector. Shallow surface electrons are effective for creating an image of the surface. Backscatter electrons are from the original electron beam itself. Electrons from the beam are reflected off the surface of the sample and may originate from slightly deeper in the sample. A different detector reads these backscatter electrons to help enhance the image quality.

Backscatter electrons may also get trapped deep inside the sample. Deep electrons inside the sample cannot reflect. Their energy is emitted in the form of X-rays, which may be read by a third detector. An SEM image or electron micrograph is created through this process.

In this study, the electron micrographs were created only using the secondary electrons. Beam current would need to be higher in order to collect any backscatter information to create the SEM image or micrograph.

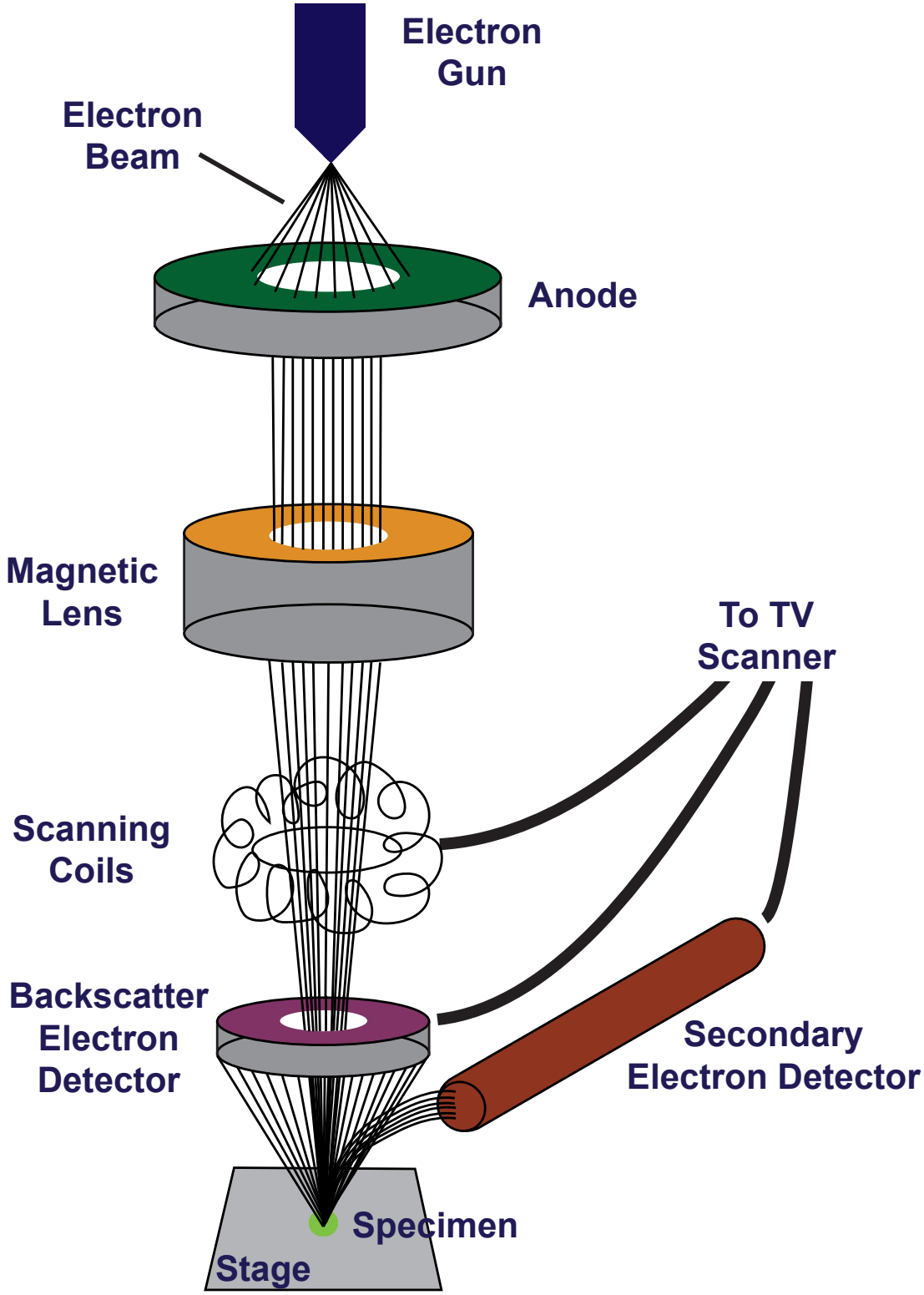

Figure A.3 SEM-EDS diagram illustrating how the initial electrons are focused, directed, and scanned across the surface of a sample to create an electron micrograph or SEM image and to collect EDS data. Figure modified from Chia, 2015.

A.3 Energy-Dispersive X-Ray Spectroscopy

Energy-Dispersive X-Ray Spectroscopy (EDS) is a procedure used along with SEM to identify the occurrence and abundance of a variety of elements within a mineral sample (Figure A.3). Specific targeted areas are selected with the SEM and then analyzed individually as opposed to a whole sample or bulk composition technique (such as ICP-MS or ICP-AES). It is most effective when used to identify the abundance of elements in a homogenous mineral grain, but may also be used to identify the elemental make-up of a small section of a heterogeneous unknown mineral sample.

Every element has a unique atomic structure and will emit X-radiation (composed of X-rays) of a specific characteristic energy. The objective of EDS is to trigger the elements present within a sample to give off their characteristic X-rays such that the elements may be identified by their energies. The atoms must be excited by an outside force, such as a beam of highly charged particles. When the beam of charged particles, such as high-energy electrons or X-rays, hit the specific region of the sample, elements within this part of the sample will be excited and thus emit their characteristic X-rays. This occurs when the incident beam is directed toward the specimen through the electron gun and further focused by a series of condenser lenses (Figure A.4). As the beam strikes the sample, an electron within an inner shell of each element present will be excited and forced to eject leaving an electron hole. An electron from an outer higher-energy shell will fill this hole and in the process it will release energy as it moves from higher to lower energy shells. This energy is released in the form of X-rays, as well as heat and light. The intensity of these released X-rays is what is characteristic about the atom because of its unique structure, and thus it is representative of the elements in the targeted region of the sample.

The EDS detector records the energy of the emitted X-rays in kilovolts (kV) and the intensity or the number of X-rays in counts per second (cps). The intensity of the emitted X-rays is proportional to the abundance of the given element. In EDS spectra, the energy in kV is plotted on the X-axis while the intensity in cps is plotted on the Y-axis. A high peak, for example, observed at a specific energy suggests that the element with characteristic X-radiation of the corresponding energy is present as well as abundant since the peak is high, which suggests that many cps were read. EDS data is generated in weight % for each element detected. In order to generate useful data, where appropriate, elemental weight % was converted to oxide weight % and totals were re-normalized to 100 (for detailed results see Appendix B).

In this study, study EDS was utilized on targeted locations throughout several subsamples to identify the elemental make-up of a small section of heterogeneous unknown minerals. Each of these subsamples was glued to a small cylindrical aluminum mount. Most samples used for

EDS analysis were coated in carbon although some EDS data was collected off gold-palladium coated specimens. Specimens were coated in carbon with the Denton Vacuum Inc. DV-401 Carbon Coating System for imaging of surfaces where EDS analyses were performed. To capture images of the regions that EDS analyses were performed, electron micrographs were taken at each EDS analysis location. Carbon is most effective for EDS analyses of minerals and rocks because C typically will not be present in the specimens, while gold and palladium may be. By collecting EDS data from both C-coated and Au-Pd-coated specimens, it was possible to get accurate readings of Au-Pd (for the C-coated) and C (Au-Pd-coated) specimens.

A.4 Inductively Coupled Plasma Mass Spectrometry

The chemical composition of the samples was determined by inductively coupled plasma mass spectrometry (ICP-MS) for rare earth elements (REE), trace elements, and for P_2O_5 and K_2O. The ICP-MS (Figure A.4) ionizes dissolved samples with inductively coupled plasma, which is energy from electromagnetic induction (time-varying magnetic fields). For this instrument, the ion-generating source is argon plasma. A quadrupole mass spectrometer then separates and measures the ions. The quadrupole carries AC and DC current such that only specific ions will make it through.

First an auto sampler sucks the liquid sample material out of small vials. Then it nebulizes, creates a spray, and enters into the plasma. This heats samples again to high temperatures, in order to excite them to ionize. At this point they enter the mass spectrometer. Pressures are very low such that ions go down channels with magnetic fields where ions of the "wrong size" will smash into the wall or desired ions go straight through the tube (since they have the perfect mass). Magnetic fields are used to selectively filter certain masses of ions over others in this process. When ions make it through the quadrupole, they hit several dynodes (metal plates) and cause a cascade of electrons. These electrons are proportional to the incoming ions and are exponentially magnified. The final detector reads electrons in counts per second and measure the mass of the ion and how much made it through the ion channel detection.

ICP-MS is very fast and more precise and much more sensitive than ICP-AES (Figure A.4). ICP-MS can measure one part per quadrillion so it is an excellent tool for trace and rare earths than may be present at very small concentrations.

Sample preparation for ICP-MS analysis involved dissolution of powdered samples in HF-HNO_3 acid digestion (methodology from Kelley et al., 2003) and was performed by Katie Kelley at the University of Rhode Island Graduate School of Oceanography. In this methodology, 0.05 g of powdered sample (crushed and powdered with a mixer mill) is measured and placed into 23 mL Savillex Teflon beakers. 3 ml of 8NHNO_3 and 1ml of HF are added to the powdered samples in each beaker. Samples are digested and evaporated to dryness overnight on a hot plate at 90ºC. These digested and dried samples are dissolved back into 3 ml of 8NHNO_3 and 3 ml of deionized water. Then they are diluted with deionized water to 2000x the original powder weight within HDPE bottles and sonicated for a duration of 30 minutes.

Kelley et al.'s (2003) methodology is very effective because it does not include HCl and $HClO_4$ as some ICP-MS methods do. This minimizes molecular interferences.

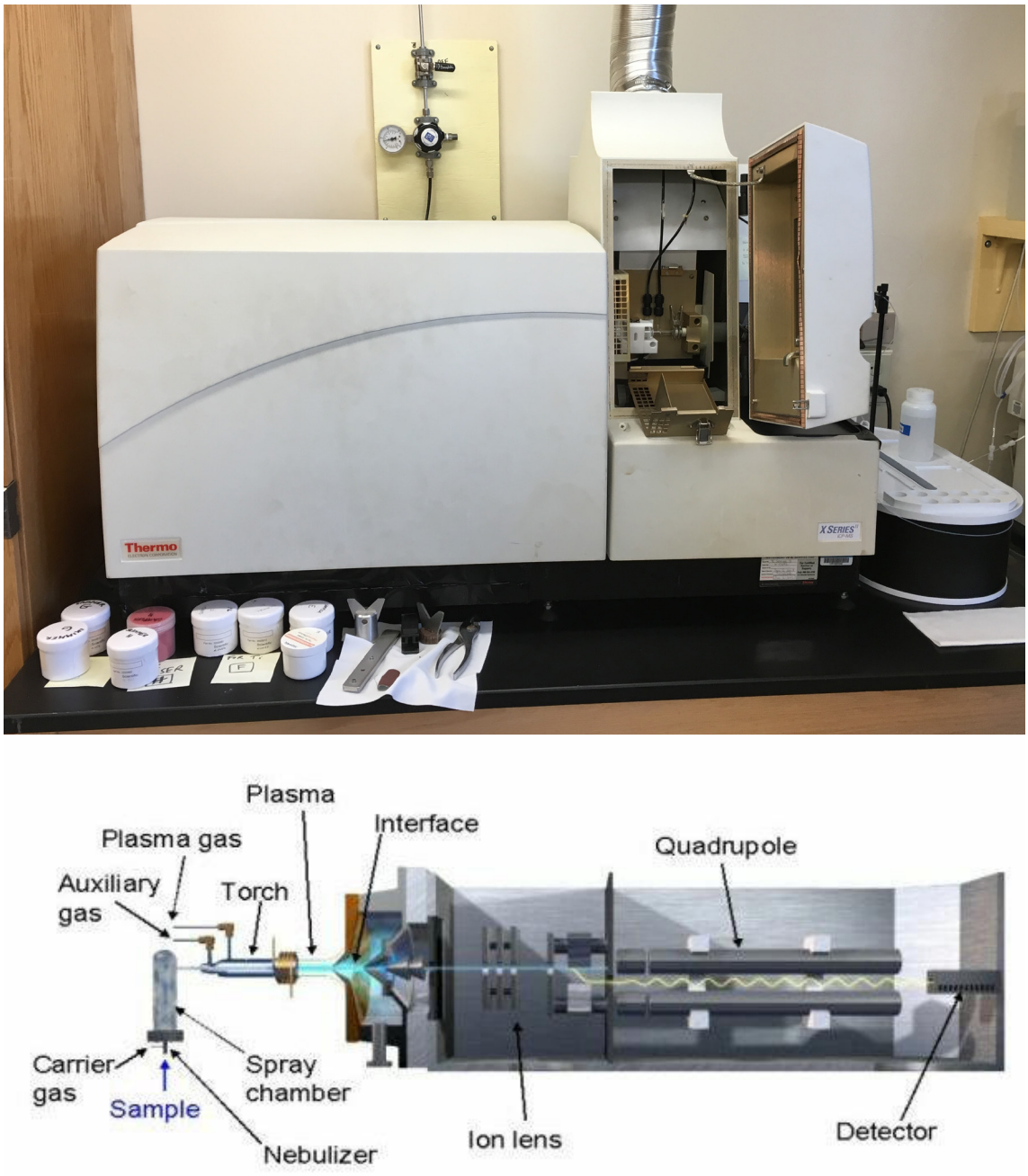

Figure A.4 (ABOVE) The ICP-MS at URI Graduate School of Oceanography. The opened section of the instrument on the right contains the torch and the ICP componant. While the closed section of the instrument on the left contains the quadrupole mass spectrometer. (BELOW) Diagram of ICP-MS from Jens Molecular and Nanoscale Analysis Lab.

A.6 Inductively Coupled Plasma Atomic Emission Spectrometry

Major elemental compositions for SiO_2, MnO, Fe_2O_3, MgO, TiO_2, CaO, Al_2O_3, and Na_2O were determined by inductively coupled plasma atomic emission spectroscopy (ICP-AES; Figure A.5). Similar to ICP-MS, the first half of this instrument works in the same way as it ionizes dissolved samples with inductively coupled plasma. ICP-AES is less precise and less sensitive in comparison to the ICP-MS. For this reason, it is more suitable for measuring compositions of major oxides present in the samples.

For ICP-AES, first an auto sampler sucks up the liquid sample continuously, and enters it into the nebulizer where the liquid is turned into a gas. In order to detect an atom from atomic emission, it must be a gas. Again, the plasma is made of argon gas, which will atomize everything (excite the atoms). These atoms will eventually drop back down to ground state and emit light (Figure A.6). This light is a different wavelength depending on the atom. These characteristic wavelengths are then detected. Radiofrequency (RF) coils receive the light signals. The ICP-AES may be tuned specifically to detect only a select range of nanometers for specific wavelengths of specific desired atoms.

Sample preparation for ICP-AES analysis also followed the methodology from Kelley et al. (2003) and was performed by Katie Kelley at the University of Rhode Island. In this procedure, solutions are prepared using $LiBO_2$ flux-fusions (Klein et al., 1991). 0.2 g of each sample is powdered and dried in Al crucibles within a 100°C muffle furnace. The dry weight is recorded after one hour. Then crucibles are heated to 950°C in a muffle furnace. After 45 min they are weighed again. These weights are used to measure the mass loss on ignition (LOI). 0.1 g of the ignited powder is measured and placed in new crucibles (high-purity graphite). Within these crucibles is 0.4 g of $LiBO_2$ flux which mixes with the sample. Crucibles are placed into a muffle furnace at 1050°C for 15 min. HDPE bottles are prepared and filled with 50 ml of 5% HNO_3. Molten beads from the crucibles are poured into HDPE bottles and shaken until fully dissolved. Clean HDPE bottles are prepared and contain 70 ml of 5% HNO_3. 10 ml of solution for each sample is pulled up and ejected out of syringes through 0.45 mm filters into these HDPE bottles. These new solutions are diluted at about 860x the total weight of the solids and 4300x the original sample weight.

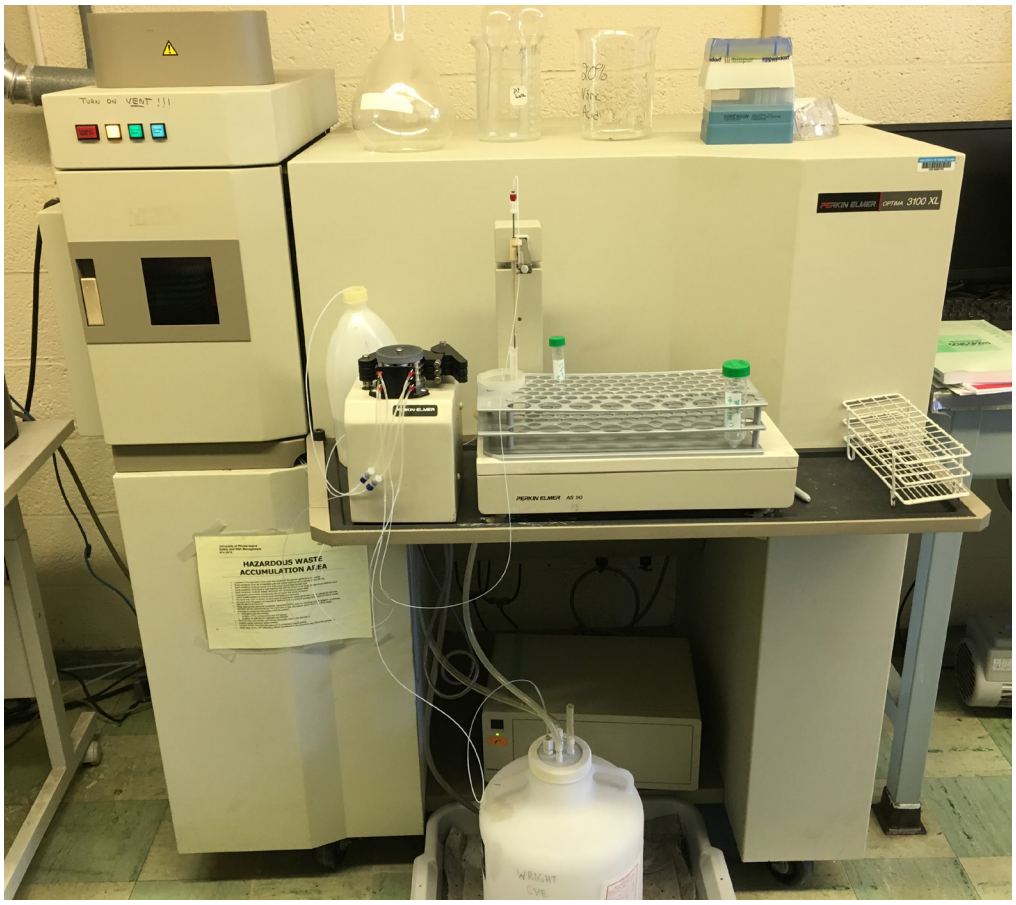

Figure A.5 The ICP-AES at URI main campus. The front tray hosed with thin plastic tubes is the auto sampler. The left half of the instrument makes of the ICP componant, while the right half contains the AES componant.

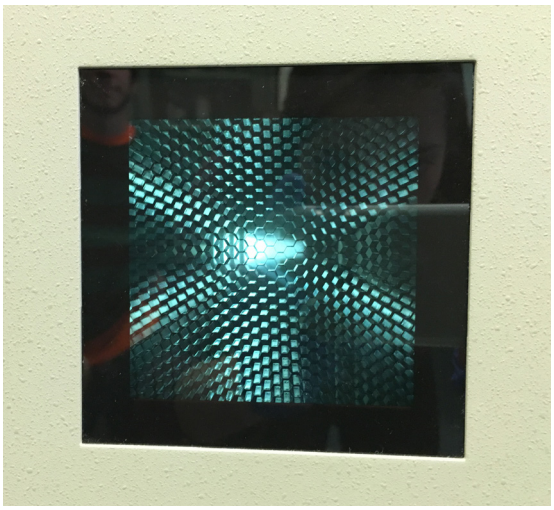

Figure A.6 Light emitted from atoms as they drop back down to ground state during ICP-AES analysis. Image of the view chamber displayed on the left side of the instrument in Figure A.5.

Appendix B: Additional SEM-EDS results

B.1 Additional SEM micrographs

SEM micrographs that were collected at Bates College Carnegie Science Center, but not included or discussed in the primary text.

B.1.1 SEM micrographs

Each image includes its corresponding sample ID (for simplicity, subsample "NA064-64A" has been notated as "64A" since the prefix "NA064" applies for all specimens). All SEM micrographs below were collected from gold-palladium coated specimens for sharper imaging.

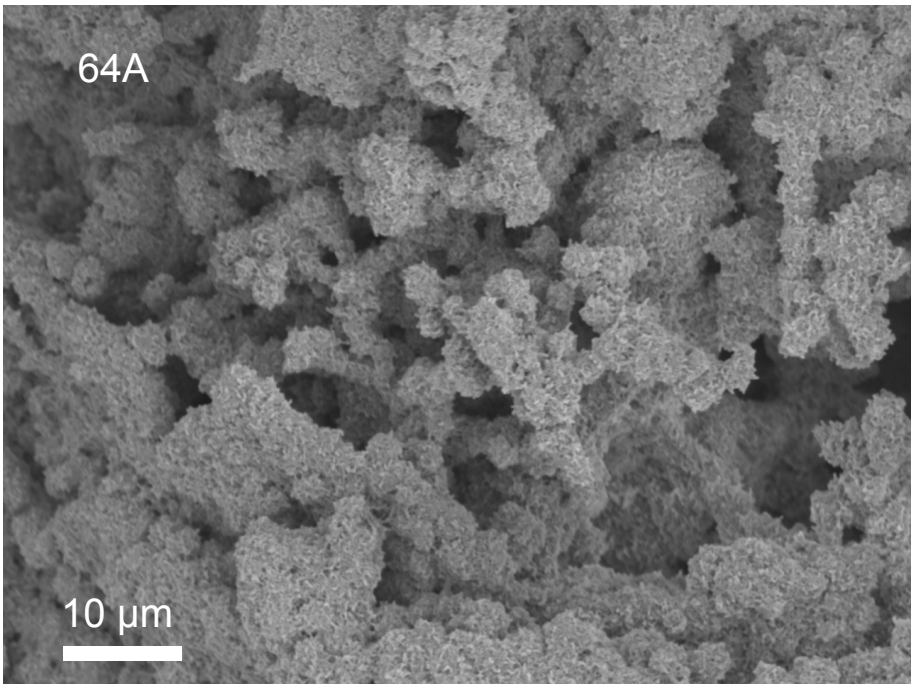

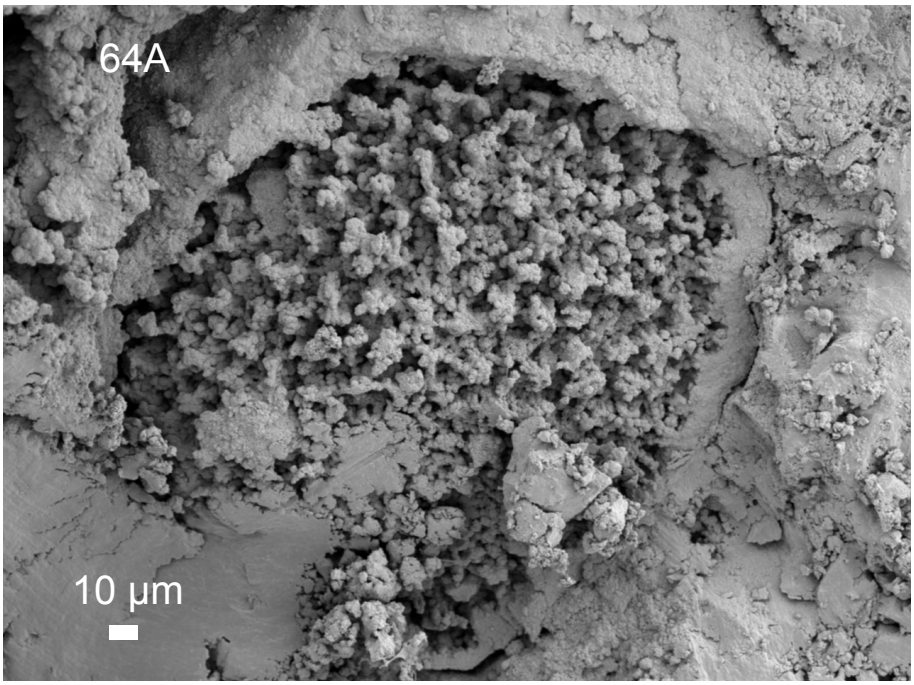
64A
10 µm

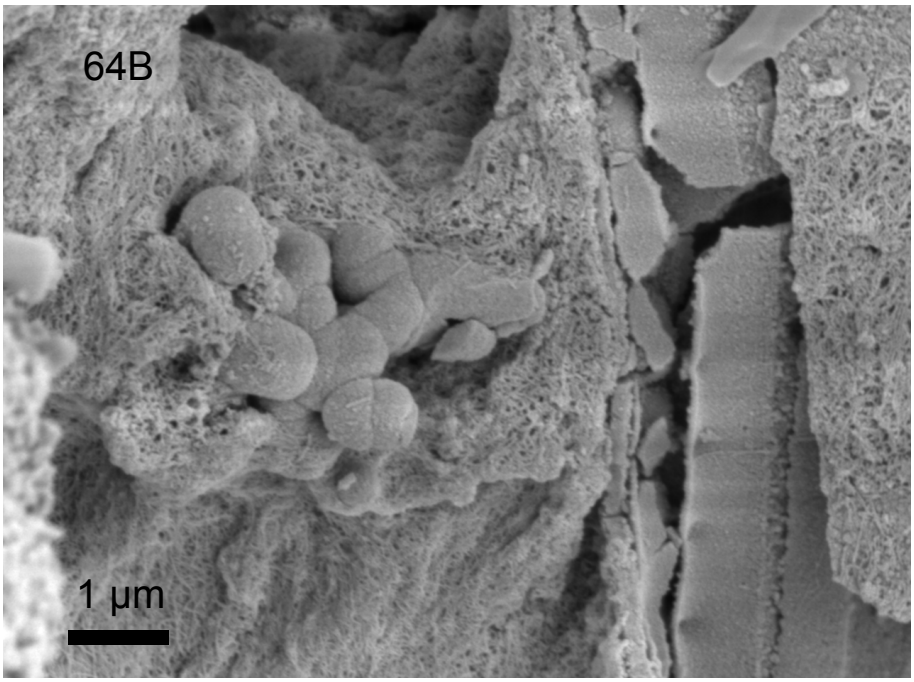
64B
1 µm

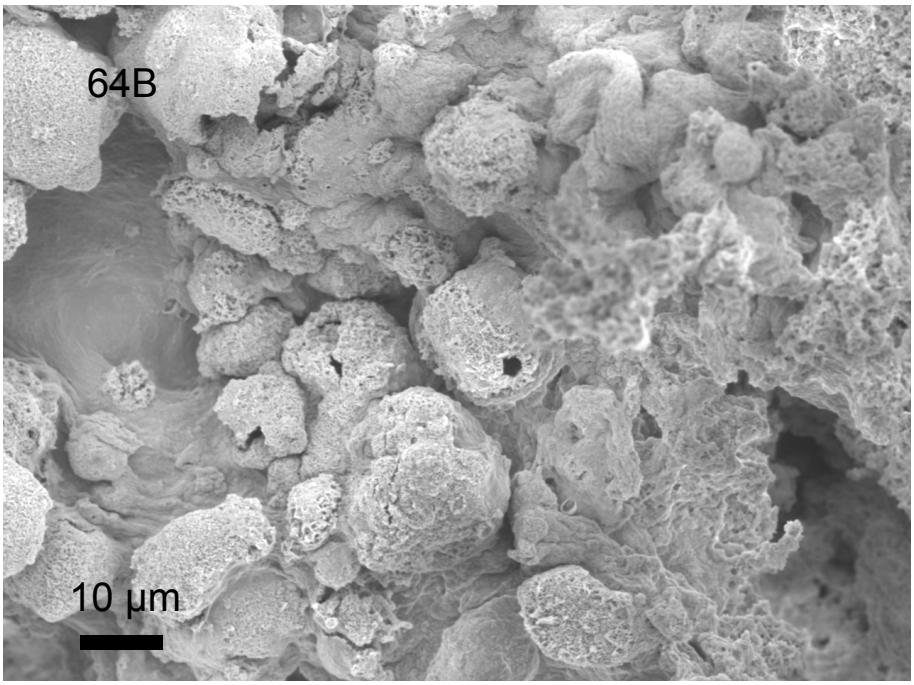
64B
10 µm

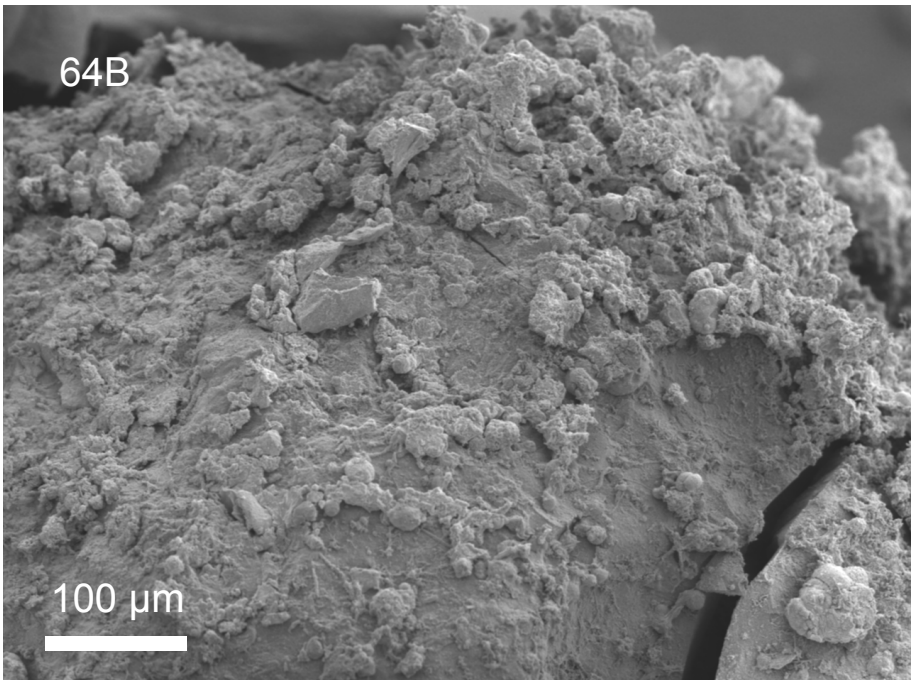
64B
100 µm

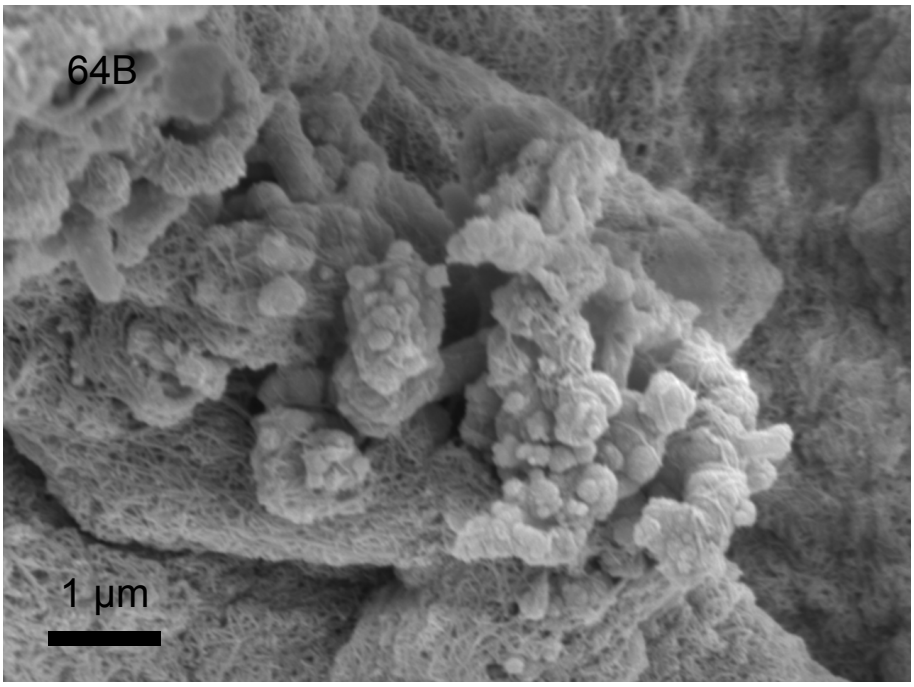
64B
1 µm

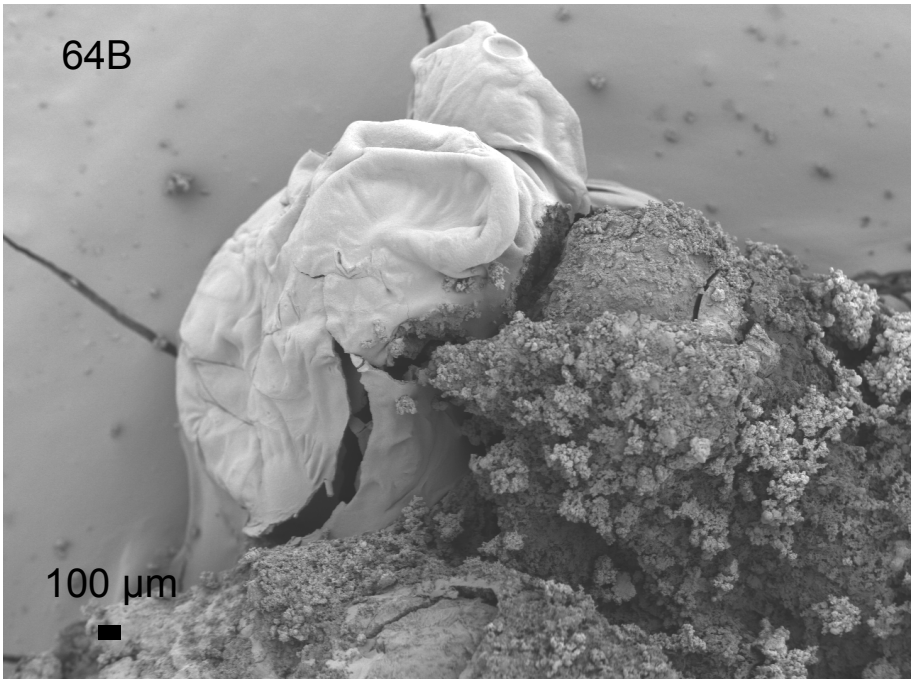
64B
100 µm

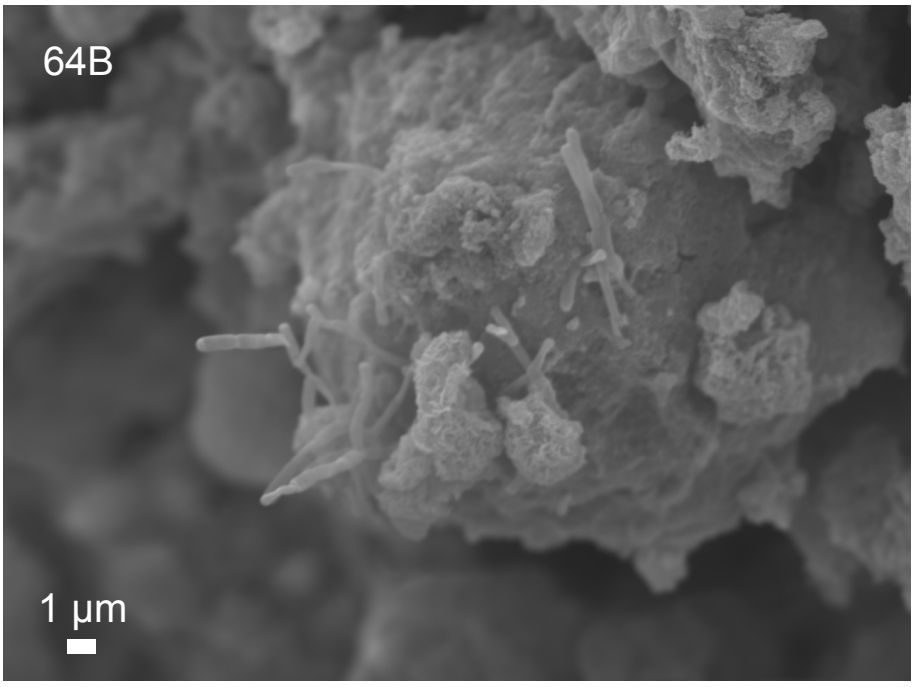
64B
1 µm

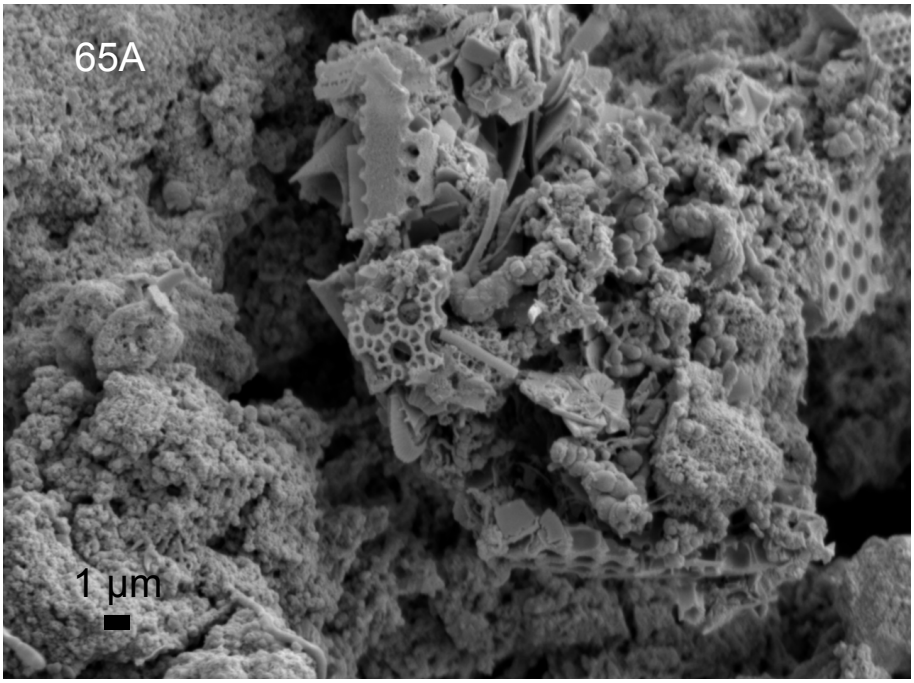
65A
1 µm

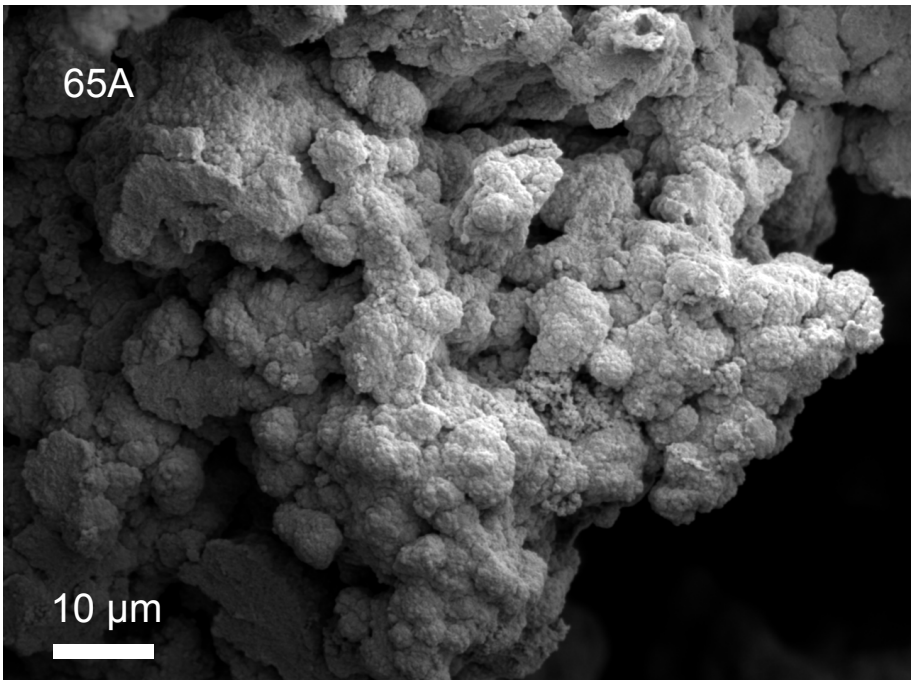
65A
10 µm

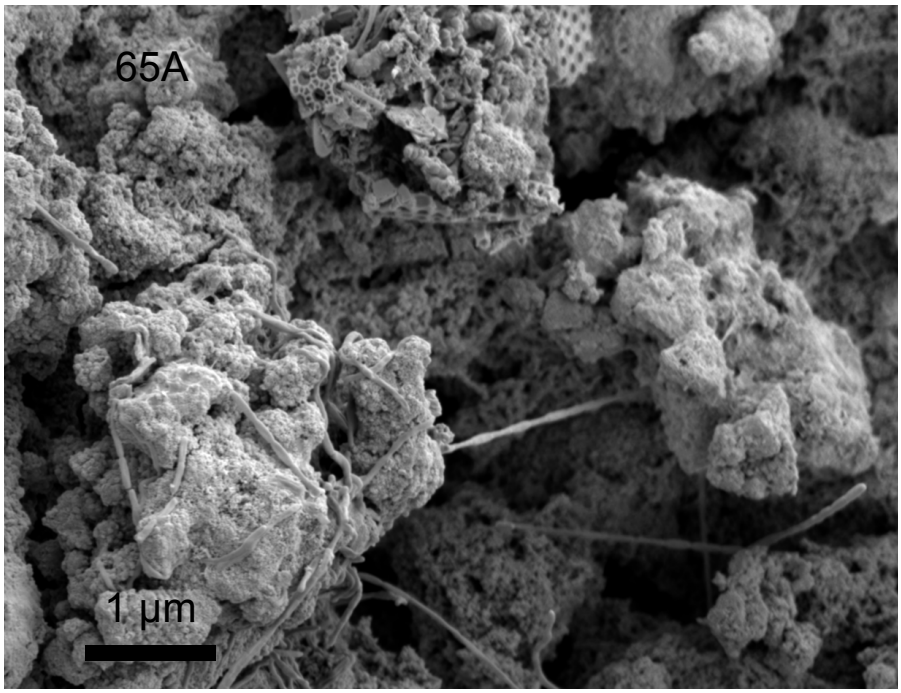
65A
1 µm

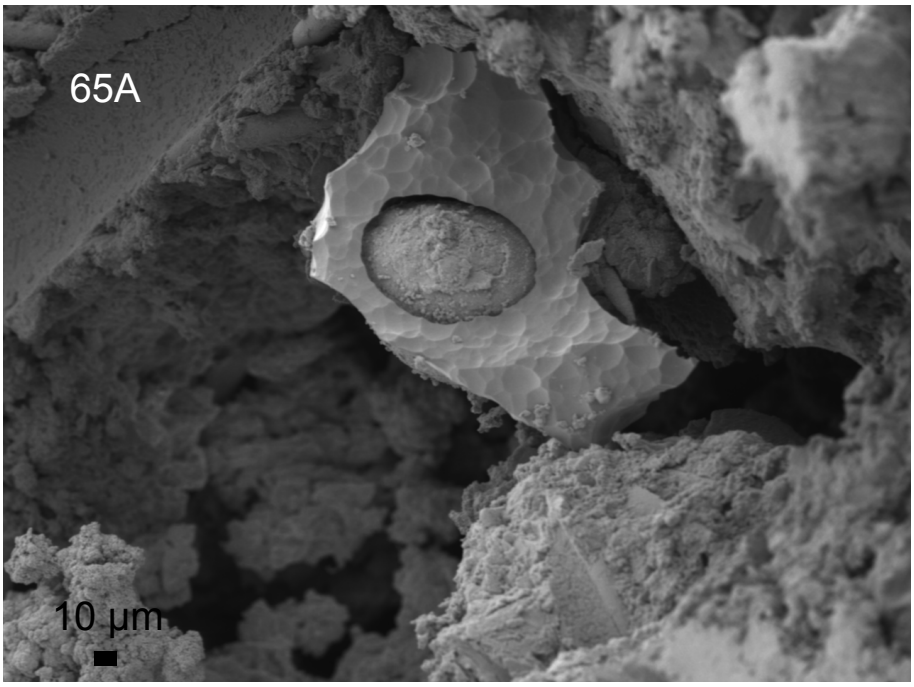
65A
10 µm

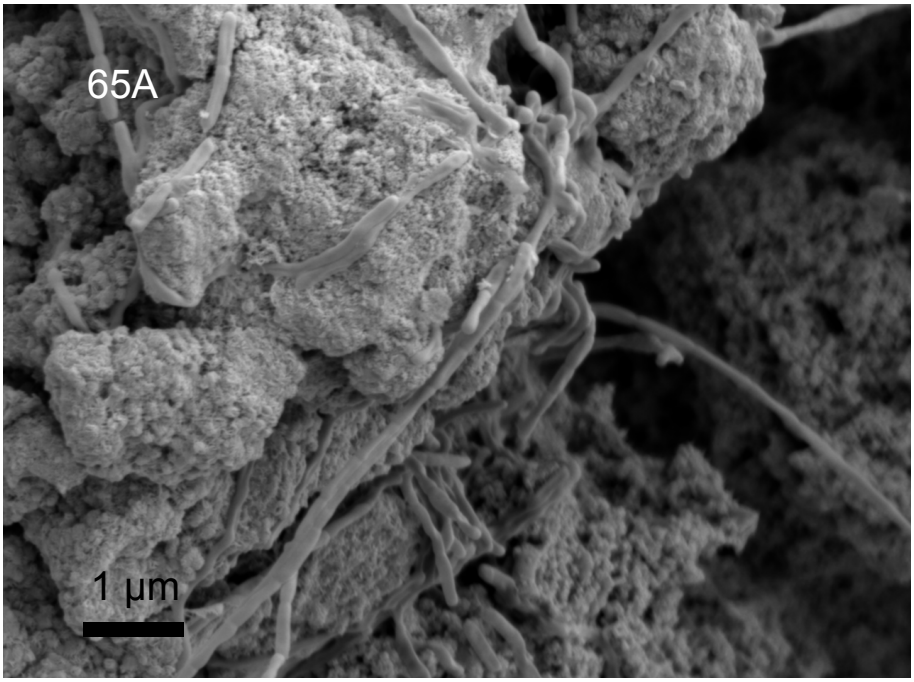
65A
1 µm

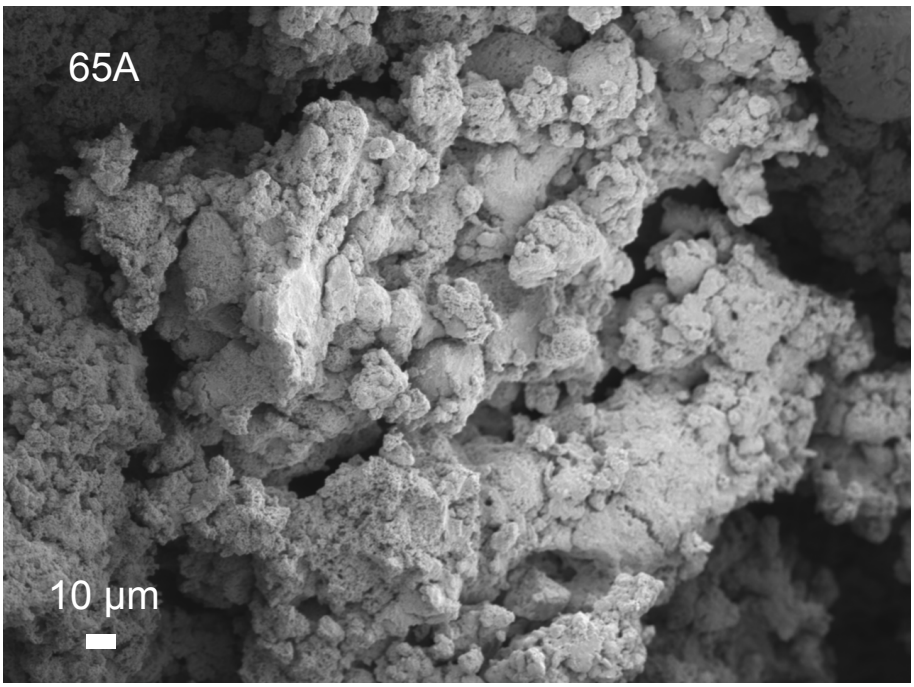
65A
10 µm

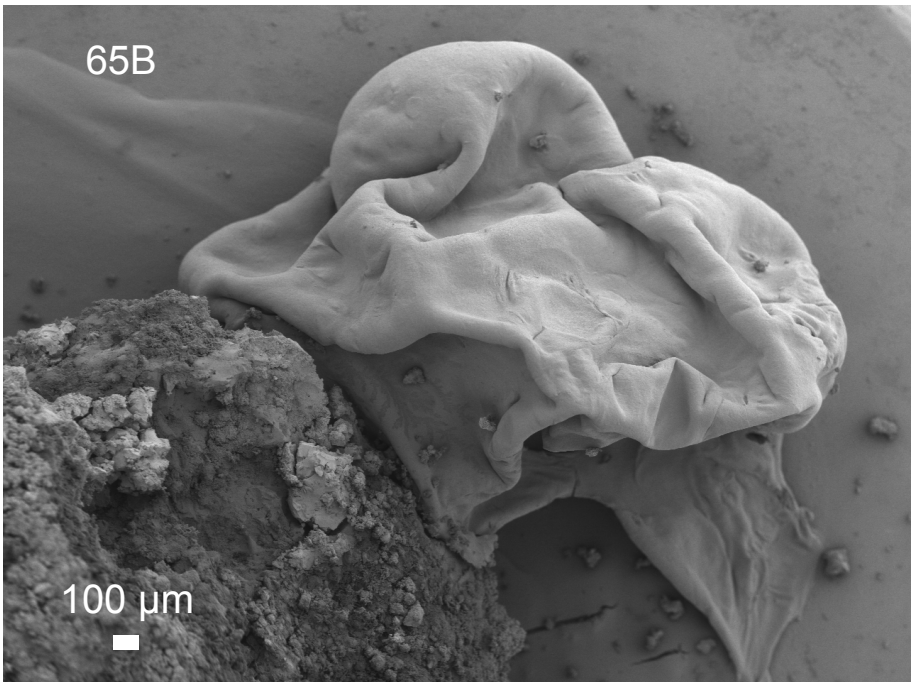
65B
100 µm

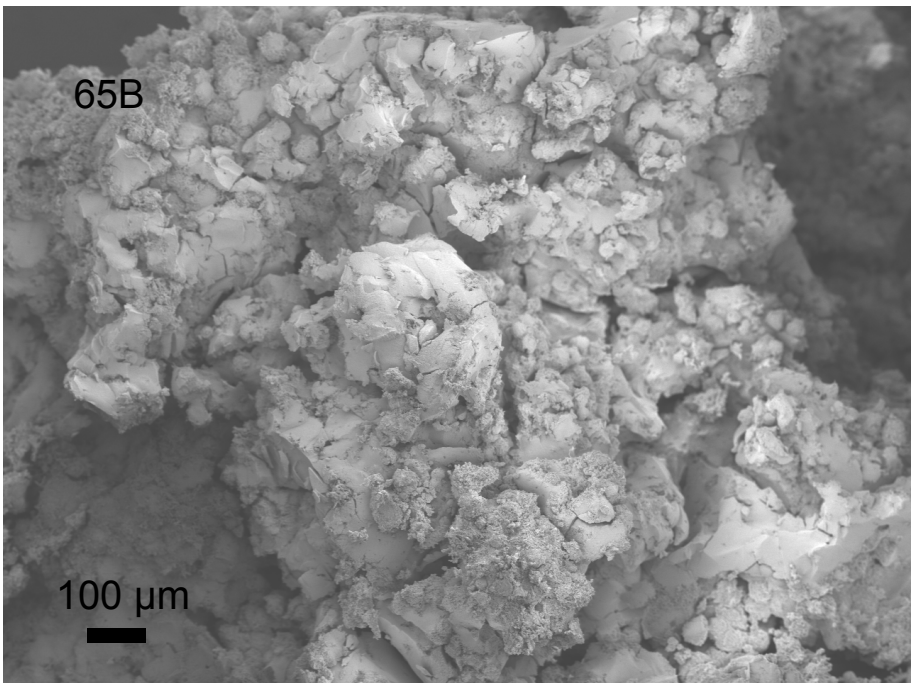
65B
100 µm

B.1.2 SEM micrographs of regions of EDS data

Each image includes its corresponding sample ID (for simplicity, subsample “NA064-64A” has been notated as “64A” since the prefix “NA064” applies for all specimens). The additional parenthetical numbers and labels on this collection of SEM micrographs are to differentiate between various specimens of the same sample. All images presented in this section correspond to regions where EDS data was collected (presented in section A.2). The central feature in each image was targeted for EDS data collection.

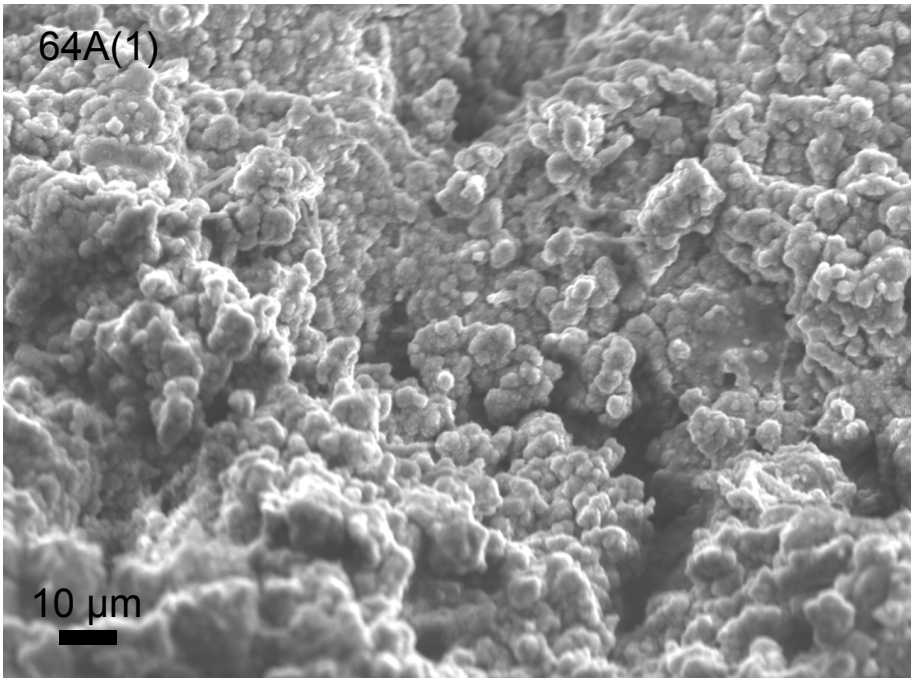

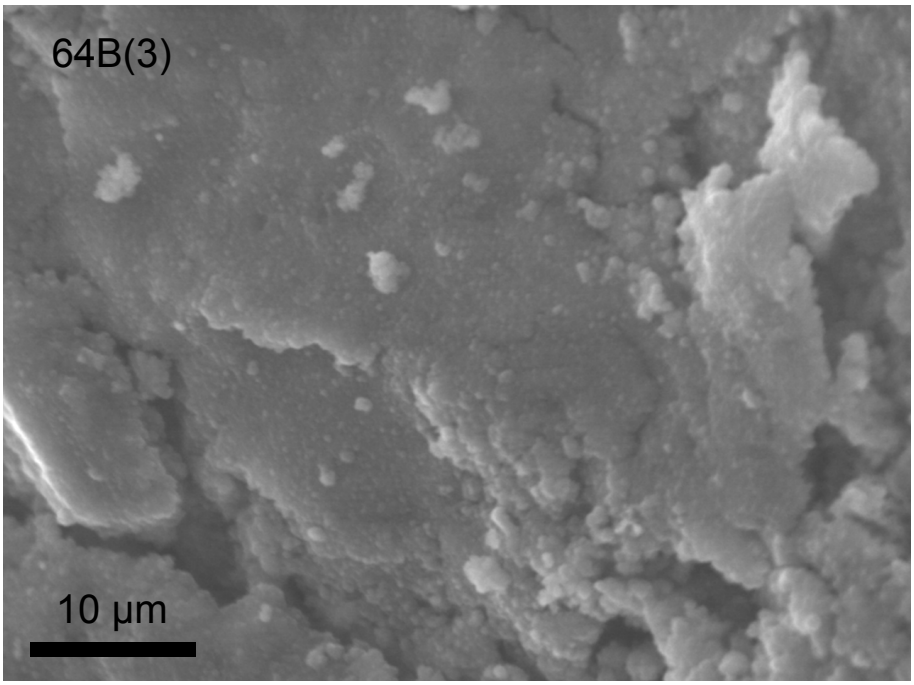
64B(3)
10 µm

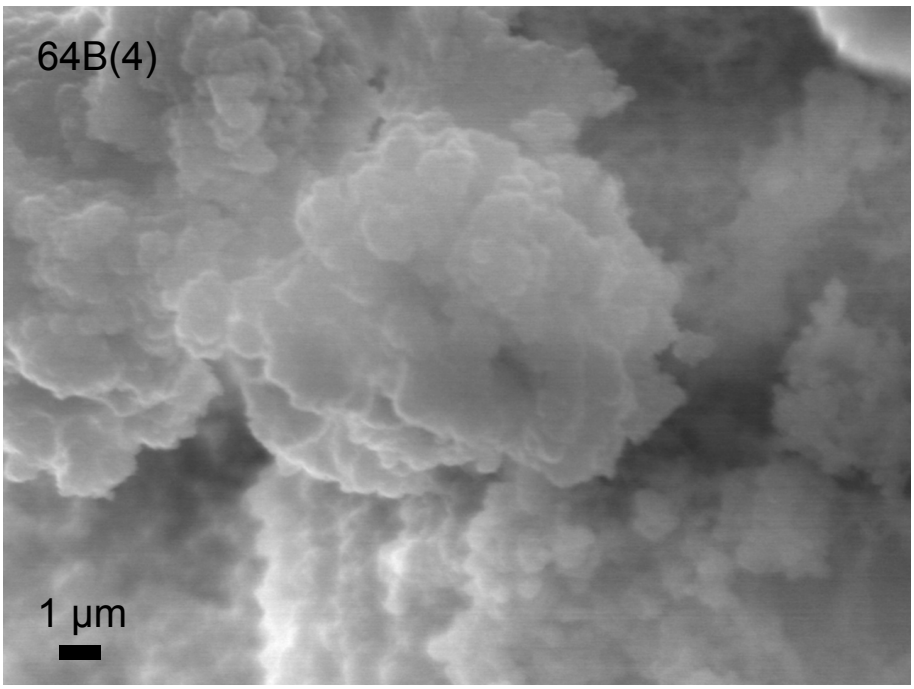
64B(4)
1 µm

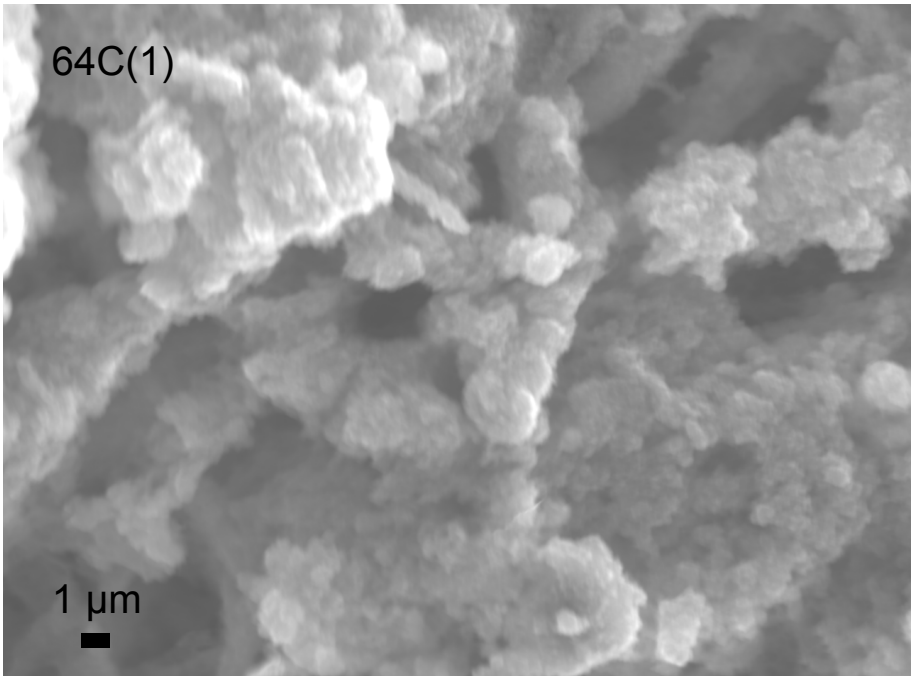
64C(1)
1 µm

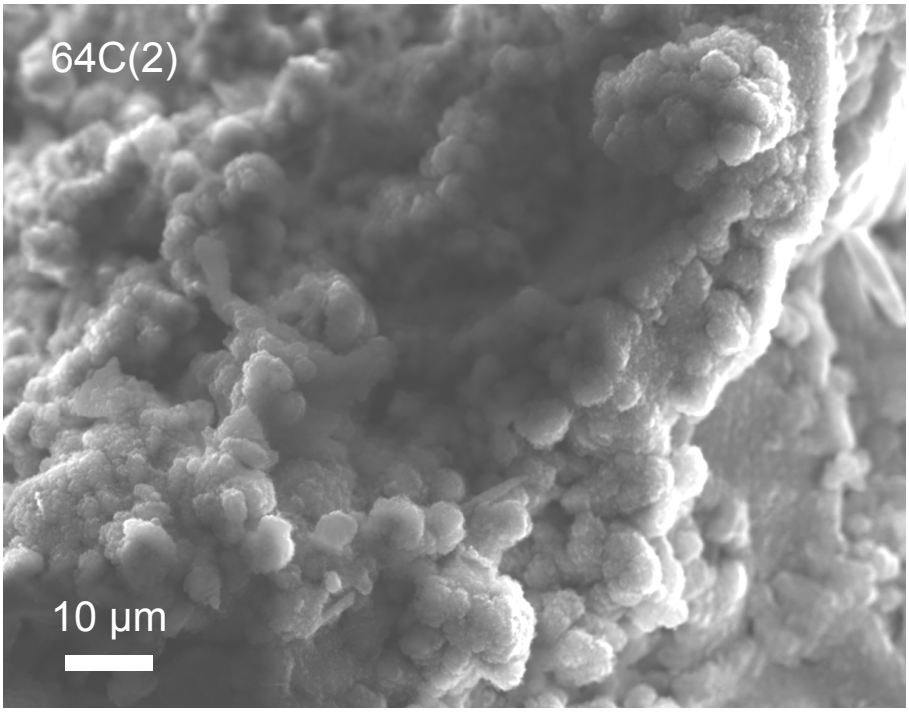
64C(2)
10 µm

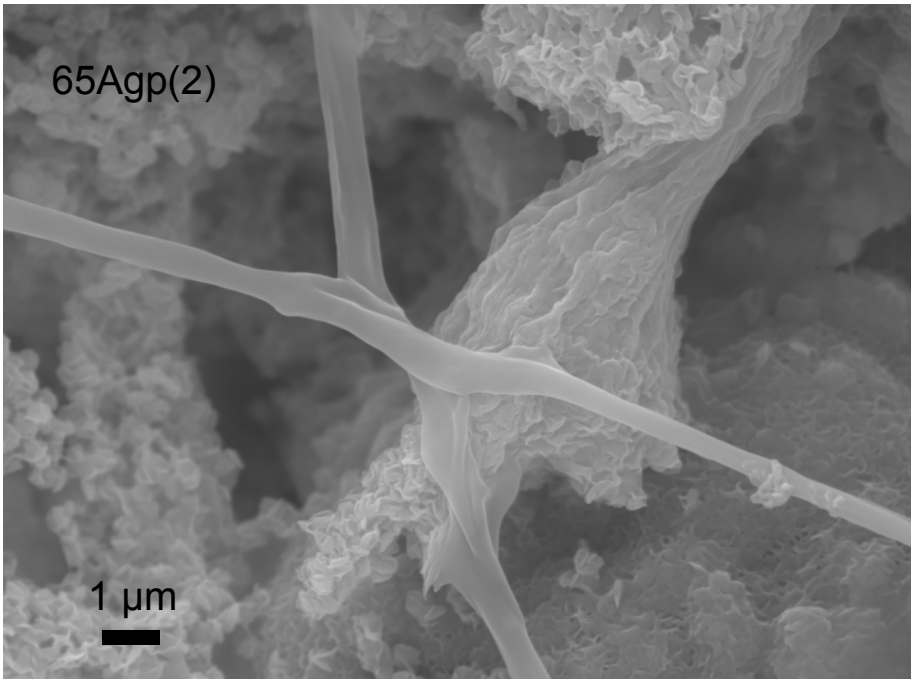
65Agp(2)
1 µm

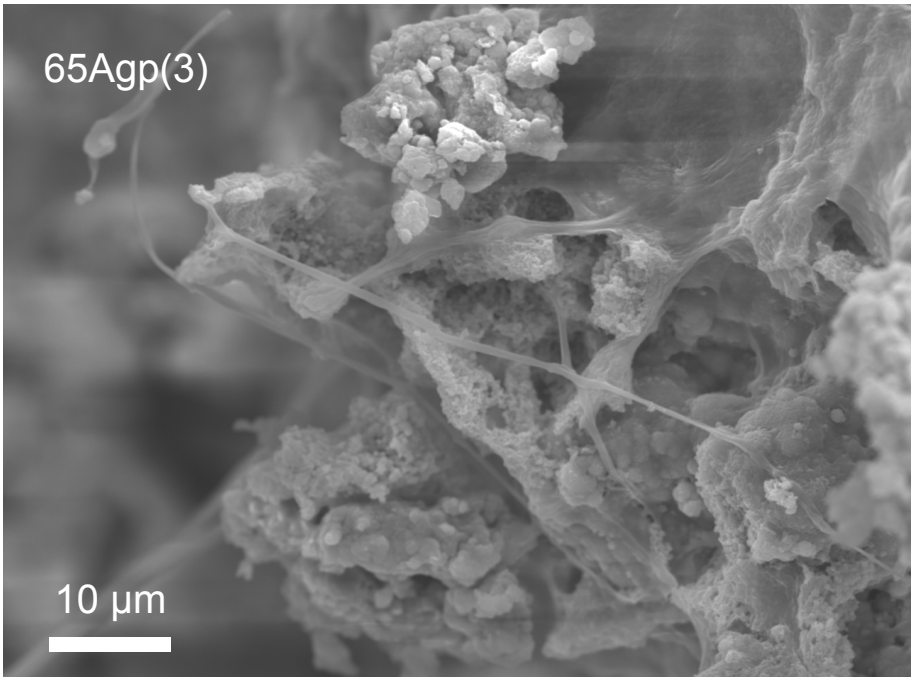
65Agp(3)
10 µm

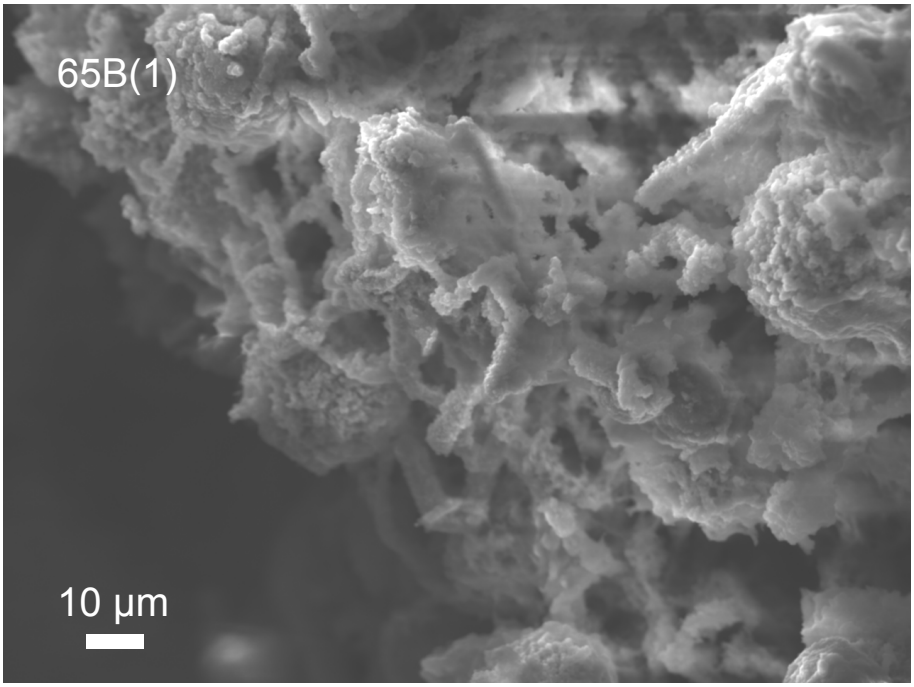
65B(1)
10 µm

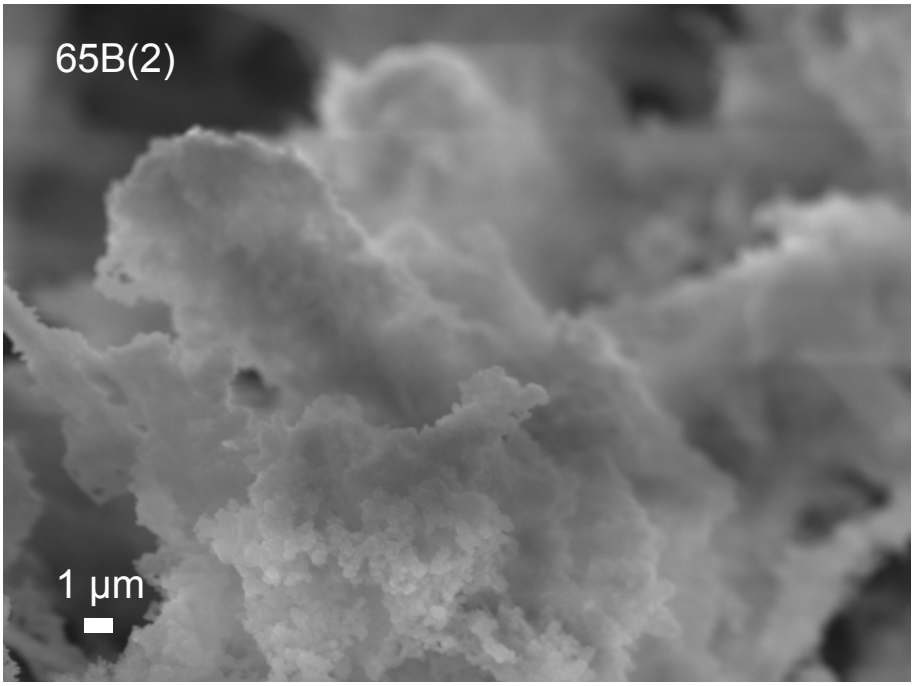
65B(2)
1 µm

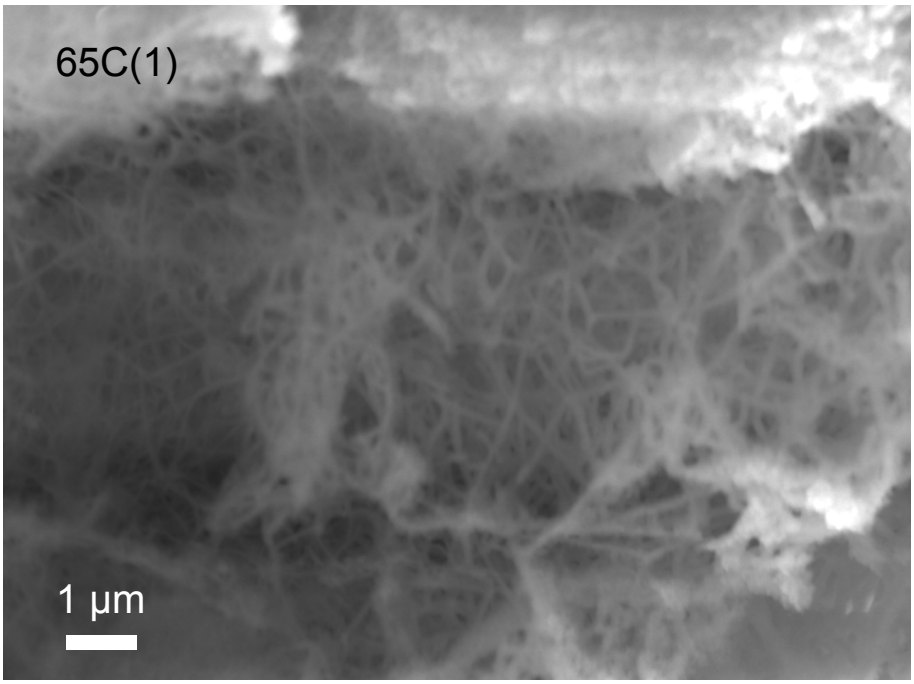
65C(1)
1 µm

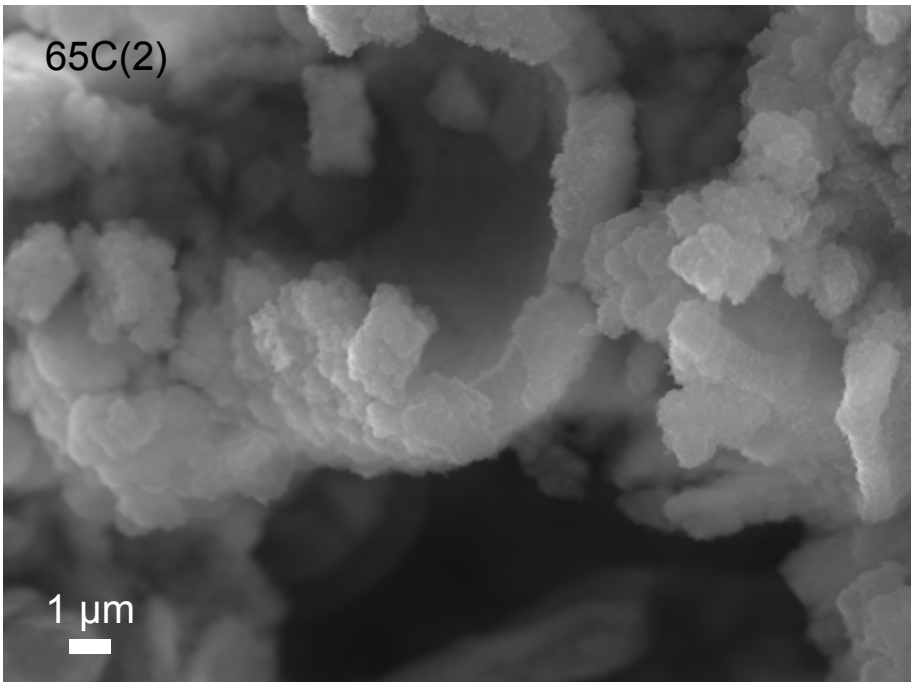
65C(2)
1 µm

B.2 Tabulated EDS results

EDS data for several specimens of samples from Seamount 3. Where appropriate, elemental data was converted to weight % oxide and then normalized to 100.

Sample/Specimen ID scheme: the first number and letter refers to the sample or sub-sample that the data was collected from. For example, specimen "64A(1)" comes from sample NA064-64 and from the sub-sample NA064-64A. The parenthetical numbers (such as the (1) in the above example) are just to differentiate between different specimens from the same sample. The inclusion of "gp" is to indicate that those particular specimen stubs were coated in gold-palladium for imaging rather than carbon like all of the other specimens. Any carbon detected for carbon-coated samples was removed from the data just as any gold or palladium detected from the "gp" samples was also removed from the data. The specimen ID's that end with an "*" indicate that the results from that particular data collection are discussed in the primary text and that SEM micrographs of that particular region are displayed in the primary text as well. For all other specimens, SEM micrographs of the scanned regions are presented earlier in this appendix (B.1). The second and third columns of data are from different regions of the same specimen, hence the same ID and similar results. Specimen "64C(3)" is the only set of EDS results without an accompanying SEM micrograph.

Sample/Specimen ID		64A(1)	64B(1)*	64B(1)*	64B(3)	64B(4)	64Bgp(1)*	64Bgp(2)*	64Bgp(3)*	64C(1)	64C(2)	64C(3)	65A(1)*	65Agp(1)*	65Agp(2)	65Agp(3)	65B(1)	65B(2)	65C(1)	65C(2)
Element or Oxide	Line	*(wt. %)*																		
SiO_2	K	48.42	14.37	13.75	18.67	16.90	0.51	9.41	11.07	13.60	21.08	14.29	41.50	24.14	18.19	13.77	2.01	16.13	14.66	3.27
Al_2O_3	K	0.34	-	-	-	0.50	0.63	0.10	0.29	0.20	0.24	0.56	0.26	0.16	0.17	0.19	0.25	-	0.48	0.91
Fe_2O_3	K	39.83	71.64	70.89	63.13	67.40	94.46	73.79	69.19	68.73	67.74	78.57	47.57	66.73	45.15	44.97	47.50	69.98	77.60	22.90
MnO	K	-	0.82	0.55	-	-	2.88	-	-	0.58	-	-	-	-	-	-	-	-	-	3.35
MgO	K	2.31	1.17	1.09	1.16	1.31	0.05	0.51	0.66	0.80	1.00	0.40	2.26	0.91	0.74	0.50	1.43	0.50	0.50	0.36
CaO	K	-	1.03	1.14	1.41	1.18	0.47	1.46	1.23	1.29	0.91	1.32	-	0.26	0.37	0.34	-	0.96	1.30	66.55
Na_2O	K	6.42	4.76	5.15	4.33	6.00	0.17	3.02	4.86	6.32	3.55	2.26	6.04	3.07	4.48	3.84	17.98	4.92	2.58	1.60
K_2O	K	2.05	0.51	0.56	0.87	0.61	-	-	-	0.24	0.78	-	2.37	1.66	1.63	1.42	-	0.22	0.21	-
P_2O_5	K	0.28	4.01	4.74	7.58	5.79	-	8.26	5.50	6.29	3.86	1.75	-	-	-	-	0.51	4.16	1.80	-
CuO	K	-	-	-	-	-	-	-	-	-	-	-	-	-	-	-	-	-	-	0.27
C	K	-	-	-	-	-	0.74	1.90	5.85	-	-	-	-	2.81	22.66	29.11	28.14	-	-	-
N	K	-	-	-	-	-	-	-	-	-	-	-	-	-	5.79	5.45	1.40	2.15	-	-
S	K	-	0.10	0.14	0.24	0.10	-	-	-	0.23	-	-	-	-	-	-	0.65	-	-	0.38
Cl	K	0.35	1.45	1.85	2.35	0.20	0.10	1.55	1.23	1.72	0.84	0.84	-	0.14	0.46	-	-	0.85	0.83	0.41
Br	L	-	0.09	0.14	0.22	-	-	-	-	-	-	-	-	-	-	-	0.11	0.14	-	-
Pd	L	-	0.02	-	0.05	-	-	-	0.12	-	-	-	-	-	-	-	0.01	-	0.01	-
Cd	L	-	0.03	-	-	-	-	-	-	-	-	-	-	0.11	0.36	0.40	-	-	0.02	-

Appendix C: Image analysis tracings

C.1 Tracings of deposits

Six ROV images of hydrothermal sinuous tubular deposits from Seamount 3. The tubular features are highlighted with red tracings. Spatial dimensions for all enclosed polygons were measured and plotted (see primary text for results).

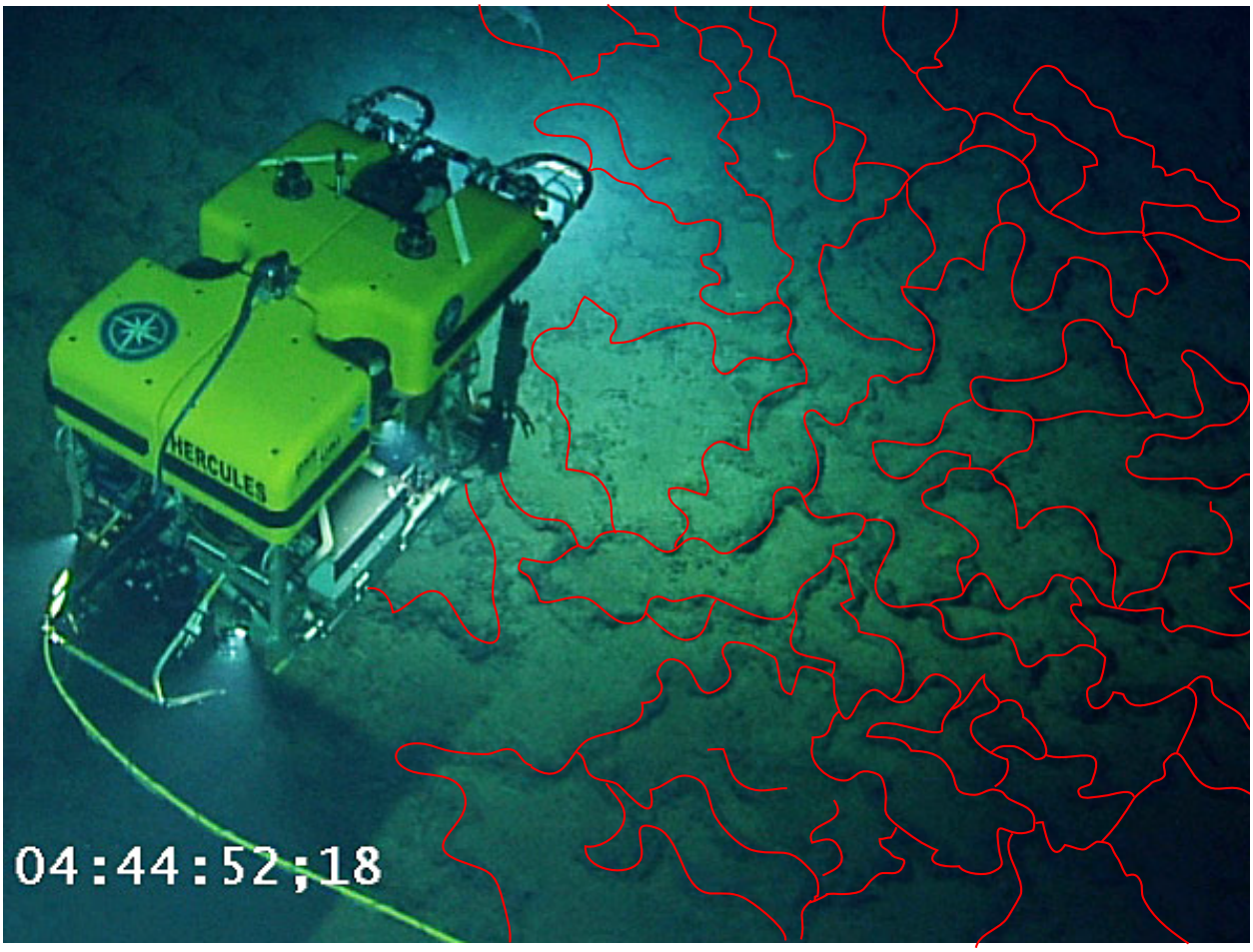

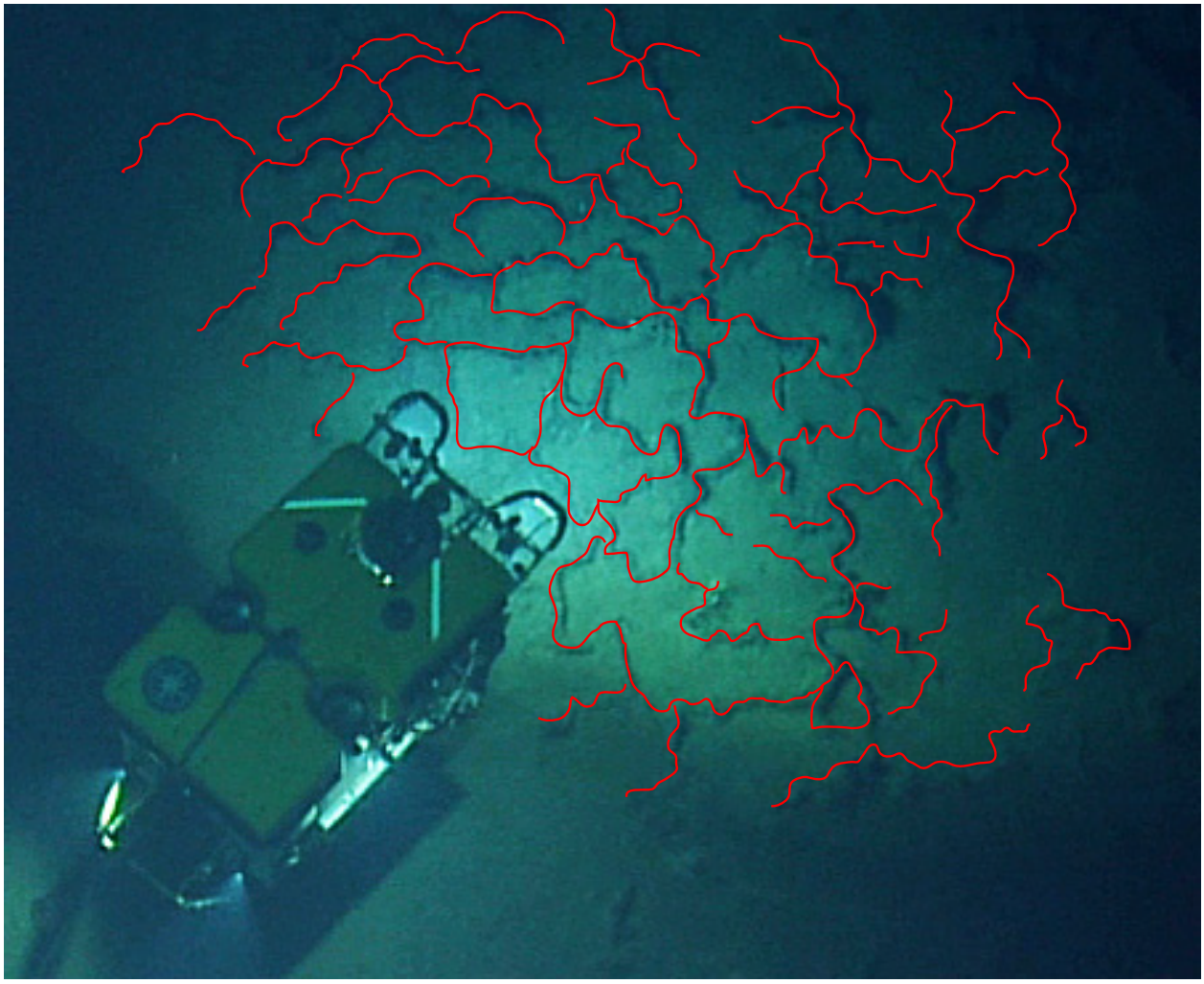

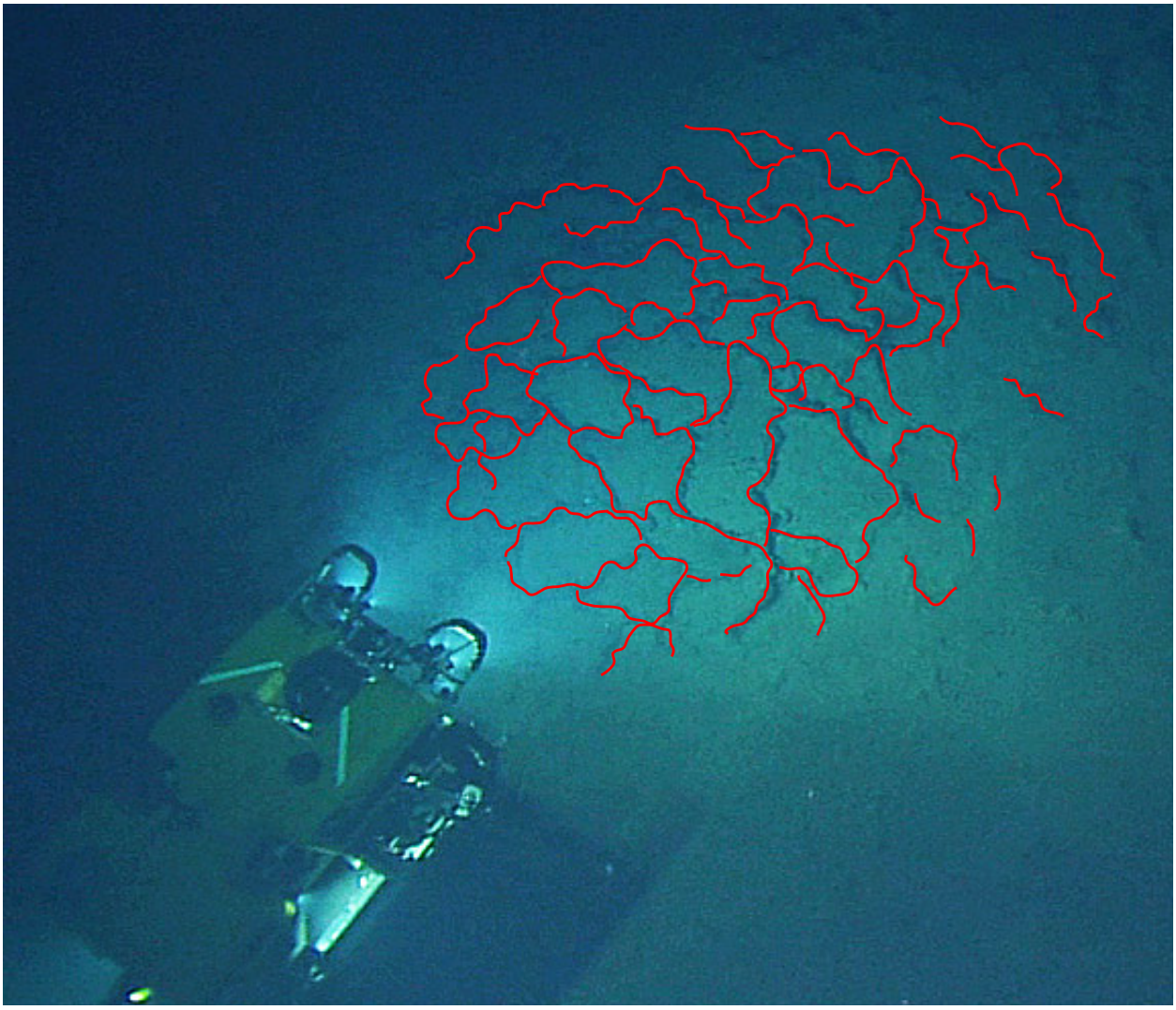

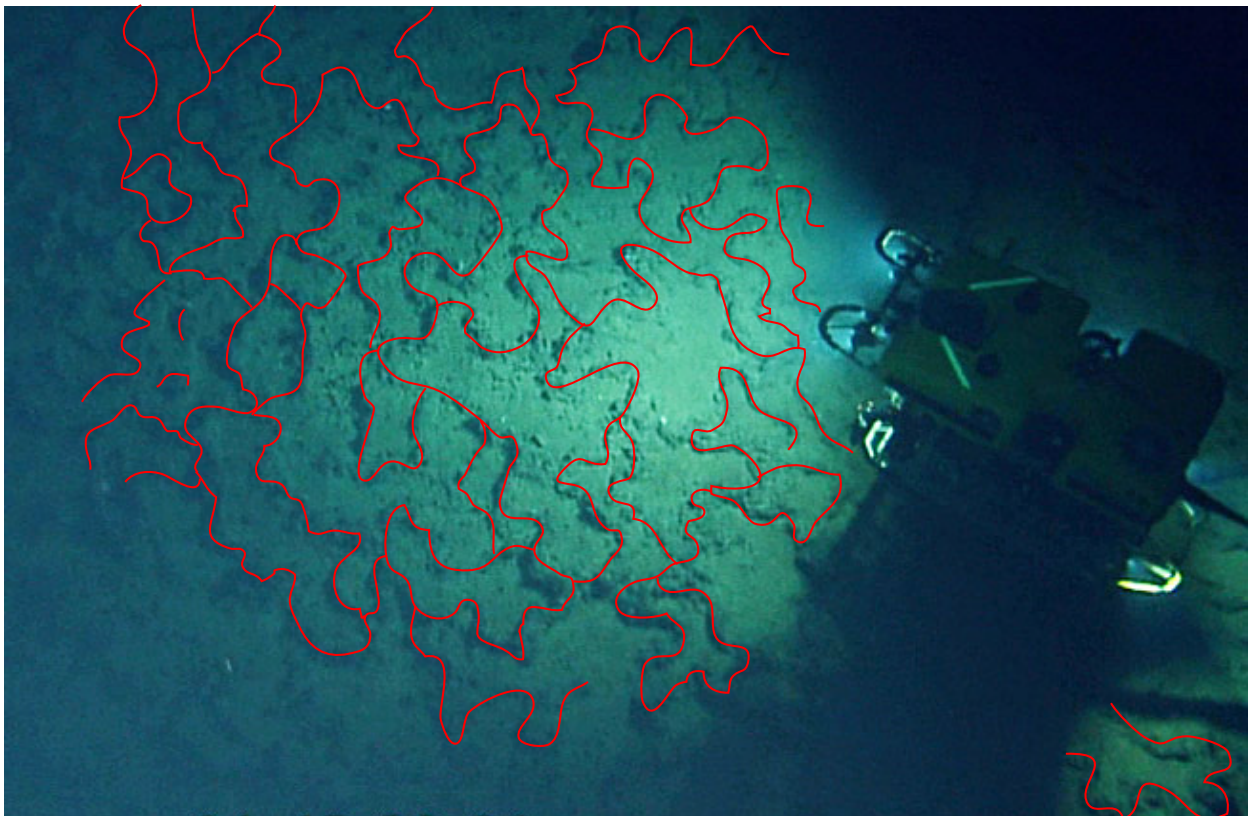

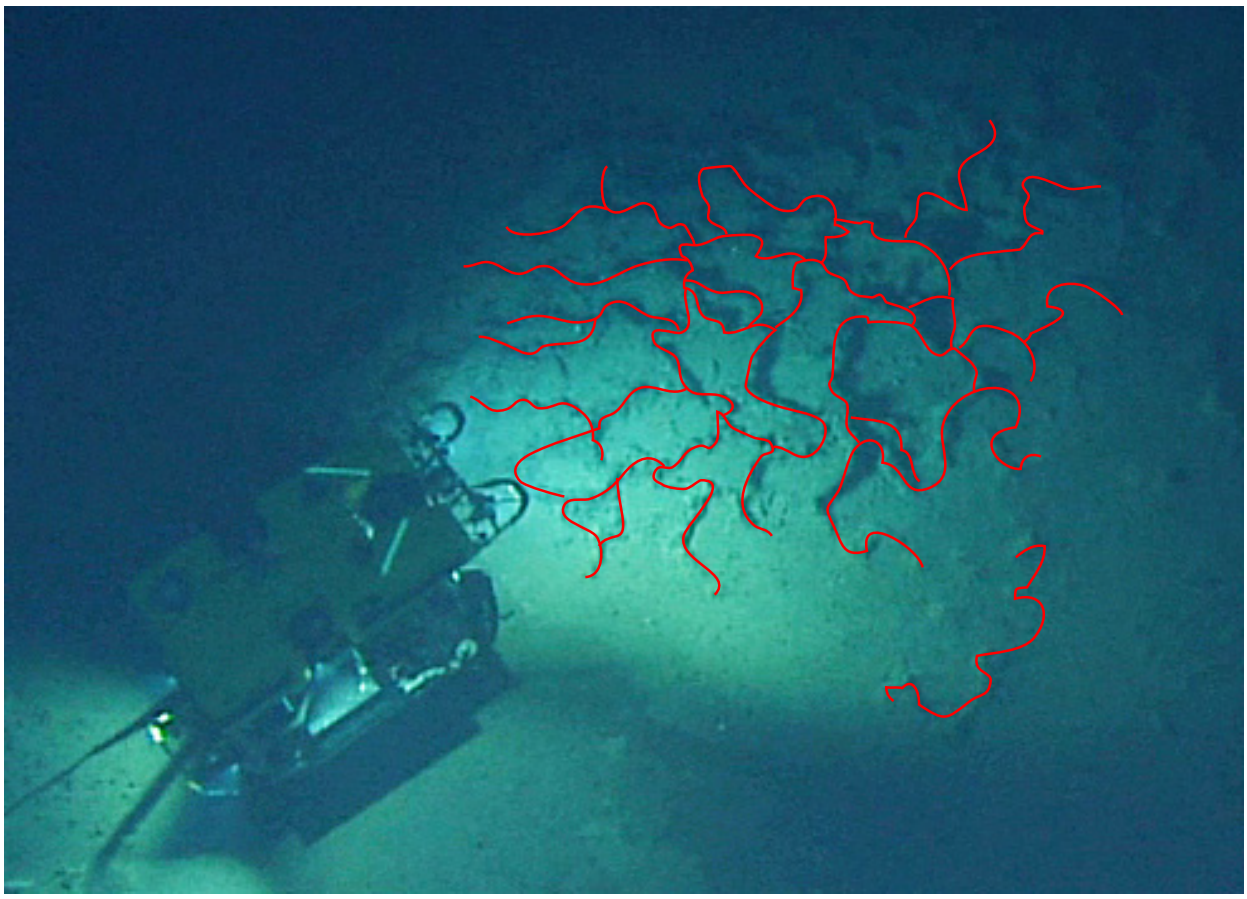

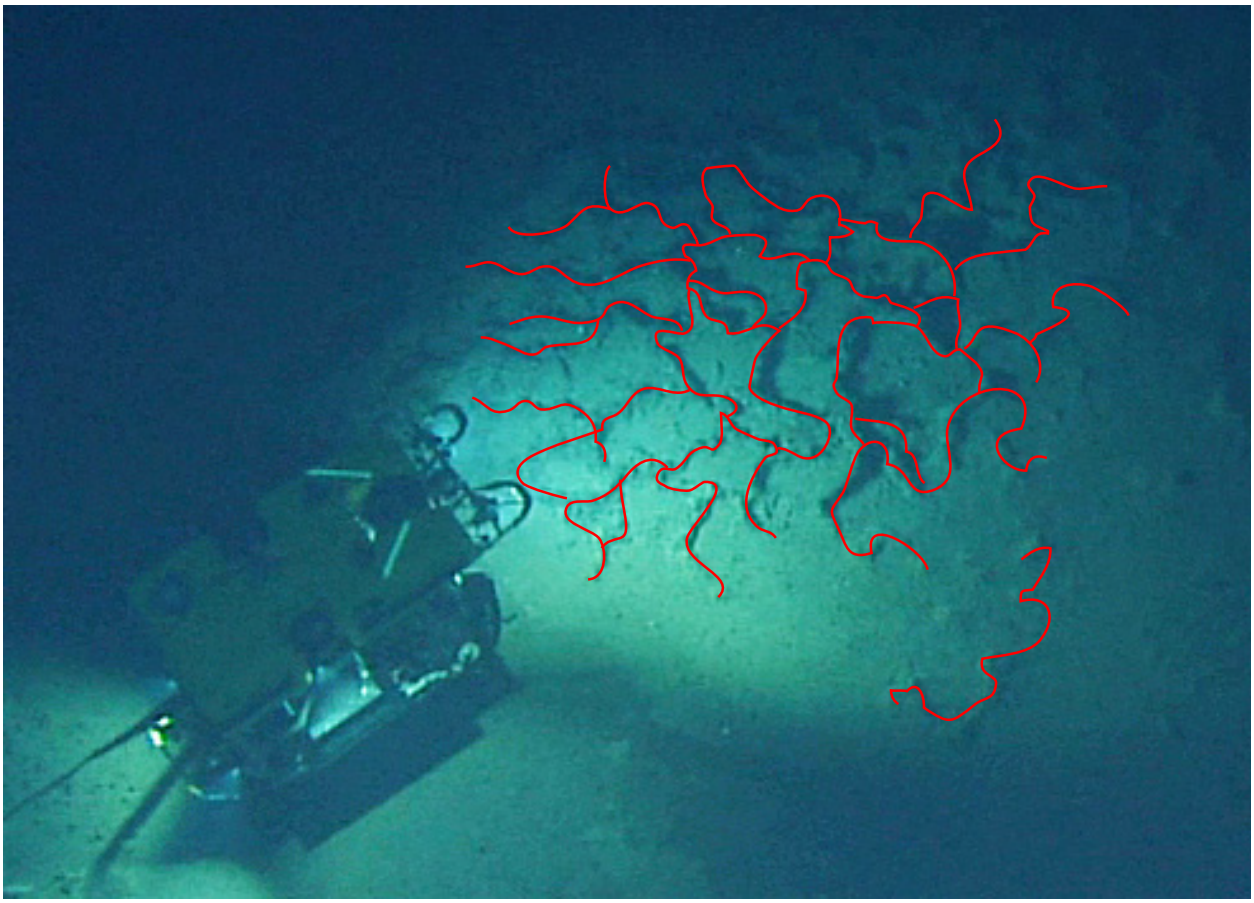

C.2 Tracings of pillow lava

Three ROV images of pillow lava from the region around Seamount 3. Clusters of pillow lobes are highlighted with red tracings. Spatial dimensions for each enclosed polygon were measured and plotted (see primary text for results).